SAPIENZA
UNIVERSITÀ DI ROMA

Coarse-grained models for polymer solutions and colloid-polymer mixtures

Scuola di dottorato in Fisica "Vito Volterra"

Dottorato di Ricerca in Fisica – XXVIII Ciclo

Candidate

Roberto Menichetti

ID number 1170331

Thesis Advisor

Prof. Andrea Pelissetto

A thesis submitted in partial fulfillment of the requirements
for the degree of Doctor of Philosophy in Physics

December 2015

Thesis defended on 22-01-2016
in front of a Board of Examiners composed by:

Prof. Angelo Vulpiani (chairman)

Prof. Massimo Gurioli

Prof. Massimo Capone

Coarse-grained models for polymer solutions and colloid-polymer mixtures

Ph.D. thesis. Sapienza – University of Rome

ISBN: 000000000-0

This thesis has been typeset by LaTeX and the Sapthesis class.

Version: August 29, 2017

Author's email: roberto.menichetti@roma1.infn.it

To my family, all my friends, my cats.

Abstract

Coarse-grained models are a very powerful —and sometimes necessary— tool in the analysis of the thermodynamic properties of macromolecular fluids. In these models, most of the original, microscopic degrees of freedom are integrated out and each macromolecule is mapped onto a set of effective sites, mutually interacting by means of appropriate intermolecular and intramolecular potentials. Depending on the number of sites n chosen, each macromolecule can be represented as a soft monoatomic molecule ($n = 1$), or as a soft n-atomic molecule ($n > 1$). The complexity of determining the complete set of effective interactions among the coarse-grained sites is such that an exact mapping is unfeasible in practice, hence approximations must be introduced, which always generate a lack of consistency between the original and the coarse-grained model.
In this thesis, we apply coarse-graining strategies to the investigation of the universal, large scale and thermodynamic properties of polymer solutions and colloid-polymer mixtures, for two different polymer architectures: linear chains and star polymers. We begin the discussion by briefly summarizing the main concepts of statistical mechanics and polymer physics, in a general fashion. We then revise the formalism behind structure-based coarse-graining procedures, both single-site and multi-site, critically analyzing their limits of validity and the methods proposed in the literature to extend them. Thereafter, we determine the accuracy of coarse-grained, single-site mappings in reproducing the correct thermodynamic behavior of solutions of linear chains and colloid-linear chain mixtures, for different average polymer-to-colloid size ratios. In conclusion, we discuss coarse-grained models for star polymer solutions in good solvents. We introduce a new multi-site model for star polymers, whose validity should extend up to the semidilute regime, and compare its predictions for the thermodynamic properties of the system with those obtained by means of single-site models.

Acknowledgements

When a journey reaches its end, it is useful to take a minute to rest and thank all those who helped you along the way. Briefly.
My first thoughts, obviously, are dedicated to my family. I will never forget their constant support and teachings, among which the most important is that of behaving always honestly (a concept which is much more subtle than the simpler "follow the rules").
Then, I would like to thank an extraordinary person, Prof. Andrea Pelissetto, for a very large number of reasons, which I will not list here. Just to mention the funniest one, for the patience he showed all the times I arrived with a brand new broken bone, after a brand new motorbike accident.
I will not make a list of all my friends, it would take too long and it is probably impossible. I just want to thank them all for what I am today.
I want to thank Noemi, even if things, sometimes, do not go the way we planned.
Last, but not least, I want to remember an incredible human being, Marco Dioguardi. Too soon, my good old friend, too soon. And unfairly.

Contents

Introduction **1**

1 Statistical Mechanics **5**
1.1 Statistical ensembles . . . 6
1.1.1 Canonical ensemble . . . 6
1.1.2 Grand canonical ensemble . . . 8
1.2 Particle densities and distribution functions . . . 8
1.2.1 Pair correlation functions and thermodynamics . . . 9
1.3 Integral equation methods . . . 11
1.3.1 Ornstein-Zernike relation . . . 11
1.3.2 Closure relations . . . 12
1.3.2.1 Hypernetted-chain . . . 13
1.3.2.2 Percus-Yevick . . . 13
1.3.2.3 Rogers-Young . . . 13
1.3.2.4 Reference-HNC . . . 14

2 Polymer Physics **17**
2.1 General features . . . 17
2.2 Polymer solutions . . . 19
2.3 Polymers in good solvents . . . 22
2.3.1 Microscopic models . . . 22
2.3.2 Dilute solutions . . . 25
2.3.2.1 The virial expansion . . . 25
2.3.2.2 Structure factor and correlation length . . . 27
2.3.3 Semidilute solutions . . . 29

3 Coarse-grained models for polymers **33**
3.1 Single-blob models . . . 34
3.1.1 State-dependent interactions . . . 39
3.2 Multiblob models . . . 40
3.2.1 Intramolecular interactions . . . 43
3.2.2 Intermolecular interactions . . . 45

4 Colloid/linear-chain mixtures **49**
4.1 Historical review and state of the art . . . 51
4.2 CG models for polymer solutions . . . 53
4.2.1 Zero-density single-blob models . . . 53

4.2.2 State-dependent single-blob models . . . 56
4.3 Colloid/polymer mixtures . . . 60
4.3.1 Monte Carlo simulations . . . 62
4.3.1.1 Results for $q = 1$ . . . 62
4.3.1.2 Results for $q = 0.5$ and $q = 0.8$ . . . 67
4.3.2 Integral equation methods . . . 69
4.3.2.1 Technical details . . . 71
4.3.2.2 Termination lines . . . 71
4.3.2.3 Structural behavior in the homogeneous phase . . . 74
4.3.2.4 Bridge functions at zero polymer density . . . 77
4.3.2.5 Integral equations with Monte Carlo bridge functions 81
4.3.2.6 Effective colloid-colloid pair potential . . . 82

5 Star polymers 85
5.1 Daoud-Cotton model . . . 86
5.2 Single-blob models . . . 90
5.3 Multiblob model . . . 92
5.3.1 Intramolecular interactions . . . 93
5.3.2 Intermolecular interactions . . . 98
5.4 Results . . . 101
5.4.1 Zero density . . . 102
5.4.2 Finite density . . . 103

Conclusions 109

Acronyms 113

References 115

Introduction

It is a matter of fact that the fast technological innovations of the last decades are strongly related to the development and characterization of new materials, each one with its own peculiar physical and chemical properties. Among them, macromolecular fluids showed to be very promising and challenging systems, both experimentally and theoretically, due to their complex physical behavior, which include a variety of fluid-fluid and fluid-solid transitions, glassy behaviors, microphase separations and supramolecular self-assembly. In this thesis, we will apply the methods of statistical mechanics to the description of the thermodynamic behavior of polymer solutions and colloid-polymer mixtures.

As is well known, polymers are macromolecules composed by L elementary units called monomers, which in the polymerization process are able to form covalent bonds. The resulting structure is complex, with many mesoscopic architectures [23]. According to the International Union of Pure and Applied Chemistry, colloids are mesoscopic particle whose extension in at least one direction lies between 1 μm and 1 nm.

The chemical properties of these systems strongly depend on the microscopic details, *i.e.* on the nature of the interactions among the microscopic components. At this level, a full-atomistic description of the system is needed: the chemical composition of monomers, the interactions with the solvent molecules and the microscopic description of the colloids must be resolved. However, it turns out that several large-scale thermodynamic properties are, to a large extent, independent of the chemical details, in the large degree of polymerization limit $L \to \infty$, but depend only on some general features, shared by a large variety of molecules [24–28]. In other words, the experimental data for the same observable, computed for very long molecules which differ in chemical composition, all fall on top of the same universal curve when expressed in terms of the appropriate scaling variables. This observed universality paved the way for the modern theory of polymers [29–31], which succeeded in describing their large-scale universal properties by means the renormalization-group methods, originally developed for the description of the second-order phase transition of ferromagnets [38–41]. Moreover, from a purely practical point of view, if one wants to investigate the large-scale properties of these systems, universality allows one to pick up one particularly simplified, convenient microscopic model, which is able to capture the correct universal behavior of the underlying microscopic model. This is a theoretically-driven, first level of coarse graining, in which solvent molecules are integrated out. For instance, polymers can be modeled as self-avoiding walks on a lattice and colloids can be modeled as hard spheres.

Although simplified, this atomistic approach becomes rapidly unfeasible, even nu-

merically, as the density increases, due to the large number of degrees of freedom involved in the description. This requires the introduction of a second level of coarse graining, dictated by computational necessity, in which the number of degrees of freedom is drastically reduced. In this approach, one integrates out most of the microscopic degrees of freedom, and represents each polymer as a set of n effective sites, interacting by means of appropriate potentials, whose functional form is again significantly constrained by universality. These mesoscopic models must be representative of the original mesoscopic behavior of the full atomistic system. Depending on the number of effective sites n chosen, one speaks of different coarse-grained (CG) representations: for $n = 1$, in the so-called single-blob (SB) picture, every polymer is mapped onto a soft monoatomic particle, thus retaining only three translational degrees of freedom per molecule [46, 47]. Interactions among these effective units are parametrized in terms of intermolecular potentials, which have an intrinsic many-body nature [32]. The most common choice is that of truncating the interaction series, working in the pairwise-additive approximation, with pair potentials defined in the zero-density limit. With this mapping, the system can be investigated by means of the statistical mechanics methods for simple fluids [2–4], *e.g.*, with Monte Carlo simulations or integral equation methods [3, 4]. Although computationally very convenient, due to the drastic reduction of the degrees of freedom involved in the description, single-blob models in the pairwise-additive approximation have a limited predictive power. Several methods have been proposed in the literature to extend their limits of validity, such as the reintroduction of many-body interaction terms, which significantly complicate the structure of the interactions, or switching to state-dependent pair potentials [70–74]. The last choice, more seriously, may introduce some inconsistencies in the thermodynamic behavior of the system [51, 52]. Another possibility consists in switching to a lower level of coarse-graining introducing multiblob (MB) models [83, 84], so that each polymer is mapped onto a soft n-atomic molecule, with $n > 1$. The effective sites interact by means of intramolecular and intermolecular potentials, parametrized in order to reproduce the mesoscopic behavior of the original microscopic system. As we will discuss, this method allows one to solve most of the criticalities arising in single-blob models, increasing the range of validity of coarse-grained, zero-density models in reproducing the thermodynamic behavior of the original system.

In this thesis, we will focus on two polymer architectures: linear chains and star polymers.

Linear chains have been extensively studied in the literature, and a large amount of theoretical and numerical accurate predictions for their thermodynamics and structural properties have been obtained [29–31, 70–72, 78, 102]. Here, we critically analyze and discuss the accuracy of coarse-grained, single-blob models, both in the zero-density [69, 76] and state-dependent approximations [72], in reproducing the scaling-limit thermodynamic behavior of solutions of linear chains, and the phase diagram of colloid-linear chain mixtures. This will be done, when possible, by means of a direct comparison with full-monomer results, or with other approximate theories.

Star polymers are molecules composed by f polymer chains tethered to a common core [46]. By increasing the functionality f, they smoothly interpolate between linear chains ($f = 2$) and soft colloidal particles ($f \gg 1$) . Their configurational properties have been mostly analyzed in terms of simple phenomenological mod-

els [129, 130], and little is known about their thermodynamic behavior. Indeed, most of the numerical investigations have been based on qualitative coarse-grained, zero-density SB models [75]. Here, we analyze the system by means of accurate SB models [76] and propose a new multiblob model which should be able to reproduce the thermodynamic behavior of star polymer solutions up to the semidilute regime.
The thesis is organized as follows.
In Chap. 1, we briefly summarize the main concepts of statistical mechanics applied to monoatomic fluids. We present the statistical ensembles, focusing on their relations with the thermodynamic behavior of a system. We define the particle densities and distribution functions, and discuss the integral equation methods, which are a powerful (and computationally convenient) tool for determining the thermodynamics of systems with pairwise-additive interactions. They are based on the exact Ornstein-Zernike relation, supported by an approximate closure relation. We explicitly report and discuss the various closure relations we use in the analysis of the thermodynamic properties of polymer solutions and colloid-polymer mixtures.
In Chap. 2 we recall the main concepts concerning polymer physics. We briefly discuss the general features of polymers, focusing on the aforementioned properties of universality. We then present polymer solutions, and the various concentration regimes: dilute, at overlap and semidilute. We discuss the influence of temperature and monomer-solvent interactions on the average large-scale properties of these macromolecules. This leads to the classification of polymer solutions in terms of good solvents, poor solvents and θ-solvents. We then analyze the behavior of polymers in good solvents, which is the subject of this thesis, presenting various microscopic models which are able to reproduce the universal, large-scale properties of the system. The theoretical predictions for the thermodynamic behavior of polymers in good solvents are then discussed in two opposite concentration regimes: in the low-density limit, by means of the polymer virial expansion, and in the semidilute regime, by means of scaling theories and the blob representation of polymers in terms of correlation blobs, which can be considered the pathway to the definition of coarse-grained multiblob models.
In Chap. 3, we discuss the general formalism behind structure-based coarse-graining strategies, and apply it to the case of polymer solutions. We describe single-blob models, discussing how intermolecular interactions among the coarse-grained molecules are parametrized and obtained, focusing on their relation with the thermodynamic properties of the original system. We critically discuss the limits of validity of SB models, and the methods proposed in the literature to extend them.
Then, we present a multiblob coarse-graining strategy, and discuss its limits of validity. We discuss the problems related to the determination of the exact intramolecular and intermolecular interactions, and introduce some approximations which can make this task feasible in practice, keeping in mind that the primary requirement is always the thermodynamic consistency between the coarse-grained and the original model.
In Chap. 4, we discuss the thermodynamic properties of colloid-polymer mixtures, as predicted by several single-blob models, which differ in the choice of the effective interaction site or in the state-dependency of the interactions. We start the discussion by determining the accuracy of these SB models in describing pure polymer solutions, comparing their predictions for the thermodynamic and structural properties with those obtained by means of Monte Carlo simulations of the full-atomistic system.

Then, we introduce colloid-polymer mixtures, and determine the phase diagram of the system by means of Monte Carlo simulations of the CG SB models, for different polymer-to-colloid size ratios. We compare these predictions with those obtained by means of full-monomer simulations, when possible, and by means of other approximate theories, in order to assess the accuracy of single-blob models in reproducing the phase behavior of the original system. At last, we compare the phase diagrams of SB models obtained by means of Monte Carlo simulations with those obtained by means of integral equation methods, for all the closure relations introduced in Chap. 1. This allow us to determine the accuracy of the various approximate closure relation in reproducing the exact phase behavior of the system. The results of this chapter have been recently published in Refs. [96, 97].
In Chap. 5, we focus on the thermodynamic behavior of star polymer solutions. We begin the discussion by presenting a phenomenological model which describes the conformational properties of a single star polymer. Then, we introduce a set of single-blob models, which differ in the choice of the effective interaction site. Finally, we propose a multiblob model for star polymers, which should be able to reproduce the properties of the underlying microscopic system up to the semidilute regime. As far as we know, there are no full-monomer results in the literature to compare with, hence we take the multiblob results for the thermodynamics and structural properties as the reference ones, and compare them with the predictions obtained by means of the SB models. This allow us to test the accuracy of single-blob models in reproducing the behavior of the system.
The residual flexibility of the multiblob model allows us to make some predictions for the structural behavior of star polymers as the density increases. This represents a significative improvement towards a better characterization of the polymer-to-colloid crossover, which is expected to occur as f increases.

Chapter 1

Statistical Mechanics

As is well known, the state of a system in thermodynamics is specified by a set of few measurable *macroscopic coordinates*, such as the pressure P exerted on the walls of the container of volume V, and the temperature T. The laws of thermodynamics are mainly based on experimental evidence and describe the system as a whole, without taking into account the dynamics or chemical structure of the microscopic components. The derivation of the macroscopic properties from the laws governing the underlying microscopic world is the purpose of statistical mechanics. In this chapter, we will briefly recall its principles and formalism, with no claims of being exhaustive. For further details on the subject, please refer to Refs. [1–3]. All the discussion will be developed for atomic fluids, considering both one-component systems [4] and mixtures [3, 5]: the generalization to molecular fluids is straightforward, and will be explicitly provided when needed.

In classical mechanics the state of a system is specified by the set of coordinates $\mathbf{r}^N = \mathbf{r}_1, .., \mathbf{r}_N$ and momenta $\mathbf{p}^N = \mathbf{p}_1, .., \mathbf{p}_N$ of the particles, which belong to the $6N$-dimensional Γ-space. The dynamics is specified by the Hamilton's equations of motion

$$\dot{\mathbf{r}}_i = \frac{\partial \mathcal{H}}{\partial \mathbf{p}_i}, \quad \dot{\mathbf{p}}_i = -\frac{\partial \mathcal{H}}{\partial \mathbf{r}_i} \quad , \tag{1.1}$$

where

$$\mathcal{H}(\mathbf{r}^N, \mathbf{p}^N) = K_N(\mathbf{p}^N) + V_N(\mathbf{r}^N) + \Phi_N(\mathbf{r}^N) \tag{1.2}$$

is the Hamiltonan of the system, consisting of a kinetic term K_N, an interaction term among the molecules V_N and (eventually) a coupling of the molecules to an external field Φ_N, which breaks the spatial homogeneity.
The state of the system is completely specified by the solution of Eq. (1.1) for the $6N$ degrees of freedom, which is clearly completely unfeasible for very large systems. In statistical mechanics one defines a phase-space probability distribution function $f^{[N]}(\mathbf{r}^N, \mathbf{p}^N, t)$, where $f^{[N]} d\mathbf{r}^N d\mathbf{p}^N$ represents the probability for the system to be in a hypercube $d\mathbf{r}^N d\mathbf{p}^N$ centered in $(\mathbf{r}^N, \mathbf{p}^N)$ at time t. Since it is a probability density, $f^{[N]}$ satisfies the normalization condition

$$\iint f^{[N]}(\mathbf{r}^N, \mathbf{p}^N, t) d\mathbf{r}^N d\mathbf{p}^N = 1. \tag{1.3}$$

For Hamiltonian systems it also satisfies the Liouville equation

$$\frac{\partial f^{[N]}}{\partial t} = -\sum_{i=1}^{N}\left(\frac{\partial f^{[N]}}{\partial \mathbf{r}_i}\cdot\dot{\mathbf{r}}_i + \frac{\partial f^{[N]}}{\partial \mathbf{p}_i}\cdot\dot{\mathbf{p}}_i\right), \tag{1.4}$$

which simply represents the conservation of probability along the equations of motion. In equilibrium statistical mechanics, which correctly describes systems in thermodynamic equilibrium (*i.e.* systems which do not change their thermodynamic state in the absence of external forces), one looks for a stationary solution $f^{[N]}(\mathbf{r}^N, \mathbf{p}^N)$ of Eq. (1.4). Depending on the functional form of $f^{[N]}$, one introduces different *statistical ensembles*.
Using this probability density, one can define a phase-space average

$$\langle O\rangle = \iint O(\mathbf{r}^N, \mathbf{p}^N) f^{[N]}(\mathbf{r}^N, \mathbf{p}^N) d\mathbf{r}^N d\mathbf{p}^N. \tag{1.5}$$

The connection between statistical mechanics and the microscopic dynamics is based on the **ergodic hypothesis**. Consider a macroscopic mechanic observable $O(\mathbf{r}^N, \mathbf{p}^N)$ and a macroscopic observer which performs a measure on the system in order to determine its value. The measurement time is $T \gg \tau$, where τ is the characteristic time of the microscopic dynamics. The result of the measurement is not the instantaneous value of the observable, but rather a time average of the instantaneous values along the trajectories of the N particles:

$$\bar{O}_T(t_0) = \frac{1}{T}\int_{t_0}^{t_0+T} O(\mathbf{r}^N(t), \mathbf{p}^N(t))dt. \tag{1.6}$$

The ergodic hypothesis states that for systems at equilibrium

$$\lim_{T\to+\infty} \bar{O}_T(t_0) = \bar{O} = \langle O\rangle, \tag{1.7}$$

which relates time and phase-space averages. Macroscopic properties can then be evaluated by means of (not so simple) integrals over the Γ-space, by using the appropriate probability density $f^{[N]}$.

1.1 Statistical ensembles

Let us now briefly introduce some statistical ensembles, defined by the corresponding $f^{[N]}$, that we will thoroughly use throughout this thesis. We will not report the full set of ensembles or their formal derivation, which can be found in every standard statistical mechanics textbook [1–3]. Since every ensemble is closely related to a thermodynamic potential, we will then be able to set up the connection between thermodynamics and statistical mechanics.

1.1.1 Canonical ensemble

The canonical ensemble is appropriate to describe closed systems composed by N particles, kept in thermal equilibrium with a heat bath at temperature T. Energy fluctuations are explicitly taken into account. The corresponding probability

distribution function is [4]

$$f^{[N]}(\mathbf{r}^N, \mathbf{p}^N) = \frac{1}{N! h^{3N}} \frac{e^{-\beta \mathcal{H}}}{Q_N}, \tag{1.8}$$

where $\beta = \frac{1}{k_B T}$, $\mathcal{H}(\mathbf{r}^N, \mathbf{p}^N)$ is the Hamiltonian of the system and Q_N is the **canonical partition function**

$$Q_N(T, V) = \frac{1}{h^{3N} N!} \iint e^{-\beta \mathcal{H}} d\mathbf{r}^N d\mathbf{p}^N. \tag{1.9}$$

Q_N is connected to the Helmholtz free energy of the system by means of

$$F(T, V, N) = -k_B T \ln Q_N, \qquad F(T, V, N) = U(S, V, N) - TS, \tag{1.10}$$

which is a function of N,V,T. Thermodynamics follows from the partial derivatives of the free energy $F(T, V, N)$

$$dF = -SdT - PdV + \mu dN, \tag{1.11}$$

$$S = -\left(\frac{\partial F}{\partial T}\right)_{V,N} \quad P = -\left(\frac{\partial F}{\partial V}\right)_{T,N} \quad \mu = \left(\frac{\partial F}{\partial N}\right)_{T,V}. \tag{1.12}$$

It is possible to rewrite Eq. (1.9) as

$$Q_N = \frac{1}{N!} \frac{Z_N}{\Lambda^{3N}}, \qquad Z_N = \int e^{-\beta V_N} d\mathbf{r}^N, \tag{1.13}$$

where Z_N is called the **configurational integral**, by integrating out the momenta and introducing the thermal wavelength Λ

$$\Lambda = \left(\frac{2\pi\beta\hbar}{m}\right)^{\frac{1}{2}}. \tag{1.14}$$

Everything can be easily extended to the case of mixtures composed by m species with N_α particles each, $\alpha = 1, .., m$. The partition function becomes [3]

$$Q(\{N_\alpha\}, T, V) = \left(\prod_{\alpha=1}^{m} \frac{1}{\Lambda_\alpha^{3N_\alpha} N_\alpha!}\right) Z(\{N_\alpha\}),$$

$$Z(\{N_\alpha\}) = \int \left(\prod_{\alpha=1}^{m} d\mathbf{r}^{N_\alpha}\right) e^{-\beta V(N_1, N_2, ..., N_m)}, \tag{1.15}$$

where $V(N_1, N_2, ..., N_m)$ is the total interaction potential among all components. In the case of mixtures, the last relation in Eq.(1.12) applied to the set N_α defines the chemical potential μ_α of each species.

1.1.2 Grand canonical ensemble

By allowing the system to exchange energy and particles with the surrounding environment (an open system), one is led to introduce the grand canonical ensemble. This ensemble is appropriate to describe a system in a volume V, in thermal and chemical equilibrium with a reservoir at temperature T and chemical potential μ. Energy fluctuations and fluctuations in the number of particles are taken into account. The corresponding probability distribution function is [4]

$$f(\mathbf{r}^N, \mathbf{p}^N, N) = \frac{1}{\Xi}\left(\frac{1}{h^{3N}N!}\right) e^{-\beta(\mathcal{H}-N\mu)}, \tag{1.16}$$

where $f(\mathbf{r}^N, \mathbf{p}^N, N)d\mathbf{r}^N d\mathbf{p}^N$ represents the probability for the system to be composed of N particles, located around $(\mathbf{r}^N, \mathbf{p}^N)$. The normalization condition now becomes

$$\sum_{N=0}^{\infty} \iint f(\mathbf{r}^N, \mathbf{p}^N, N)d\mathbf{r}^N d\mathbf{p}^N = 1. \tag{1.17}$$

Introducing the activity $z = \exp(\beta\mu)/\Lambda^3$, the **grand canonical partition function** Ξ is

$$\Xi(T, V, \mu) = \sum_{N=0}^{\infty} \frac{e^{(N\beta\mu)}}{h^{3N}N!} \iint e^{-\beta\mathcal{H}} d\mathbf{r}^N d\mathbf{p}^N = \sum_{N=0}^{\infty} \frac{z^N}{N!} Z_N. \tag{1.18}$$

It is connected to the grand potential $\Omega(T, V, \mu)$ by

$$\Omega = -k_B T \ln \Xi \quad , \qquad \Omega = F(T, V, N) - \mu N = -PV. \tag{1.19}$$

As usual, thermodynamics follows from the partial derivatives of Ω as

$$d\Omega = -SdT - PdV - Nd\mu, \tag{1.20}$$

$$S = -\left(\frac{\partial\Omega}{\partial T}\right)_{V,\mu} \quad P = -\left(\frac{\partial\Omega}{\partial V}\right)_{T,\mu} \quad \langle N\rangle = -\left(\frac{\partial\Omega}{\partial\mu}\right)_{T,V}. \tag{1.21}$$

It is important to stress that the partial derivative of Ω with respect to μ provides the average number of particles in the system, as a function of the chemical potential μ imposed by the reservoir. In the case of mixtures [3]

$$\Xi(T, V, \{\mu_\alpha\}) = \sum_{N_1=0}^{\infty} \ldots \sum_{N_m=0}^{\infty} \left[\prod_{\alpha=1}^{m} \left(\frac{z_\alpha^{N_\alpha}}{N_\alpha!}\right)\right] Z(\{N_\alpha\}), \tag{1.22}$$

where $Z(\{N_\alpha\})$ is defined in Eq. (1.15). The average number of particle of each species $\langle N_\alpha\rangle$ is obtained by applying the last relation in Eq. (1.21) to the set μ_α.

1.2 Particle densities and distribution functions

The probability distribution functions defined in Eqs. (1.8) and (1.16) depend on the coordinates and momenta of all particles, and therefore provide a full description of the system at hand. However, it is often convenient to refer only to the distribution

of **any** subset of n particles among the N ones, which drives us to introduce the **n-particle densities**, dependent only on the subset $\mathbf{r}^n$. These functions are obtained, in the canonical ensemble, as

$$\rho_N^{(n)}(\mathbf{r}^n) = \frac{N!}{(N-n)!}\frac{1}{Q_N h^{3N} N!}\iint e^{-\beta\mathcal{H}} d\mathbf{r}^{(N-n)} d\mathbf{p}^N =$$

$$= \frac{N!}{(N-n)!}\frac{1}{Z_N}\int e^{-\beta V_N} d\mathbf{r}^{(N-n)}, \tag{1.23}$$

thus integrating out the momenta of all the N particles, the coordinates of the $N-n$ subset, and multiplying the result for the number of ways in which a subset of n particles can be chosen among the N ones. Equivalently, in the grand canonical ensemble we define

$$\rho^{(n)}(\mathbf{r}^n) = \frac{1}{\Xi}\sum_{N=n}^{\infty}\frac{z^N}{(N-n)!}\int e^{-\beta V_N} d\mathbf{r}^{(N-n)}. \tag{1.24}$$

The normalizations in the two ensembles are straightforward

$$\int \rho_N^{(n)}(\mathbf{r}^n) d\mathbf{r}^{(n)} = \frac{N!}{(N-n)!}\ , \qquad \int \rho^{(n)}(\mathbf{r}^n) d\mathbf{r}^n = \Big\langle \frac{N!}{(N-n)!}\Big\rangle, \tag{1.25}$$

and obviously for homogeneous systems we have $\rho^{(1)}(\mathbf{r}) = \rho = N/V$.
In an interacting system, the degree of correlations among particles can be characterized by means of the n-particles distribution functions

$$g_N^{(n)}(\mathbf{r}^n) = \frac{\rho_N^{(n)}(\mathbf{r}^n)}{\prod_{j=1}^n \rho_N^{(1)}(\mathbf{r}_j)}, \tag{1.26}$$

(with an analogous definition in the grand canonical ensemble) which allow one to single out the contributions of interatomic interactions, with respect to the ideal case. The definition of these quantities in mixtures is analogous but a bit long-winded, and will be taken into account only in Sec. 1.2.1 in the case of pair correlations.

1.2.1 Pair correlation functions and thermodynamics

Since a large part of the following discussion will be based on homogeneous atomic systems interacting by means of pairwise-additive interactions, it is useful to focus our attention on some thermodynamic properties concerning pair correlations. In the homogeneous and isotropic case, the pair density can be equivalently written as

$$\rho^{(2)}(|\mathbf{r}-\mathbf{r}'|) = \Big\langle \sum_{i=1}^{N}\sum_{j\neq i=1}^{N} \delta(\mathbf{r}-\mathbf{r}_i)\delta(\mathbf{r}'-\mathbf{r}_j)\Big\rangle. \tag{1.27}$$

Starting from Eq. (1.26), we can define the **pair (or radial) distribution function** $g(r)$ and the **pair correlation function** $h(r)$ as

$$g(r) = \frac{\rho^{(2)}(|\mathbf{r}-\mathbf{r}'|)}{\rho^2}, \qquad h(r) = g(r) - 1. \tag{1.28}$$

Several thermodynamic observables can be related to these quantities. In the grand canonical ensemble, is it possible to connect $g(r)$ to the isothermal compressibility κ_T and the fluctuation in the number of particle [4]:

$$\kappa_T = -\frac{1}{V}\left(\frac{\partial V}{\partial P}\right)_T = \frac{\beta}{\rho}\frac{\langle(\Delta N)^2\rangle}{\langle N\rangle}. \tag{1.29}$$

By using Eq. (1.25), in the homogeneous case one obtains

$$1 + \rho\int (g(r)-1)\, d\mathbf{r} = \frac{\langle N^2\rangle - \langle N\rangle^2}{\langle N\rangle} = \rho k_B T \kappa_T, \tag{1.30}$$

which relates $g(r)$ to κ_T. Defining the **structure factor** $S(\mathbf{q})$ as

$$S(\mathbf{q}) = 1 + \rho\int g(r) e^{-i\mathbf{q}\cdot\mathbf{r}} d\mathbf{r} = 1 + \left\langle \frac{1}{N}\sum_{i=1}^{N}\sum_{j\neq i}^{N} e^{-i\mathbf{q}\cdot(\mathbf{r}_i - \mathbf{r}_j)}\right\rangle, \tag{1.31}$$

we have, apart from a $\delta(\mathbf{q})$ term,

$$\lim_{\mathbf{q}\to 0} S(\mathbf{q}) = \rho k_B T \kappa_T. \tag{1.32}$$

Eqs. (1.30)-(1.32) are valid for arbitrary interatomic interactions.
Consider now the Hamiltonian of Eq. (1.2), again with $\Phi_N = 0$ but with a total interatomic potential

$$V_N(\mathbf{r}_1, \mathbf{r}_2, ..., \mathbf{r}_N) = \sum_{j>i=1}^{N} v(|\mathbf{r}_i - \mathbf{r}_j|). \tag{1.33}$$

In the presence of pairwise additive interactions (1.33), the virial pressure P^v can be computed by means of the radial distribution function $g(r)$ [4]:

$$Z = \frac{\beta P^v}{\rho} = 1 - \frac{\beta}{3N}\Big\langle \sum_{i=0}^{N} \mathbf{r}_i \cdot \nabla_i V_N(\mathbf{r}^N)\Big\rangle = \tag{1.34}$$

$$= 1 - \frac{2\pi\beta\rho}{3}\int_0^\infty \frac{\partial v(r)}{\partial r} g(r) r^3 dr, \tag{1.35}$$

which is nothing but the virial theorem.
These results can be extended to mixtures. The pair density tensor $\rho^{(2)}_{\alpha\beta}$, $\alpha, \beta = 1, \ldots, m$, among different species is defined by [6]:

$$\rho^{(2)}_{\alpha\beta}(\mathbf{r}, \mathbf{r}') = \Big\langle \sum_{i_\alpha=1}^{N_\alpha}\sum_{j_\beta=1}^{N_\beta}{}' \delta(\mathbf{r} - \mathbf{r}_{i_\alpha})\delta(\mathbf{r}' - \mathbf{r}_{j_\beta})\Big\rangle, \qquad \int d\mathbf{r} d\mathbf{r}' \rho^{(2)}_{\alpha\beta}(\mathbf{r}, \mathbf{r}') = N_\alpha(N_\beta - \delta_{\alpha\beta}), \tag{1.36}$$

where the prime in the second sum of the first relation simply indicates that, if $\beta = \alpha$, the term $i_\alpha = j_\alpha$ must be omitted. As for the single component case, the radial distribution tensor $g_{\alpha\beta}(r)$ and the pair correlation tensor $h_{\alpha\beta}(r)$ then follow:

$$g_{\alpha\beta}(r) = \frac{\rho^{(2)}_{\alpha\beta}(r)}{\rho_\alpha \rho_\beta}, \qquad h_{\alpha\beta}(r) = g_{\alpha\beta}(r) - 1, \tag{1.37}$$

where $\rho_\alpha = N_\alpha/V$ is the number density of species α.
Starting from the pair correlation tensor, one defines the **partial structure factors**

$$S_{\alpha\beta}(\mathbf{q}) = \delta_{\alpha\beta} + \sqrt{\rho_\alpha \rho_\beta}\hat{h}_{\alpha\beta}(\mathbf{q}), \tag{1.38}$$

where we identify $\hat{f}(\mathbf{q})$ with the (three-dimensional) Fourier transform of a function $f(r)$

$$\hat{f}(\mathbf{q}) = \int f(r) e^{-i\mathbf{q}\cdot\mathbf{r}} d\mathbf{r}. \tag{1.39}$$

For a binary mixture, from the structure factors in Eq. (1.38) the concentration structure factor can be defined as

$$S_c(k) = x_1 x_2 \left[x_1 S_{22}(k) + x_2 S_{11}(k) - 2\sqrt{x_1 x_2} S_{12}(k)\right], \tag{1.40}$$

where $x_\alpha = \rho_\alpha/(\rho_1 + \rho_2)$ is the molar fraction of species $\alpha = 1, 2$.
For $k \to 0$, $1/S_c(k) \to \partial^2 \beta g(x_1, P)/\partial x_p^2$, where $g(x_p, P)$ is the Gibbs free energy per particle. Hence, its divergence signals the thermodynamic instability of the homogeneous phase. In the presence of pairwise additive interatomic interactions, the virial equation for mixtures becomes:

$$Z = \frac{\beta P^v}{\rho} = 1 - \sum_{\alpha,\gamma=1}^{m} \frac{2\pi\beta}{3\rho} \rho_\alpha \rho_\gamma \int_0^\infty \frac{\partial v_{\alpha\gamma}(r)}{\partial r} g_{\alpha\gamma}(r) r^3 dr, \tag{1.41}$$

where $\rho = \sum_\alpha \rho_\alpha$ and $v_{\alpha\gamma}(r)$ is the interaction potential among species α and γ.
Therefore, some thermodynamics observables for the system can be determined as soon as the pair distribution functions $g_{\alpha\beta}(r)$ are known.

1.3 Integral equation methods

Integral equation methods [3, 4] are a very powerful tool to determine the thermodynamics and the liquid structure of simple fluids, both for single-component systems and for mixtures. They rely on the Ornstein-Zernike (OZ) relation, supported by an appropriate approximate closure relation. Even if these methods cannot compete nowadays with exact approaches such as molecular dynamics or Monte-Carlo methods, they can provide quantitatively or at least qualitatively accurate results with a very limited computational efforts. We will now present a short review of the basics of integral equation methods in a general fashion, focusing on the OZ relation and on the closure relations we will use in the discussion. The critical analysis of integral-equation predictions on polymer solutions and colloid-polymer mixtures will be presented in Chaps. 4 and 5.

1.3.1 Ornstein-Zernike relation

The main ingredient in integral equation methods is the Ornstein-Zernike relation. Here, we will not provide its exact derivation which can be found in Ref. [4]. This relation connects the pair correlation function $h(r)$ defined in Eq. (1.28) and the so-called **direct correlation function** $c(r)$, which characterizes the free-energy

fluctuations of the system in response to density fluctuations (for a formal definition see Ref. [4]). The OZ relation reads

$$h(\mathbf{r}) = c(\mathbf{r}) + \rho \int c(\mathbf{r} - \mathbf{r}')h(\mathbf{r}')d\mathbf{r}', \tag{1.42}$$

or in Fourier space

$$\hat{h}(\mathbf{k}) = \hat{c}(\mathbf{k}) + \rho\hat{c}(\mathbf{k})\hat{h}(\mathbf{k}). \tag{1.43}$$

In terms of the structure factor $S(\mathbf{k})$ defined in Eq. (1.31), the Ornstein-Zernike relation can be written as

$$S(\mathbf{k}) = \frac{1}{1 - \rho\hat{c}(\mathbf{k})}. \tag{1.44}$$

A solution in series of Eq. (1.42) makes clear how the total correlation $h(r)$ between two particles is due to the direct correlation, plus a series in direct contributions mediated by the presence of all the other particles in the system. For mixtures, the OZ relation connects the pair correlation tensor $h_{\alpha\gamma}(r)$ and the direct correlation tensor $c_{\alpha\gamma}(r)$ by

$$\hat{h}_{\alpha\gamma}(\mathbf{k}) = \hat{c}_{\alpha\gamma}(\mathbf{k}) + \sum_{\nu} \hat{c}_{\alpha\nu}(\mathbf{k})\rho_\nu\hat{h}_{\nu\gamma}(\mathbf{k}). \tag{1.45}$$

To compute the quantities of interest, $h_{\alpha\gamma}$ and $c_{\alpha\gamma}$, Eqs. (1.43) or (1.45) must be supplemented by another set of relations between them, which are commonly referred to as closure relations. It is possible to show, by means of the diagrammatic cluster expansion [3][4], that the general form of a closure relation can be written as

$$g_{\alpha\gamma}(r) = e^{-\beta v_{\alpha\gamma}(r)} \exp[h_{\alpha\gamma}(r) - c_{\alpha\gamma}(r) + b_{\alpha\gamma}(r)]. \tag{1.46}$$

We remind that the $g_{\alpha\gamma}$ are related to the $h_{\alpha\gamma}$ by means of Eq. (1.37).
The set $b_{\alpha\gamma}(r)$ are the so-called bridge functions of the system and cannot be computed exactly in a closed form, hence approximations must be introduced. Every approximation, or closure relation, is based upon a different form of the set $b_{\alpha\gamma}$, as discussed in Sec. 1.3.2.

1.3.2 Closure relations

A large variety of approximate closure relations for the Ornstein-Zernike equation have been proposed and analyzed in the literature, and the limits of validity of each of them have been fully determined [3, 4].
In this section, we present the closure relations we will use in the analysis of polymer solutions and colloid-polymer mixtures, which are the hypernetted-chain, the Percus-Yevick, the Rogers-Young and the reference hypernetted-chain approximations. Our choice is mainly dictated by their well-established accuracy in the prediction of the thermodynamic properties for the class of potentials we will be dealing with [4, 12, 15]. Other well-known approximate closure relations exist, *e.g.*, the mean-spherical approximation, the Ornstein-Zernike approximation and the random-phase approximation, whose functional form will be omitted here for the sake of brevity. For further details the reader may refer to Ref. [4].

1.3.2.1 Hypernetted-chain

The hypernetted-chain (HNC) approximation is obtained by setting $b_{\alpha\gamma}(r) = 0$, hence we have

$$g_{\alpha\gamma}(r) = e^{-\beta v_{\alpha\gamma}(r)} \exp[h_{\alpha\gamma}(r) - c_{\alpha\gamma}(r)]. \tag{1.47}$$

HNC has proven to be very accurate for potentials which are soft on short ranges [4]. Using this approximation, it is possible to compute the chemical potential μ, both for single-component systems [7][8] and for mixtures [9]:

$$\beta\mu = \beta\mu_{id} + \frac{\rho}{2}\int h(\mathbf{r})[h(\mathbf{r}) - c(\mathbf{r})]d\mathbf{r} - \rho\int c(\mathbf{r})d\mathbf{r}, \tag{1.48}$$

$$\beta\mu_\alpha = \beta\mu_{id,\alpha} + \sum_\gamma \left(\frac{\rho_\gamma}{2}\int h_{\alpha\gamma}(\mathbf{r})[h_{\alpha\gamma}(\mathbf{r}) - c_{\alpha\gamma}(\mathbf{r})]d\mathbf{r} - \rho_\gamma\int c_{\alpha\gamma}(\mathbf{r})d\mathbf{r}\right), \tag{1.49}$$

where μ_{id} is the ideal contribution to the chemical potential.

1.3.2.2 Percus-Yevick

The Percus-Yevick (PY) approximation [4] consists in setting

$$g_{\alpha\gamma}(r) = e^{-\beta v_{\alpha\gamma}(r)}[1 + h_{\alpha\gamma}(r) - c_{\alpha\gamma}(r)], \tag{1.50}$$

and can be seen as the linearization of the HNC closure in $(h_{\alpha\gamma} - c_{\alpha\gamma})$. It has proven to be accurate in the case of short range, hard-core potentials, and has been widely applied in the context of hard-sphere systems [10, 11]. The reason for its reliability in the context of short-range, hard potentials is that in comparison with the HNC approximation, it reintroduces a set of approximate bridge functions $b_{\alpha\gamma}$, which are proven to be relevant on short distances. By comparing Eq. (1.46) with Eq. (1.50) one can define

$$b^{PY}_{\alpha\gamma}(r) = \ln[1 + h_{\alpha\gamma}(r) - c_{\alpha\gamma}(r)] - [h_{\alpha\gamma}(r) - c_{\alpha\gamma}(r)]. \tag{1.51}$$

1.3.2.3 Rogers-Young

Both the HNC and PY approximation suffer from thermodynamic inconsistency in the computation of thermodynamic properties. Indeed, if one computes the isothermal compressibility κ_T by means of Eq. (1.30) or as the derivative of the virial pressure P^v in Eq. (1.35) (also called the virial route) as

$$\frac{\beta}{\kappa_T} = \rho\frac{\partial P^v}{\partial\rho}, \tag{1.52}$$

two different results are obtained. The Rogers-Young (RY) closure [12] makes use of an adjustable parameter in order to obtain thermodynamic consistency. It reads

$$g(r) = e^{-\beta v(r)}\left[1 + \frac{\exp[(h(r) - c(r))f(r)] - 1}{f(r)}\right], \tag{1.53}$$

where the function $f(r)$ is given by

$$f = 1 - e^{-\chi r}. \tag{1.54}$$

The parameter χ is determined numerically by requiring compatibility of the two different compressibilities in Eq. (1.30) and (1.52). The RY closure interpolates between the HNC and PY closures. Indeed, for $\chi \to 0$ one obtains the PY closure, while in the opposite limit $\chi \to \infty$ HNC is recovered.
In mixtures, different results for the isothermal compressibility are obtained if one uses the virial route

$$\frac{\beta}{\kappa_T} = \sum_{\alpha=1}^{m} \rho_\alpha \left(\frac{\partial \beta P^v}{\partial \rho_\alpha} \right)_{\{\rho_\gamma\}}, \tag{1.55}$$

or [5]

$$\frac{\beta}{\kappa_T} = \sum_{\alpha} \rho_\alpha - \sum_{\alpha\beta} \rho_\alpha \rho_\beta \hat{c}_{\alpha\beta}(0), \tag{1.56}$$

where the $\hat{c}_{\alpha\beta}$ are defined in Eq. (1.45). In this case, the generalization of RY closure reads [13]:

$$g_{\alpha\beta}(r) = e^{-\beta V_{\alpha\beta}(r)} \left[1 + \frac{\exp[(h_{\alpha\beta}(r) - c_{\alpha\beta}(r)) f_{\alpha\beta}(r)] - 1}{f_{\alpha\beta}(r)} \right], \tag{1.57}$$

where again $f_{\alpha\beta}(r)$ is

$$f_{\alpha\beta} = 1 - e^{-\chi_{\alpha\beta} r}. \tag{1.58}$$

There is no clear prescription on the choice of the set $\chi_{\alpha\beta}$. In most of the cases, when the components have characteristic sizes σ_α, a single optimization parameter is used by choosing $\chi_{\alpha\beta} = \chi/\sigma_{\alpha\beta}$, where $\sigma_{\alpha\beta} = \frac{1}{2}(\sigma_\alpha + \sigma_\beta)$.

1.3.2.4 Reference-HNC

The Reference-HNC or RHNC closure uses the bridge functions of a reference hard-sphere system. For single-component systems [14], it is assumed that the bridge function $b(r)$ can be replaced by the bridge function of a system of hard spheres with an appropriate diameter d, at the same density ρ of the original system:

$$b(r) = b^{\mathrm{HS}}(r, d, \rho). \tag{1.59}$$

The appropriate diameter d is obtained by means of the Lado criterion [16]

$$\int d\mathbf{r} [g(r) - g^{\mathrm{HS}}(r, d)] \frac{\partial b^{\mathrm{HS}}(r, d, \rho)}{\partial d} = 0. \tag{1.60}$$

In Eq. (1.60), $g^{\mathrm{HS}}(r, d)$ is the pair distribution function of a hard-sphere system of diameter d at the same density of the original system. Both g^{HS} and b^{HS} can be computed quite precisely, starting from the analytical solution of the PY equation for hard spheres [10] and applying some corrections [17, 18].
The generalization to mixtures is straightforward [15]. In this case the whole set $b_{\alpha\beta}$ has to be replaced with that of a mixture of additives hard spheres with appropriate diameters d_α, and at the same densities ρ_α of the original system:

$$b_{\alpha\beta}(r, \{\rho_\alpha\}) = b^{\mathrm{HS}}_{\alpha\beta}(r, \{d_\alpha\}, \{\rho_\alpha\}). \tag{1.61}$$

Each bridge function depends on the whole set of diameters d_α. The generalization of the Lado criterion reads [15]

$$I_k = \sum_{\alpha,\beta=1}^{m} x_\alpha x_\beta \int d\mathbf{r}[g_{\alpha\beta}(r) - g_{\alpha\beta}^{\mathrm{HS}}(r,\{d_\alpha\})]\frac{\partial b_{\alpha\beta}^{\mathrm{HS}}(r,\{d_\alpha\})}{\partial d_k} = 0, \quad \forall k = 1..m, \tag{1.62}$$

where $x_\alpha = \rho_\alpha / \left(\sum_\alpha \rho_\alpha\right)$ is the mole fraction of species α. The set of functions $g_{\alpha\beta}^{\mathrm{HS}}$ and $b_{\alpha\beta}^{\mathrm{HS}}$ can again be computed starting from the analytical solution of the PY equation for mixtures of additive hard spheres [11], and correcting the results by means of some exact theorems and numerical prescriptions [15, 19–22].

Chapter 2

Polymer Physics

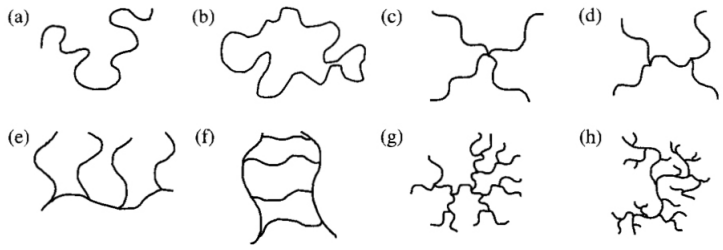

Figure 2.1. Polymer architectures [28]: linear (a), ring (b), star (c), H (d), comb (e), ladder (f), dendrimer (g), randomly branched (h).

Polymers are systems of great interest under a physical and chemical point of view, due to their well known technological applications and their connection with biological systems. The first theoretical studies date back to the works of Flory in the first half of the 20th century [23], followed by those of de Gennes, Edwards, Khokhlov, des Cloizeaux and many others, who set up the modern theory of polymers.
In this chapter, we present some general results, obtained by applying statistical mechanics methods to the analysis of polymer systems, with no claim of being exhaustive: for more details the reader may refer to Refs. [23–28]. We discuss polymer solutions in the dilute and semidilute regime. Under these conditions, they show universal properties, independent of chemical details and to a large extent also of temperature. This universality is connected to the criticality of polymer solutions, in the language of the modern theory of critical phenomena [29–31]. We will then focus on the description of the good-solvent regime, presenting some results obtained from scaling theories and renormalization-group methods. The application of these concepts to linear chains and star polymers is postponed to Chaps. 3 and 4.

2.1 General features

Polymers are a typical soft-matter system: each molecule is made up of $L \gg 1$ fundamental chemical units called **monomers**, linked together by covalent bonds. L is called the **degree of polymerization**. Depending on the number of different

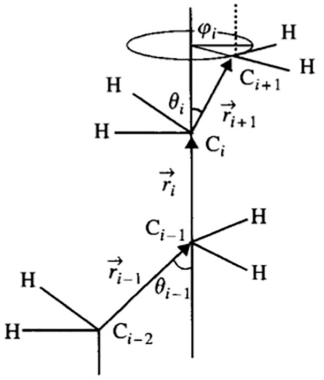

Figure 2.2. A molecule of polyethylene, build-up from the repetition of group CH_2 [28].

chemical units n along the molecule, one speaks of **homopolymers** ($n = 1$) or **heteropolymers** ($n > 1$), with very different chemical properties [23].
A second characterization can be based on the mesoscopic architecture of polymers. Several structures are possible; some of them are shown in Fig 2.1. The covalent bonds created in the polymerization process are very strong and cannot be broken easily: hence, the polymer architecture is quite stable. On the other hand, the relative orientations of the bonds can easily change and therefore polymers can assume several different space configurations. Each of them can be specified by the position vectors of the backbone atoms of the molecule $\mathbf{R}_i$, $i = 1...L$, or equivalently by the bond vectors between two subsequent atoms $\mathbf{r}_i = \mathbf{R}_{i+1} - \mathbf{R}_i$ [28], as shown in Fig 2.2. Configurational properties describing the molecule as a whole can be defined. The average size of a polymer is tipically characterized by its **radius of gyration**

$$R_g^2 = \frac{1}{N}\sum_{i=1}^{N}(\mathbf{R}_i - \mathbf{R}_{cm})^2, \tag{2.1}$$

and its average

$$\hat{R}_g^2 = \frac{1}{N}\sum_{i=1}^{N}\langle(\mathbf{R}_i - \mathbf{R}_{cm})^2\rangle = \frac{1}{2N^2}\sum_{i,j=1}^{N}\langle(\mathbf{R}_i - \mathbf{R}_j)^2\rangle. \tag{2.2}$$

$\mathbf{R}_{cm}$ is the center of mass of the molecule and the statistical average $\langle ... \rangle$ is performed over all microscopic configurations of the system.
In real polymeric systems, monomers mutually interact in a very complex way. However, to obtain some qualitative informations on the behavior of the solution it is useful to consider **ideal models**, in which interactions among units i, j far away along the molecule, $|i - j| \gg 1$, are neglected (or exponentially vanishing). Although unrealistic, these models are important in the context of θ-solvents. In **real models**, there are non-vanishing interactions among all microscopic units [25].

Due to the complexity of the microscopic structure, the chemical and physical properties of these systems strongly depend on the microscopic details. Despite this,

it is now well established that polymer solutions, to be defined in Sec. 2.2, exhibit separation of scales: at distances of the order of the bond length local properties significantly depend on the microscopic structure of monomers. At a mesoscopic and macroscopic level one has instead global properties, which do not depend on the microscopic details [24–26]. Indeed, for $L \gg 1$, polymer systems and several simple models show the same large-scale universal behavior, as soon as they have the same microscopic architecture and are in the same solvent regime. In the limit $L \to \infty$, the average of several physical observables follows the scale behavior

$$\langle O_L \rangle \sim L^p, \tag{2.3}$$

with model-dependent prefactors, but with a universal exponent p characterizing the observable. For example, the average radius of gyration scales as

$$\hat{R}_g \sim L^\nu b \tag{2.4}$$

in polymer solutions, where b is a characteristic microscopic length and ν is a universal exponent, which depends only on the quality of the solvent [24, 27, 29–31]. Microscopic models which show the same exponents for the same observables in the large-scale limit are said to belong to the same **universality class** (in the standard renormalization group formalism).
The scaling law in Eq. (2.3) is strictly valid only in the limit $L \to \infty$: for L large but finite, one should take care of corrections to scaling, which for a generic observable read

$$\langle O_L \rangle \sim L^p \left(1 + \frac{a_1}{L} + \frac{a_2}{L^2} + ... + \frac{b_0}{L^{\Delta_1}} + \frac{b_1}{L^{\Delta_1+1}} + ... + \frac{c_0}{L^{\Delta_2}} + \frac{c_1}{L^{\Delta_2+1}} + ...\right). \tag{2.5}$$

In Eq. (2.5), the exponents $\Delta_1 < \Delta_2 < ...$ are again universal, but with model-dependent prefactors $(a_1, a_2, ..., b_0, b_1, ..., c_0, c_1, ...)$.
Beside scaling laws, also adimensional ratios of large-scale or thermodynamic observables are universal, when expressed in terms of appropriate adimensional variables: this is the case of the osmotic coefficient $Z(\rho_p) = \beta P(\rho_p)/\rho_p$, where P is the osmotic pressure and ρ_p is the polymer number density, which for $L \to \infty$ tends to a universal function F^* of the adimensional combination $\rho_p \hat{R}_g^3$ [30]:

$$Z(\rho_p) \underset{L\to\infty}{\longrightarrow} 1 + F^*(\rho_p \hat{R}_g^3). \tag{2.6}$$

In this thesis, we will consider only the universal long-wavelength behavior of homopolymers. Universality implies that thermodynamic properties, computed in the framework of a convenient microscopic model, apply to all models which belong to the same large-scale universality class.

2.2 Polymer solutions

A polymer solution is obtained by dissolving N_p molecules in a solvent: the concentration is usually characterized by the **volume fraction**

$$\Phi_p = \frac{4\pi}{3V} N_p \hat{R}_g^3 = \frac{4\pi}{3} \rho_p \hat{R}_g^3, \tag{2.7}$$

where $\rho_p = N_p/V$. Φ_p is simply the ratio of the total average volume occupied by the polymers (considered as spheres of average radius $\hat{R}_g$) and the volume of the container V. If $\Phi_p \lesssim 1$, different polymer coils do not overlap and a **dilute solution** is obtained. Overlaps begin to occur at a density

$$\rho_p^* = \frac{1}{V_p} = \frac{1}{4/3\pi\hat{R}_g^3}, \tag{2.8}$$

i.e. for $\Phi_p = \rho_p/\rho_p^* \approx 1$. A **semidilute solution** is obtained for $\Phi_p \gtrsim 1$, provided that the monomer density $\rho_m = LN_p/V$ is small. Otherwise, one enters the **concentrated** or **melt** regime.

The solubility of a polymer in a solvent depends on the affinity between the components, that is on the monomer-solvent as well as on the monomer-monomer interactions. Integrating out the solvent molecules, the system can be approximately represented as a set of monomers interacting by means of an effective pair potential $v(r)$, which takes into account the average effect of the solvent. This potential has a short-range, repulsive shape plus an attractive tail, whose presence and depth are connected to the monomer-solvent repulsion. In principle, integrating out the solvent introduces many-body effective interactions among monomers [32], but the contributions of 3-body, 4-body, etc. interaction terms are negligible for low-monomer concentrations and in good solvents [31].

As discussed in Sec. 2.1, the specific microscopic interaction among the monomers is supposed to have a weak influence on the large-scale behavior of the system, which is only determined by some general features, shared by a large class of microscopic models [31]. Relying on these assumptions, in a very crude mean-field approximation, one classifies the solvent quality according to the value of the monomeric second virial coefficient or **excluded-volume parameter**

$$b(T) = -\frac{1}{2}\int d\mathbf{r}(e^{-\beta v(r)} - 1) = -\frac{1}{2}\int d\mathbf{r} f(r), \tag{2.9}$$

where $f(r)$ is the Mayer function

$$f(r) = e^{-\beta v(r)} - 1. \tag{2.10}$$

The sign of b is only dependent on the trade-off between the short-range repulsion and the solvent-induced attraction between the monomers. It should be noted that the hard-core repulsive interaction gives a positive contribution to the excluded volume, while the attractive tail gives a negative one.

Good solvents are those for which $b > 0$: here the repulsion among the monomers is stronger than that between monomer and solvent. Polymers tend to swell in order to minimize monomer-monomer contacts. As soon as $L \to \infty$ and in three dimensions, these systems fall into the universality class of **self-avoiding walks**, with an universal exponent $\nu \approx 0.588$ [24, 26], as defined in Eq. (2.4).

The temperature T_θ at which $b(T_\theta) \approx 0$ defines **θ-solvents**, in which the two contributions balance and the two-body effective interaction is zero. Here, the polymers behave nearly as ideal (with deviations from ideality due to 3-body interactions) and belong to the **random walk** universality class for $L \to \infty$, with $\nu = 1/2$. For $T < T_\theta$ and $b < 0$, in **poor solvents**, the dominance of repulsion between monomers

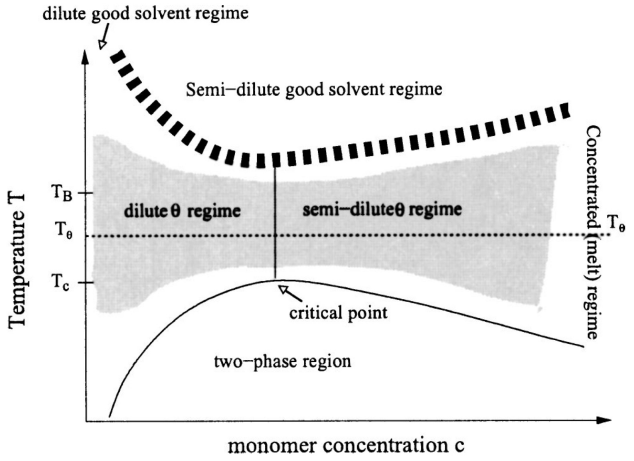

Figure 2.3. Temperature-concentration phase diagram of a polymer solution for finite values of L [33]. The dashed line is the boundary of a semidilute good solvent solution, while the full line below T_θ is the binodal line for phase separation in poor solvents. The shaded area indicates polymers that behave almost as in θ conditions.

and solvent molecules causes the polymers to collapse into globules, with $\nu \approx 1/3$. The classification based on the value of $b(T)$ is approximate, as it is only based on energy considerations and does not take into account the entropic contributions, i.e. the fact that the number of typical configurations is different in the two phases. A thermodynamically consistent definition of the θ-point takes into account the polymer second virial coefficient $B_2(T)$ [24]. It is defined by the expansion of the osmotic coefficient $Z = \beta P/\rho_p$, as a function of the polymer density ρ_p

$$Z = 1 + B_2(T)\rho_p + B_3(T)\rho_p^2 + ... \tag{2.11}$$

In the mean-field Flory-Huggins lattice theory [24, 28] we have $B_2(T) \propto (1 - 2\chi)$, with

$$\chi = \frac{\beta}{2}\left(2u_{\rm sm} - u_{\rm ss} - u_{\rm mm}\right). \tag{2.12}$$

The $u_{\alpha\beta}$ are the monomer-monomer, solvent-monomer and solvent-solvent interaction energies, therefore χ clearly represents the relative affinity of the components. In this model, θ-solvents are characterized by $\chi = 1/2$, good-solvents by $\chi < 1/2$ and poor solvents by $\chi > 1/2$. Thus, θ-solvents are characterized by a vanishing polymer second virial coefficient.

Even if we will be dealing only with polymers in good solvents, it is interesting to briefly discuss the phase diagram of a polymer solution in the poor-solvent case, since it shares some qualitative features with the fluid-fluid phase separation exhibited by colloid-polymer mixtures, which will be analyzed in Chap. 4. As we said, in poor solvents the monomer-solvent repulsion is greater than the monomer-monomer one, and this causes the polymer to collapse. This repulsion can become so predominant that polymers aggregate in order to expel the solvent, causing the system to demix into two phases, a polymer-poor/solvent-rich one and a polymer-rich/solvent-poor one. The overall phase behavior of a polymer solution for finite values of L is shown

in Fig. 2.3. In addiction to the θ temperature T_θ defined above, the temperatures T_B and T_C are shown. The former is the temperature at which the virial coefficient $B_2(T, L)$ vanishes. The temperature T_C in the poor-solvent regime is the critical temperature at which the aforementioned phase separation occurs [33]. In the scaling limit $L \to \infty$, we have $T_C \to T_\theta$ and $T_B \to T_\theta$. The shaded area in 2.3 represents the region in which finite L polymers behave approximately as θ-polymers. It becomes a line in the limit $L \to \infty$, and the transition from good to θ-solvents becomes sharp. In the large monomer concentration region of Fig 2.3, one has **concentrated solutions or polymer melts**. In this regime, the system exhibits a **screening of the excluded-volume interactions**: repulsion among the monomers vanishes on average and each polymer behaves essentially as in the ideal case, with random-walk statistics [24, 28]. This mechanism, although rather counterintuitive, can be qualitatively explained. The swelling of polymers in good solvents aims at reducing contacts among monomers, as a consequence of the intramolecular repulsive interactions. However, in concentrated solutions the interstitial volume of a molecule is completely filled by monomers belonging to other molecules. Therefore, the swelling is no more an efficient way of reducing the intramolecular interaction energy, since there is at the same time an intermolecular repulsion with all the other molecules in the system. Effectively, the monomer repulsive interaction vanishes. The screening of excluded volume interactions turns out to be important in the description of semidilute solutions in terms of correlation blobs, which will be presented in Sec. 2.3.3.

2.3 Polymers in good solvents

In this thesis, we will be mainly interested in the characterization of linear chains and star polymers in good solvents, both in the dilute and semidilute regime. This section will therefore focus on some general aspects of good-solvent solutions.
We will begin the discussion by presenting several simple models that are frequently used as a "microscopic" description of polymers. It is important to stress that these model are not representative of a real microscopic structure, but they all belong to the universality class of polymers in good solvents. Therefore, they are able to capture the correct universal large-scale behavior of the system for $L \to \infty$.
We will then report some results concerning structural and thermodynamic properties in the dilute regime. The notion of correlation length [24, 27, 28] will be introduced. Scaling theories and correlation blobs will then allow us to make some simple predictions concerning polymer solutions in the semidilute regime.

2.3.1 Microscopic models

Among all the microscopic models describing polymers in good solvents, we can make a first distinction between **continuum** and **lattice** models. In the former, the bond vectors are allowed to move in the continuous three-dimensional space, while in the latter they can only belong to the sites of a lattice. The discrete and field-theoretical **Edwards model** [30, 31] are two examples of continuum models. In the discrete Edwards model, a system of N_p polymers of L monomers located at

$\{\mathbf{r}_{\alpha,j}\}$, $\alpha = 1, ..., N_p$, $j = 1, ..., L$ is described by a probability distribution function

$$P(\{\mathbf{r}_{\alpha,j}\}) = \frac{1}{Z(N_p)} \exp\left[-V\{\mathbf{r}_{\alpha,j}\}\right], \tag{2.13}$$

where

$$\begin{aligned}\exp\left[-V\right] = &\exp\left\{-\frac{1}{2l^2}\sum_{\alpha=1}^{N_p}\sum_{j=1}^{L}\left(\mathbf{r}_{\alpha,j} - \mathbf{r}_{\alpha,j-1}\right)\right\} \\ &\prod_{(\alpha,i)(\beta,j)}\left[1 - \frac{v}{2}\delta(\mathbf{r}_{\alpha,i} - \mathbf{r}_{\beta,j})\right],\end{aligned} \tag{2.14}$$

and the product extends over all pairs of distinct monomers. In this model each polymer is represented as a set of particles connected by harmonic potentials, with a repulsive interaction which occurs between all monomers parametrized by a delta function. For $v = 0$, one obviously recovers the Gaussian (ideal) chain. $Z(N_p)$ is the canonical partition function

$$Z(N_p) = \int \left(\prod_{\alpha=0}^{N_p}\prod_{j=0}^{L} d\mathbf{r}_{\alpha,j}\right) \exp\left[-V\{\mathbf{r}_{\alpha,j}\}\right], \tag{2.15}$$

and the average of an observable $O(\{\mathbf{r}_j^m\})$ in the canonical ensemble reads

$$\langle O\rangle = \int \left(\prod_{\alpha=0}^{N_p}\prod_{j=0}^{L} d\mathbf{r}_{\alpha,j}\right) P(\{\mathbf{r}_{\alpha,j}\})O(\{\mathbf{r}_{\alpha,j}\}). \tag{2.16}$$

The generalization to the grand canonical ensemble is straightforward. The discrete Edwards model can be (with some mathematical care) extended to the continuum case, where the configuration of a chain is represented by a vector $\mathbf{r}_\alpha(s)$, $\alpha = 1, ..., N_p$, which is now function of the continuous parameter s. The weight of a configuration then reads

$$P[\{\mathbf{r}_\alpha(s)\}] = \frac{1}{Z(N_p)} \exp(-W[\{\mathbf{r}_\alpha(s)\}]) \tag{2.17}$$

where

$$W[\{\mathbf{r}_\alpha(s)\}] = \frac{1}{2}\sum_{\alpha=0}^{N_p}\int ds \left[\frac{d\mathbf{r}_\alpha(s)}{ds}\right]^2 + \frac{v}{2}\sum_{\alpha,\beta}^{N_p}\int ds \int ds' \delta(\mathbf{r}_\alpha(s) - \mathbf{r}_\beta(s')). \tag{2.18}$$

The canonical partition function now becomes

$$Z(N_p) = \int \left(\prod_{\alpha=1}^{N_p} D[\mathbf{r}_\alpha(s)]\right) \exp(-W[\{\mathbf{r}_\alpha(s)\}]), \tag{2.19}$$

and the average of an observable $O[\{\mathbf{r}_\alpha(s)\}]$ is

$$\langle O\rangle = \int \left(\prod_{\alpha=1}^{N_p} D[\mathbf{r}_\alpha(s)]\right) P[\{\mathbf{r}_\alpha(s)\}]O[\{\mathbf{r}_\alpha(s)\}], \tag{2.20}$$

where $D[\mathbf{r}_\alpha]$ stands for a functional integration among all the possible configurations of all the chains. The structure of the model in Eq. (2.18) clearly resembles its discrete counterpart (2.14), with a connectivity term and a repulsion parametrized by v. Again, for $v = 0$ one obtains the continuous Gaussian chain model.
Most of the pioneering theoretical work on polymer solutions has been based on these two continuous model [29–31]. However, in a numerical approach it is sometimes more convenient to introduce discrete models, in which polymers are represented as random walks on a lattice. In this thesis, full-monomer properties were computed by means of Monte Carlo simulations of the **lattice Self-Avoiding Walk** (SAW) [34] and **Domb-Joyce models** (DJ) [35]. Both in the SAW and DJ models, each molecule is defined as an ordered set of points $\{\mathbf{r}_{\alpha,1}....\mathbf{r}_{\alpha,L}\}$, $\alpha = 1, ..., N_p$, in which $\mathbf{r}_{\alpha,i}$ and $\mathbf{r}_{\alpha,i+1}$ are lattice nearest neighbors. The degree of polymerization L is the number of lattice points occupied by each molecule.
In the SAW, the intersections of a walk with itself or with the other walks are forbidden. Although the SAW model has been extensively studied in the last century and its features are nowadays well known, it presents several disadvantages:

- In the implementation of Monte Carlo simulations, one should carefully consider the trial moves used. Indeed, the ergodicity of the algorithm is often not obvious [34].
- SAW results present large scaling corrections of the form defined in Eq. (2.5).
- At high density, the impossibility of walks to intersect sharply reduces the acceptance of the moves and the simulation time increases.
- In the case of star polymers, several different chains are tethered to a common core [46]. This is a complex task in the SAW framework for high values of the functionality f. In the literature this was accomplished by connecting the endpoints of the chains to a central extended core. As a consequence, large scaling corrections are present: indeed, the scaling limit is only obtained when $\hat{R}_g$ is much larger than the size of the core.

We can overcome most of these problems by decreasing the magnitude of the repulsion between monomers and introducing the Domb-Joyce model [35]. It has the same lattice representation of the SAW but intersections are possible, although penalized by a factor w. The energy of the system is obtained by counting the number of intramolecular and intermolecular intersections among walks

$$E = \left[\sum_{\alpha=1}^{N_p}\sum_{i<j=1}^{L}\delta(\mathbf{r}_{\alpha,i},\mathbf{r}_{\alpha,j})\right] + \left[\sum_{\alpha<\beta=1}^{N_p}\sum_{i,j=1}^{L}\delta(\mathbf{r}_{\alpha,i},\mathbf{r}_{\beta,j})\right], \tag{2.21}$$

where $\delta(\mathbf{r}_{\alpha,i},\mathbf{r}_{\beta,j})$ is the Kronecker delta, $\delta(\mathbf{r}_{\alpha,i},\mathbf{r}_{\beta,j}) = 1$ if monomers i and j of molecules α and β occupy the same lattice point and zero otherwise. Each configuration is then weighted with a factor

$$P(\{\mathbf{r}_{\alpha,i}\}) \propto \exp(-wE). \tag{2.22}$$

Self-avoiding walks are recovered for $w \to \infty$, while random walks for $w \to 0$.
This model does not present most of the disadvantages of SAWs, since all problems

due to the self-avoidance are mostly eliminated. Moreover, in the DJ model there is a particular value of the repulsion parameter, $w^* \approx 0.5058$, at which the leading corrections to scaling parametrized in Eq. (2.5) by the exponent Δ_1 are absent [78]. Therefore, the universal scaling limit is reached at lower values of L.

2.3.2 Dilute solutions

While for very low polymer concentrations $\Phi_p \to 0$ the system behaves essentially as an "ideal gas" of polymers, repulsive interactions between different molecules obviously influence the thermodynamic properties of the system as soon as Φ_p increases. In this section, deviations of the osmotic coefficient from the ideal behavior will be taken into account by means of the virial expansion defined in Eq. (2.11), which is appropriate for low polymer concentrations. At the same time, since in a dilute solution the volume fraction of polymers satisfy $\Phi_p \lesssim 1$, overlaps among different molecules are essentially rare. Therefore, in a macroscopic description of dilute polymer solutions we still expect in this regime the only relevant scale to be the radius of gyration $\hat{R}_g$. The idea of macroscopic relevant scale will be explained in 2.3.2.2, introducing the polymer structure factor and the **correlation length** ξ. It is important to stress that the quantities that will be introduced in sec. 2.3.2.1, 2.3.2.2 are experimentally measurable. Indeed, the osmotic coefficient is connected to the pressure difference between the solution container and a pure solvent reservoir, kept in contact by a semipermeable membrane. For what concerns the structure factor, it can be obtained by means of neutron scattering experiments [28].

2.3.2.1 The virial expansion

For low enough concentrations, the osmotic coefficient can be reasonably represented by the first terms of the virial expansion defined in Eq. (2.11). The corresponding virial coefficients B_i can be derived from the grand canonical partition function (1.18) of N_p polymers in a volume V [36]. This reads

$$\Xi = \sum_{N_p=0}^{\infty} \frac{z_p^{N_p}}{N_p!} \int D\mathbf{r}_1 ... D\mathbf{r}_{N_p} \exp[-\beta H_{N_p}], \tag{2.23}$$

where z_p is the polymer fugacity (activity), H_{N_p} is the hamiltonian of the system of N_p polymers and the symbol $D\mathbf{r}_\alpha$ represents an integration over the microscopic degrees of freedom of the α-th molecule. We can split the total hamiltonian in a sum of intramolecular and intermolecular contributions

$$H_{N_p} = \sum_{\alpha}^{N_p} H_\alpha^{\text{intra}}(\{\mathbf{r}_{\alpha,i}\}) + \sum_{\alpha<\beta=1}^{N_p} H_{\alpha\beta}^{\text{inter}}(\{\mathbf{r}_{\alpha,i}\}, \{\mathbf{r}_{\beta,j}\}), \tag{2.24}$$

where $H_\alpha^{\text{intra}}(\{\mathbf{r}_{\alpha,i}\})$, $i = 1, ..., L$, contains the intramolecular interactions among the monomers belonging to a single molecule α, and $H_{\alpha\beta}^{\text{inter}}(\{\mathbf{r}_{\alpha,i}\}, \{\mathbf{r}_{\beta,j}\})$, $i, j = 1, ..., L$ is the total interaction between molecules α and β. In the following, we will make use of

the superscript "intra" and "inter" only when needed. Introducing the single-polymer partition function Q_1 and rescaling the activities $\tilde{z}_p$

$$Q_1 = \int D\mathbf{r}_1 \exp[-\beta H_1], \qquad \tilde{z}_p V = z_p Q_1, \tag{2.25}$$

the grand-canonical partition function in Eq. (2.23) becomes (at third order in $\tilde{z}_p$):

$$\Xi = 1 + \tilde{z}_p V + \frac{\tilde{z}_p^2}{2} V^2 \frac{Q_2}{Q_1^2} + \frac{\tilde{z}_p^3}{6} V^3 \frac{Q_3}{Q_1^3} + O(\tilde{z}_p^4). \tag{2.26}$$

In order to specify the position of the i-th polymer, we can pick up the coordinate of one of its monomer $\bar{\mathbf{r}}_i$, $i = 1, ..., N_p$. The choice is arbitrary: the central monomer, the ending one as well as (with some rearrangements) the center of mass of the molecule all give the same results. As we will see in Chaps. 3 and 4, this procedure forms the basis for the definition of coarse-grained models. Thereafter, we can rewrite the generic $O(\tilde{z}_p^K)$ coefficient in Eq. (2.26) as

$$V^K \frac{Q_K}{Q_1^K} = \int d\bar{\mathbf{r}}_1 ... \bar{\mathbf{r}}_K \left\langle \exp\left(-\beta \sum_{\alpha<\beta}^{K} H_{\alpha\beta}^{\text{inter}} \right) \right\rangle \Big|_{\bar{\mathbf{r}}_1 ... \bar{\mathbf{r}}_K}, \tag{2.27}$$

where the average is performed over the intramolecular Boltzmann measure, keeping the positions $\bar{\mathbf{r}}_i$ fixed. In order to derive the first two virial coefficients, we introduce the **total** intermolecular Mayer factor

$$f_{\alpha\beta} = \exp[-\beta H_{\alpha\beta}^{\text{inter}}] - 1. \tag{2.28}$$

The coefficient of the $O(\tilde{z}_p^2)$ term is

$$V^2 \frac{Q_2}{Q_1^2} = \int d\bar{\mathbf{r}}_1 \bar{\mathbf{r}}_2 \left\langle f_{12} + 1 \right\rangle |_{\bar{\mathbf{r}}_1, \bar{\mathbf{r}}_2} = V \int d\bar{\mathbf{r}}_{12} \left\langle f_{12} \right\rangle |_{0, \bar{\mathbf{r}}_{12}} + V^2, \tag{2.29}$$

while at $O(\tilde{z}_p^3)$ we have

$$V^3 \frac{Q_3}{Q_1^3} = \int d\bar{\mathbf{r}}_1 d\bar{\mathbf{r}}_2 d\bar{\mathbf{r}}_3 \left\langle (f_{12} + 1)(f_{13} + 1)(f_{23} + 1) \right\rangle |_{\bar{\mathbf{r}}_1, \bar{\mathbf{r}}_2, \bar{\mathbf{r}}_3}. \tag{2.30}$$

By exploiting translational invariance and the symmetry in the exchange of labels, we can rewrite Eq. (2.30) as

$$V^3 \frac{Q_3}{Q_1^3} = V \int d\bar{\mathbf{r}}_{12} d\bar{\mathbf{r}}_{13} \left\langle (f_{12} f_{13} f_{23}) \right\rangle |_{0, \bar{\mathbf{r}}_{12}, \bar{\mathbf{r}}_{13}} + \tag{2.31}$$

$$+ V \left[3 \int d\bar{\mathbf{r}}_{12} d\bar{\mathbf{r}}_{13} \left\langle (f_{12} f_{23}) \right\rangle |_{0, \bar{\mathbf{r}}_{12} \bar{\mathbf{r}}_{13}} + 3V \int d\bar{\mathbf{r}}_{12} \left\langle f_{12} \right\rangle |_{0, \bar{\mathbf{r}}_{12}} + V^2 \right].$$

Defining the integrals

$$I_2 = \int d\bar{\mathbf{r}}_{12} \left\langle f_{12} \right\rangle |_{0, \bar{\mathbf{r}}_{12}}, \tag{2.32}$$

$$I_3 = \int d\bar{\mathbf{r}}_{12} d\bar{\mathbf{r}}_{13} \left\langle (f_{12} f_{13} f_{23}) \right\rangle |_{0, \bar{\mathbf{r}}_{12}, \bar{\mathbf{r}}_{13}}, \tag{2.33}$$

$$\hat{T}_1 = \int d\bar{\mathbf{r}}_{12} d\bar{\mathbf{r}}_{13} \langle (f_{12} f_{23}) \rangle |_{0,\bar{\mathbf{r}}_{12}\bar{\mathbf{r}}_{13}}, \tag{2.34}$$

and introducing the flexibility term $T_1 = \hat{T}_1 - I_2^2$, which is zero for rigid molecules, the grand canonical partition function becomes

$$\Xi = 1 + V \left[\tilde{z}_p + \frac{\tilde{z}_p^2}{2}(I_2 + V) + \frac{\tilde{z}_p^3}{6}(I_3 + 3(T_1 + I_2^2 + I_2 V) + V^2) \right] + O(\tilde{z}_p^4). \tag{2.35}$$

In view of Eq. (1.19), we can obtain the pressure P as

$$\beta P(\tilde{z}_p) = \frac{1}{V} \ln \Xi = \tilde{z}_p + \frac{\tilde{z}_p^2}{2} I_2 + \frac{\tilde{z}_p^3}{6}(I_3 + 3T_1 + 3I_2^2) + O(\tilde{z}_p^4). \tag{2.36}$$

To obtain Eq. (2.11), we should express $\tilde{z}_p$ in terms of ρ_p: this can be done by using Eq. (1.21), which becomes

$$\rho_p = z_p \frac{\partial \beta P}{\partial z_p} = \tilde{z}_p \frac{\partial \beta P}{\partial \tilde{z}_p}. \tag{2.37}$$

The first two virial coefficient are then

$$B_2 = -\frac{I_2}{2}, \quad B_3 = -\frac{I_3}{3} - T_1. \tag{2.38}$$

By comparing the universal scaling result of Eq. (2.6) for the osmotic coefficient with the virial expansion written as

$$Z(\rho_p) = 1 + \frac{B_2}{\hat{R}_g^3}\left(\rho_p \hat{R}_g^3\right) + \frac{B_3}{\hat{R}_g^6}\left(\rho_p^2 \hat{R}_g^6\right) + ..., \tag{2.39}$$

we obtain an important information concerning the **universality of the adimensional ratios**

$$\frac{B_{i+1}}{\hat{R}_g^{3i}} \underset{L\to\infty}{\longrightarrow} A_{i+1}^* \tag{2.40}$$

in the scaling limit. The quantities A_{i+1}^* are **independent on the microscopic detail** for a large class of models, as soon as we have the same polymer architecture. The correctness of renormalization-group predictions for polymers was indeed initially tested by computing these quantities by means of different microscopic models and comparing the results.

2.3.2.2 Structure factor and correlation length

The concepts of particle densities and distribution functions introduced in Sec. 1.2 for atomic fluids can be easily generalized to the case of polymers. The pair distribution function is now defined in terms of the monomer coordinates and reads

$$g(|\mathbf{r}_1 - \mathbf{r}_1|) = \frac{1}{L^2 \rho_p^2} \left\langle \sum_{\alpha,\beta=1}^{N_p}{}' \sum_{i,j=1}^{L} \delta(\mathbf{r}_1 - \mathbf{r}_{\alpha,i}) \delta(\mathbf{r}_2 - \mathbf{r}_{\beta,j}) \right\rangle. \tag{2.41}$$

The primed sum indicates that the term with $\alpha = \beta$ must be omitted. Analogously, we define the polymer structure factor

$$S(\mathbf{q}) = \frac{1}{L^2 N_p} \left\langle \sum_{\alpha,\beta=1}^{N_p} \sum_{i,j=1}^{L} e^{i\mathbf{q}\cdot(\mathbf{r}_{\alpha,i}-\mathbf{r}_{\beta,j})} \right\rangle. \tag{2.42}$$

In contrast with Eq. (2.41), the sum in Eq. (2.42) is performed also on the diagonal terms with $\alpha = \beta$, which take into account the intramolecular correlations. These terms define the **form factor**

$$F(\mathbf{q}) = \frac{1}{L^2 N_p} \left\langle \sum_{\alpha=1}^{N_p} \sum_{i,j=1}^{L} e^{i\mathbf{q}\cdot(\mathbf{r}_{\alpha,i}-\mathbf{r}_{\alpha,j})} \right\rangle. \tag{2.43}$$

Therefore, the structure factor is connected to the pair distribution function by

$$S(\mathbf{q}) = N_p \delta(\mathbf{q}) + F(\mathbf{q}) + \rho_p \int d\mathbf{r}(g(r) - 1) e^{i\mathbf{q}\cdot\mathbf{r}}. \tag{2.44}$$

Since $F(0) = 1$, $S(q \to 0)$ in the grand canonical ensemble is connected to the average fluctuations in the number of polymers, and Eq. (1.32) still holds. In the absence of long-range correlations, it is possible to expand $S(\mathbf{q})$ around $S(0)$ in the so-called Ornstein-Zernike approximation, obtaining

$$S(\mathbf{q}) = \frac{S(0)}{1 + q^2\xi^2}, \tag{2.45}$$

where ξ is the **correlation** length of the system. It must be emphasized that Eq. (2.45) is valid only in the limit $q\xi \ll 1$, that is for $r \gg \xi$. From Eq. (2.42) we see that $S(q)$ is proportional to the Fourier transform of the **total** correlation function among monomers [27]. From the inverse Fourier transform of Eq. (2.45), we obtain that the total correlation function $h(r)$ at large distances $r \gg \xi$ (in three dimensions) behaves as

$$h(r) \approx \frac{1}{r} \exp(-r/\xi). \tag{2.46}$$

Therefore, ξ is measure of the distance at which microscopic components are correlated: for $r \gg \xi$ density fluctuations become almost statistically independent.
In the case of a single polymer (a dilute solution in the limit of zero concentration), the correlation length is of the order of the radius of gyration of the molecule [24, 27]

$$\xi \sim \hat{R}_g, \tag{2.47}$$

thus confirming that $\hat{R}_g$ is the only relevant scale in a macroscopic description of polymers. If the density increases, the correlation length is reduced by the interactions among different molecules. However, as soon as overlaps are rare and $\Phi_p \lesssim 1$, we still expect that the degree of correlation between monomers extends up to distances of the order of the radius of gyration. This property obviously breaks down in semidilute solutions, where many different molecules strongly overlap. In this regime, a single-polymer scale like the zero-density radius of gyration is not representative of the behavior of many interpenetrating molecules. A phenomenological description of the properties of semidilute solutions based on scaling theories and concentration blobs will be presented in the following section.

2.3.3 Semidilute solutions

The different regimes introduced in Sec. 2.2 are shown in Fig. 2.4. In dilute solutions different polymer coils are far apart, and start to overlap at a volume fraction $\Phi_p \approx 1$. If we increase the concentration, different coils interpenetrate so much that the individuality of each molecule is lost, and we enter the semidilute regime. We already mentioned the fact that in semidilute solutions the overall monomer density is small $\rho_m = \rho_p L \ll 1$, otherwise the concentrated limit is reached, where we have the screening of excluded-volume interactions.

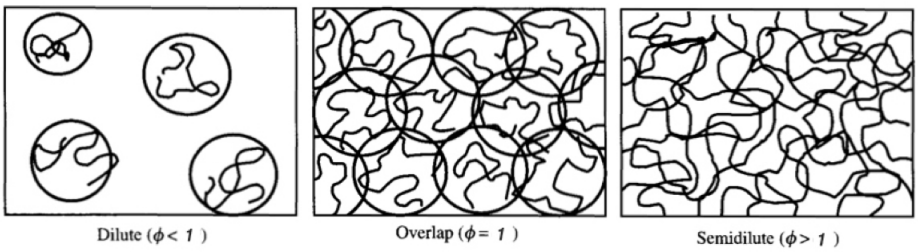

Figure 2.4. Concentration effects in polymer solutions [28]. Left: dilute regime. Center: solutions at overlap. Right: semidilute solutions.

These considerations lead to the blob representation of polymers and to phenomenological descriptions which are able to capture the behavior of the system in the semidilute regime [24, 28]. The simplest way of obtaining the semidilute thermodynamic properties of polymers is based on scaling theory. The key assumption of the approach is that for high overlapping polymers everything should be independent on the degree of polymerization L, and depend only on the monomer concentration ρ_m. In other words, for $L \to \infty$ nothing should change if we replace our system of N_p polymers of length L with a system of kN_p polymers of length L/k, as long as $L/k \gg 1$ and the radius of gyration of polymers of length L/k is significantly larger than the correlation length.
From Eq. (2.6), the L-dependence of the osmotic pressure in the scaling limit and for large volume fractions can be written as [24, 31]

$$\beta P \sim \rho_p f_Z(\Phi_p) \sim \frac{\rho_m}{L} f_Z(\rho_m L^{(3\nu-1)}), \quad \Phi_p \gg 1. \tag{2.48}$$

In order to become independent of L for $\Phi_p \to \infty$, $f_Z(\Phi_p)$ must behave as

$$f_Z(\Phi_p) \sim \Phi_p^m. \tag{2.49}$$

The exponent m is fixed by requiring the independence of Eq. (2.48) from L, at a fixed ρ_m:

$$m(3\nu - 1) - 1 = 0 \longrightarrow m = \frac{1}{3\nu - 1}. \tag{2.50}$$

Thus

$$Z(\Phi_p) \sim \Phi_p^{1/(3\nu-1)}, \quad \Phi_p \gg 1 \tag{2.51}$$

is the scaling prediction for the osmotic coefficient in the semidilute regime.
For what concerns the correlation length ξ, we saw in Sec. 2.3.2.2 that in the limit

of infinite dilution it is of the order of the radius of gyration $\hat{R}_{g,0}$. The subscript 0 means that we are referring to the zero-density radius of gyration, since concentration effects will influence the average size of a molecule. At higher volume fractions we expect the correlation length to decrease, since the screening effects connected to the interpenetration of different polymer coils come into play.
To determine the Φ_p dependence of $\xi(\Phi_p)$ we start from simple dimensional analysis

$$\xi(\Phi_p) \sim \hat{R}_{g,0} f_\xi(\Phi_p), \quad \Phi_p \gg 1. \tag{2.52}$$

Using $\hat{R}_{g,0} \sim L^\nu$ and requiring the r.h.s. to be L-independent at a fixed ρ_m, we obtain the power law

$$\frac{\xi(\Phi_p)}{\hat{R}_{g,0}} \sim \Phi_p^{-\nu/(3\nu-1)}, \tag{2.53}$$

which is indeed a decreasing function of Φ_p. It is important to underline that all these results are valid **irrespective of the polymer architecture**.
Eqs. (2.51), (2.53) and other properties can be equivalently obtained in the representation of polymers by means of **correlation blobs**. This approach, although qualitative, is able to capture the correct scaling behavior of the system. It is based on the assumption that semidilute solutions are in a bridging regime between dilute and concentrated, and their properties depend on the scale at which the system is observed [28, 31].

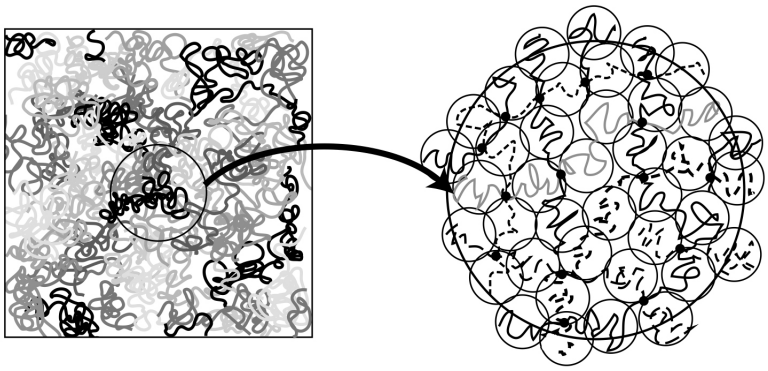

Figure 2.5. Magnification of a portion of a semidilute solution, and partitioning in terms of concentration blobs [27].

If we look at a semidilute polymer solution from large distances, see Fig. 2.5, the system appears as completely molten. However, if we magnify a portion of it, we see that different molecules are meshed only up to an average distance $r_{g,b}$. Inside a sphere of radius $r_{g,b}$, a section of each molecule still preserves its identity and does not overlap with other molecules. The idea is now to partition each molecule in n_b subunits or "blobs" of radius $r_{g,b}$, each containing $g_b = L_b/n_b$ monomers. This construction builds-up the **blob representation** of a polymer. Clearly, we expect that if the density increases the size of a single blob $r_{g,b}$ shrinks since molecules overlap more. To compute the density dependence of $r_{g,b}$ we introduce several assumptions:

- The blobs completely fill the volume of the solution, without voids. Therefore, the overall monomer density ρ_m is equal to the monomer density in a blob

$$\rho_m = \rho_p L \sim \frac{g_b}{r_{g,b}^3}. \tag{2.54}$$

- Since different blobs do not interact, the g_b subunits are connected to the radius $r_{g,b}$ of the blob by the excluded-volume relation

$$r_{g,b} \sim {g_b}^{\nu}. \tag{2.55}$$

By combining Eqs. (2.54) and (2.55), we obtain

$$r_{g,b}^{(3-1/\nu)} \sim \frac{1}{\rho_p L} \sim \frac{\hat{R}_{g,0}^{(3-1/\nu)}}{\Phi_p}. \tag{2.56}$$

It follows

$$r_{g,b} \sim \hat{R}_{g,0} \Phi_p^{-\nu/(3\nu-1)}. \tag{2.57}$$

From Eq. (2.57) we see that $r_{g,b} \sim \hat{R}_{g,0}$ for solutions at overlap $\Phi_p \approx 1$, and is independent of L. Moreover, by comparing Eq. (2.57) with Eq. (2.53) we see that the radius $r_{g,b}$ is nothing but the correlation length ξ. We are thus led to a direct physical interpretation of the correlation blobs, which relies on a separation of scales exhibited by polymers in semidilute solutions: inside each correlation blob and at scales $r \lesssim \xi$, monomers have correlations of excluded-volume type and the sub-coils are therefore swollen. At scales larger than the correlation length, each blob behaves almost as a statistical independent unit (monomers belonging to two different blobs are uncorrelated). A semidilute polymer solution can thus be seen as a concentrated system of correlation blobs, allowing us to compute several interesting quantities. For a linear chain, the concentration dependence of the radius of gyration $\hat{R}_g(\Phi_p)$ can be obtained by considering each molecule as a random walk of $L/g_b = n_b$ correlation blobs of size $r_{g,b}$. From Eqs. (2.55) and (2.57) we can estimate

$$n_b \sim \Phi_p^{1/(3\nu-1)}. \tag{2.58}$$

The radius of gyration $\hat{R}_g(\Phi_p)$ then becomes

$$\hat{R}_g^2(\Phi_p) = n_b r_{g,b}^2 \quad \longrightarrow \quad \frac{\hat{R}_g(\Phi_p)}{\hat{R}_{g,0}} \sim \Phi_p^{(1-2\nu)/(3\nu-1)}. \tag{2.59}$$

The semidilute behavior of osmotic coefficient $Z(\Phi_p)$ (2.51) can also be obtained in the framework of the blob representation, by using the fact that correlation blobs of radius $r_{g,b}$ (or equivalently ξ) behave as statistically independent units. Assuming the system to be an ideal gas of blobs, we can give an estimate of the osmotic pressure βP as the number of independent units (blobs) per unit volume

$$\beta P \sim \frac{N_{\text{blobs}}}{V} \sim \frac{1}{\xi^3}. \tag{2.60}$$

By using Eq. (2.57) and $\Phi_p \sim \rho_p L^{3\nu}$, we have again

$$\frac{\beta P}{\rho_p} = Z(\Phi_p) \sim \Phi_p^{1/(3\nu-1)}. \tag{2.61}$$

Therefore scaling theories and blob-model predictions are completely consistent. In conclusion, it is important to stress that, albeit qualitative, concentration-blob models are the pathway to the definition of accurate multiblob coarse-grained models of polymers, as we will introduce in Chap. 3 and apply to the case of star polymers in Chap. 5.

Chapter 3

Coarse-grained models for polymers

The thermodynamic behavior of polymer systems for low densities can be reasonably obtained by using the first few terms of the virial expansion defined in Eq. (2.11), once the virial coefficients B_i are known. They can be computed, for example, by means of numerical simulations of a limited number of molecules [37] (although each of them should have a very large degree of polymerization L in order to reach the scaling limit). Increasing the polymer density from the dilute to the semidilute regime, the description of the thermodynamic properties of polymer solutions in terms of a truly microscopic model becomes rapidly unfeasible even numerically, due to the large number of degrees of freedom involved. Indeed, we already mentioned how a genuine semidilute solution is characterized by a large polymer volume fraction Φ_p but an overall small monomer density ρ_m, otherwise one enters the concentrated regime. In terms of the degree of polymerization L, it is easy to show that ρ_m scales as [24, 28]

$$\rho_m \sim \Phi_p L^{(1-3\nu)}; \tag{3.1}$$

hence, if one wants $\Phi_p > 1$ and $\rho_m \ll 1$ at the same time, the degree of polymerization L must be consistently increased. This implies that the numerical simulations of these systems, even using simple lattice models as those described in Sec. 2.3.1, become more and more computationally demanding. Therefore, it is useful to develop a simplified description of the system which does not include too many details at the microscopic atomic scale. In these models, which gained attention in the last decades and are commonly referred to as **coarse-grained** (CG) models, most of the microscopic degrees of freedom are integrated out and each molecule is replaced by a set of $n \ll L$ effective interaction sites. One must then introduce appropriate interactions among these effective units in order to reproduce the correct mesoscopic and macroscopic behavior of the underlying microscopic system. Several methods have been proposed in the literature to parametrize and determine these interactions, such as energy-based methods, force-matching methods and relative-entropy methods [42–45]. In this thesis we will rely on structure-matching methods [46], which aim at reproducing at the CG level the mesoscopic structure of the full-monomer (FM) system. These coarse-graining strategies can be conceptually related with the real-space spin-blocking technique developed by Kadanoff in his pioneering works [38]

which led to the renormalization-group analysis of ferromagnetism [39–41].
Depending on the number of interaction sites, one obtains different coarse-grained models. If every molecule is mapped onto a point-like particle, thus retaining only three translational degrees of freedom for each polymer, one speaks of single-site or "single-blob" (SB) representations. As we will discuss, in the single-site description of linear chains and star polymers, most of the literature [65–69, 72, 75, 76] considered the central monomer or the center of mass of each molecule as the effective coordinate associated with the CG molecule. Moreover, the pairwise-additive approximation was used for the total intermolecular interaction. The effective pair potential between two polymers is obtained in the zero-density limit (two molecules). This choice is obviously computationally very efficient because of the huge decimation of degrees of freedom, which allows one to rapidly obtain results by means of numerical simulations or by using integral equation methods. However, the predictability of these models is limited to the dilute regime, where multiple overlaps among different molecules are rare. Indeed, it is well known that in an exact coarse-graining procedure the effective interaction has contributions beyond two-body terms. Three,..., N_p-body potentials appear [32], which are relevant when three (or more) molecules overlap. Several techniques have been proposed in the literature [70–74] to extend these models at higher densities, with the drawback of complicating the analysis and sometimes introducing some thermodynamic inconsistencies. In addition to this, single-blob models present problems connected to the choice of the representation: different effective interaction sites leads to quite different results for the thermodynamic behavior of the system.
In order to obtain a reliable description of the semidilute regime, a possible strategy consists in switching to a lower level of coarse-graining, thus introducing multi-site or multiblob (MB) models. Here, every polymer is mapped onto a soft n-atomic molecule, and interactions are parametrized in terms of intramolecular and intermolecular potentials, that reproduce the underlying polymer structure. Again, these interactions are computed in the zero-density limit (one or two polymers). With this choice, many-body intermolecular interactions should be better described, and therefore the model should be reliable at densities at which multiple overlaps occur. Moreover, a residual flexibility of the molecule is retained with respect to the single-blob case.
In this chapter, we introduce the general formalism underlying every structure-based coarse-graining strategy, both in the single- and multiblob representations, underlining drawbacks and advantages of each approach.

3.1 Single-blob models

We consider a system of N_p macromolecules in a volume V, where each molecule is composed by L microscopic units. In the single-blob approach, the microscopic degrees of freedom of each molecule are integrated out and only three translational degrees of freedom are retained [46, 47]. Intermolecular interactions are then parametrized by means of effective potentials among these effective coordinates. In order to obtain the CG representation of the system, one has to define the effective coordinates $\mathbf{R}_\alpha$ in terms of the microscopic coordinates $\{\mathbf{r}_{\alpha,i}\}$, $\alpha = 1, ..., N_p$,

$i = 1, ..., L$, via the linear transformation

$$\mathbf{R}_\alpha = \mathbf{T}[\{\mathbf{r}_{\alpha,i}\}] = \sum_{i=1}^{L} c_i \mathbf{r}_{\alpha,i}, \tag{3.2}$$

where the coefficients c_i satisfy the normalization condition $\sum_{i=1}^{L} c_i = 1$. Different choices of the coefficients c_i correspond to different single-blob representations: in the case of polymer chains, $c_i = \delta_{i,1}$ (equivalently $c_i = \delta_{i,L}$) identifies the end-monomer representation, $c_i = \delta_{i,L/2}$ the central monomer representation, and $c_i = 1/L$, $i = 1, \ldots, L$ the center of mass representation.
Although the original problem was characterized by pairwise additive interactions, in an **exact** mapping the total intermolecular interaction potential $V(\{\mathbf{R}_\alpha\})$ among the effective coordinates is the sum of $2, ..., N_p$-body interaction terms [32, 46, 47]:

$$V(\{\mathbf{R}_\alpha\}) = V^{(0)}(N, V) + V^{(2)}(\{\mathbf{R}_\alpha\}) + V^{(3)}(\{\mathbf{R}_\alpha\}) + \ldots. \tag{3.3}$$

The zero-body term $V^{(0)}(N, V)$ is related to the free energy of an isolated molecule and does not depend on the effective coordinates, $V^{(0)}(N, V) = N v_0$. The single-molecule potentials $V^{(1)}(\{\mathbf{R}_\alpha\})$ vanish instead as a consequence of the translational symmetry of the original problem. The generic term $V^{(n)}(\{\mathbf{R}_\alpha\})$ indicates genuine n-body contributions of the form

$$V^{(n)}(\{\mathbf{R}_\alpha\}) = \sum_{\alpha_1 < \alpha_2 < \ldots < \alpha_n}^{N_p} u^{(n)}(\mathbf{R}_{\alpha_1}, \mathbf{R}_{\alpha_2}, \ldots, \mathbf{R}_{\alpha_n}). \tag{3.4}$$

Each potential $u^{(n)}(\mathbf{R}_{\alpha_1}, \mathbf{R}_{\alpha_2} \ldots, \mathbf{R}_{\alpha_n})$ in Eq. (3.4) is inherently n-body, and cannot be decomposed a a sum of lowest order interactions: for example, the potential $u^{(3)}(\mathbf{R}_{\alpha_1}, \mathbf{R}_{\alpha_2}, \mathbf{R}_{\alpha_3})$ cannot be decomposed as a sum of the $u^{(2)}(\mathbf{R}_{\alpha_i}, \mathbf{R}_{\alpha_j})$ pair potentials.
These effective interactions can be computed in the grand canonical ensemble. For a system of N_p molecules, each composed by L atoms, the partition function Ξ defined in Eq. (2.23) can be written as

$$\Xi = 1 + \tilde{z}_p V + \frac{\tilde{z}_p^2}{2} V^2 \frac{Q_2}{Q_1^2} + \frac{\tilde{z}_p^3}{6} V^3 \frac{Q_3}{Q_1^3} + ..., \tag{3.5}$$

as shown in Sec. 2.3.2.1. The coefficient of the $O(\tilde{z}_p^2)$ term is

$$V^2 \frac{Q_2}{Q_1^2} = V^2 \frac{\int D\mathbf{r}_1 D\mathbf{r}_2 \exp[-\beta(H_1 + H_2 + H_{12}^{\text{inter}})]}{\int D\mathbf{r}_1 D\mathbf{r}_2 \exp[-\beta(H_1 + H_2)]}. \tag{3.6}$$

If we now insert the factor

$$1 = \int d\mathbf{R}_1 \delta\left(\mathbf{R}_1 - \mathbf{T}[\{\mathbf{r}_{1,i}\}]\right) \int d\mathbf{R}_2 \delta\left(\mathbf{R}_2 - \mathbf{T}[\{\mathbf{r}_{2,j}\}]\right), \tag{3.7}$$

in both the numerator and the denominator of Eq. (3.6), we can rewrite it as

$$V^2 \frac{Q_2}{Q_1^2} = \int d\mathbf{R}_1 d\mathbf{R}_2 \mathcal{G}^{(2)}(\mathbf{R}_1, \mathbf{R}_2), \tag{3.8}$$

where we introduced the second-order distribution function

$$\mathcal{G}^{(2)}(\mathbf{R}_1,\mathbf{R}_2) = \langle \exp[-\beta H_{12}^{\text{inter}}]\rangle_{\mathbf{R}_1,\mathbf{R}_2} = \tag{3.9}$$

$$= \frac{\int D\mathbf{r}_1 D\mathbf{r}_2 e^{-\beta(H_1+H_2+H_{12}^{\text{inter}})}\delta\left(\mathbf{R}_1-\mathbf{T}[\{\mathbf{r}_{1,i}\}]\right)\delta\left(\mathbf{R}_2-\mathbf{T}[\{\mathbf{r}_{2,j}\}]\right)}{\int D\mathbf{r}_1 D\mathbf{r}_2 \exp[-\beta(H_1+H_2)]\delta\left(\mathbf{R}_1-\mathbf{T}[\{\mathbf{r}_{1,i}\}]\right)\delta\left(\mathbf{R}_2-\mathbf{T}[\{\mathbf{r}_{2,j}\}]\right)}.$$

The distribution function $\mathcal{G}^{(2)}(\mathbf{R}_1,\mathbf{R}_2)$ is therefore the microscopic average of the total intermolecular Boltzmann factor $\exp[-\beta H_{12}^{\text{inter}}]$ over the noninteracting Boltzmann measure, keeping the effective coordinates $\mathbf{R}_1,\mathbf{R}_2$ fixed. From Eq. (3.8), the pair potential among the two CG molecules is defined by the relation

$$\beta u^{(2)}(\mathbf{R}_1,\mathbf{R}_2) = -\ln[\mathcal{G}^{(2)}(\mathbf{R}_1,\mathbf{R}_2)] = -\ln\langle \exp[-\beta H_{12}^{\text{inter}}]\rangle_{\mathbf{R}_1,\mathbf{R}_2} \tag{3.10}$$

and is a function of $R_{12} = |\mathbf{R}_1-\mathbf{R}_2|$ due to the translational and rotational invariance of the original problem. Moreover, Eq. (3.10) shows that the pair potential is a **potential of mean force**.
We now consider higher-order terms in Eq. (3.5). The $O(\tilde{z}_p^3)$ coefficient is given by

$$V^3\frac{\int D\mathbf{r}_1 D\mathbf{r}_2 D\mathbf{r}_3 \exp[-\beta(H_1+H_2+H_3+H_{12}^{\text{inter}}+H_{13}^{\text{inter}}+H_{23}^{\text{inter}})]}{\int D\mathbf{r}_1 D\mathbf{r}_2 D\mathbf{r}_3 \exp[-\beta(H_1+H_2+H_3)]}. \tag{3.11}$$

The introduction of a set of δ-functions analogous to that performed in Eq. (3.7) allows us to rewrite it as

$$\int d\mathbf{R}_1 d\mathbf{R}_2 d\mathbf{R}_3 \mathcal{G}^{(3)}(\mathbf{R}_1,\mathbf{R}_2,\mathbf{R}_3), \tag{3.12}$$

where $\mathcal{G}^{(3)}(\mathbf{R}_1,\mathbf{R}_2,\mathbf{R}_3)$ is the third-order correlation function

$$\mathcal{G}^{(3)}(\mathbf{R}_1,\mathbf{R}_2,\mathbf{R}_3) = \langle \exp[-\beta(H_{12}^{\text{inter}}+H_{13}^{\text{inter}}+H_{23}^{\text{inter}})]\rangle_{\mathbf{R}_1,\mathbf{R}_2,\mathbf{R}_3}. \tag{3.13}$$

More generally, we can define a hierarchy of n-order correlation functions as

$$\mathcal{G}^{(n)}(\mathbf{R}_1,...,\mathbf{R}_n) = \left\langle \exp\left[-\beta\left(\sum_{i<j=1}^{n} H_{ij}^{\text{inter}}\right)\right]\right\rangle_{\mathbf{R}_1,...,\mathbf{R}_n} =$$

$$= \frac{\int\left(\prod_{\alpha=1}^n D\mathbf{r}_\alpha e^{-\beta H_\alpha^{\text{intra}}}\right)\exp\left[-\beta\left(\sum_{i<j=1}^n H_{ij}^{\text{inter}}\right)\right]\prod_{\alpha=1}^n\delta\left(\mathbf{R}_\alpha-\mathbf{T}[\{\mathbf{r}_{\alpha,i}\}]\right)}{\int\left(\prod_{\alpha=1}^n D\mathbf{r}_\alpha e^{-\beta H_\alpha^{\text{intra}}}\right)\prod_{\alpha=1}^n\delta\left(\mathbf{R}_\alpha-\mathbf{T}[\{\mathbf{r}_{\alpha,i}\}]\right)}, \tag{3.14}$$

In terms of the $\mathcal{G}^{(n)}(\mathbf{R}_1,...,\mathbf{R}_n)$, the genuine n-body potential $u^{(n)}$ is defined as

$$\begin{aligned}\beta u^{(n)}(\mathbf{R}_1,\mathbf{R}_2,\ldots,\mathbf{R}_n) &= -\ln\mathcal{G}^{(n)}(\mathbf{R}_1,...,\mathbf{R}_n) - \sum^{(2,n)}\beta u^{(2)}(\mathbf{R}_{\alpha_i},\mathbf{R}_{\alpha_j}) \\ &- \sum^{(3,n)}\beta u^{(3)}(\mathbf{R}_{\alpha_i},\mathbf{R}_{\alpha_j},\mathbf{R}_{\alpha_k}) \\ &- \sum^{(n-1,n)}\beta u^{(n-1)}(\mathbf{R}_{\alpha_i},\mathbf{R}_{\alpha_j},\ldots,\mathbf{R}_{\alpha_{n-1}}),\end{aligned} \tag{3.15}$$

where the symbol $\sum^{(m,n)}$ indicates a summation over the ordered m-ples of n objects. From Eq. (3.15), for example, the three-body potential is obtained as

$$\begin{aligned}\beta u(\mathbf{R}_1,\mathbf{R}_2,\mathbf{R}_3) &= -\ln \mathcal{G}^{(3)}(\mathbf{R}_1,\mathbf{R}_2,\mathbf{R}_3) - \beta u^{(2)}(\mathbf{R}_{12}) - \beta u^{(2)}(\mathbf{R}_{13}) - \beta u^{(2)}(\mathbf{R}_{23}) \\ &= -\ln\left[\frac{\mathcal{G}^{(3)}(\mathbf{R}_1,\mathbf{R}_2,\mathbf{R}_3)}{\mathcal{G}^{(2)}(R_{12})\mathcal{G}^{(2)}(R_{13})\mathcal{G}^{(2)}(R_{23})}\right]. \end{aligned} \tag{3.16}$$

These results show that while on one hand the coarse-graining strategy simplifies the description, by integrating out most of the internal degrees of freedom, on the other hand it introduces very complex interactions among the effective sites.
Due to the strong relation between structural properties and thermodynamics in the zero-density limit (see Sec. 2.3.2.1), the latter can be related to the effective interactions. For example, it is possible to relate the virial coefficients B_i to the effective potentials $u^{(i)}$[48]. The first two virial coefficients read

$$B_2 = -\frac{1}{2}\int d\mathbf{r}\left(e^{-\beta u^{(2)}(r)} - 1\right), \tag{3.17}$$

and

$$\begin{aligned} B_3 = &- \frac{1}{3}\int d\mathbf{r}_{12}d\mathbf{r}_{13}\left(e^{-\beta u^{(3)}(\mathbf{r}_{12},\mathbf{r}_{13},\mathbf{r}_{23})} - 1\right) e^{-\beta[u^{(2)}(r_{12})+u^{(2)}(r_{13})+u^{(2)}(r_{23})]} \\ &- \frac{1}{3}\int d\mathbf{r}_{12}d\mathbf{r}_{13}\left(e^{-\beta u^{(2)}(r_{12})} - 1\right)\left(e^{-\beta u^{(2)}(r_{13})} - 1\right)\left(e^{-\beta u^{(2)}(r_{23})} - 1\right). \end{aligned} \tag{3.18}$$

The general virial coefficient B_n takes contributions from all the i-body potential $u^{(i)}$ up to $i = n$.
From this discussion, we see that an exact coarse-graining mapping is an extremely sophisticated task. The complexity of determining the n-body interaction $u^{(n)}(\mathbf{R}_1,\mathbf{R}_2\ldots\mathbf{R}_n)$ by means of numerical simulations grows obviously with n: for $n \geq 3$ one should sample a function of $3(n-2)$ variables, due to translational and rotational invariance, which becomes rapidly unfeasible. Moreover, even if exact parametrizations of the CG potentials were known, the computational cost of a simulation which includes up to n-body interactions would grow as N_p^n. Hence, approximations must be introduced.
One common choice is to truncate the series of Eq. (3.3) by considering $V^{(n)}(\{\mathbf{R}_\alpha\}) = 0$ for $n \geq 3$, thus retaining only pair interactions. This is the aforementioned pairwise-additive approximation, in which the total interaction for a system of N_p coarse-grained molecules becomes

$$V(\mathbf{R}_1,\ldots,\mathbf{R}_{N_p}) = \sum_{\alpha<\gamma=1}^{N_p} u^{(2)}(|\mathbf{R}_\alpha - \mathbf{R}_\gamma|). \tag{3.19}$$

The pair potential $u^{(2)}(|\mathbf{R}_1 - \mathbf{R}_2|)$ can be obtain by means of Eq. (3.10), that is by a numerical simulation of two noninteracting molecules (zero-density limit). Since the model has no implicit state-dependence, thermodynamic and structural properties of the system can be investigated by means of standard statistical mechanics methods

for monoatomic fluids, such as Monte Carlo simulations or integral equations.
The pairwise-additive approximation is valid as long as the contributions due to the many-body interactions $u^{(n)}$ with $n \geq 3$ are negligible, which means that multiple overlaps among three (or more) molecules must not occur. Hence, we expect single-blob models with pairwise-additive potentials to be reliable in the dilute regime only. Indeed, if we set $u^{(3)} = 0$ in Eqs. (3.17) and (3.18), the CG model only reproduces the second virial coefficient B_2. In general, any arbitrary truncation of the many-body series introduces a lack of consistency between the original model and the coarse-grained one.
At the same time, the relation between structural properties and thermodynamics in the zero-density limit allows us to use the virial coefficients B_i as valuable tools for testing zero-density coarse-grained models. For instance, to investigate the thermodynamic behavior of SB models that only differ by the choice of the effective interaction site, one can use the third virial coefficient B_3.
The previous discussion is completely general and can be applied to dilute and semidilute polymer solutions in good solvents. We will consider effective microscopic models in an implicit solvent such as those introduced in Sec. 2.3.1: roughly speaking, this means that a coarse-graining of the solvent molecules has already been performed, and the average presence of the solvent has been taken into account by means of a local monomer-monomer repulsion. As we discussed, these models are able to capture the correct long-wavelength behavior in the scaling limit. In order to define single-blob models for polymers, one then integrates out the monomer degrees of freedom and introduces a set of effective sites $\mathbf{R}_\alpha$, $\alpha = 1, \ldots, N_p$, interacting by means of appropriate potentials. Once again, universality in the scaling limit $L \to \infty$ significantly constraints the effective interactions. For finite values of L, the adimensional distributions $\mathcal{G}^{(n)}$ in Eq. (3.14) depend on the specific polymer under consideration, i.e. are model-dependent functions. However, in the scaling limit $L \to \infty$, they converge to universal distributions

$$\lim_{L\to\infty} \mathcal{G}^{(n)}(\mathbf{R}_1, ..., \mathbf{R}_n) = \bar{\mathcal{G}}^{(n)}(\mathbf{b}_1, ..., \mathbf{b}_n), \tag{3.20}$$

where we define $\mathbf{b}_\alpha = \mathbf{R}_\alpha / \hat{R}_g$, and $\hat{R}_g$ is the zero-density average radius of gyration. These universal distributions only depend on the polymer architecture, on the quality of solvent, but do not depend on the microscopic model.
As a consequence, also the generic n-body effective potentials $\beta u^{(n)}$ in Eq. (3.15) converges, in the scaling limit, to a universal function $\beta u^{(n)}$

$$\beta u^{(n)}(\mathbf{R}_1, \ldots \mathbf{R}_n) \underset{L\to\infty}{\longrightarrow} \beta \bar{u}^{(n)}(\mathbf{b}_1, ..., \mathbf{b}_n), \tag{3.21}$$

as soon as distances are expressed in terms of the zero-density radius of gyration $\hat{R}_g$. The specific discussion of these potentials in the case of linear chains and star polymers is postponed to later chapters.
As for the general case, the most common choice in polymer physics is to truncate the series of Eq. (3.3) at the two-body level, considering only the potential $\beta \bar{u}^{(2)}(\mathbf{b}_1, \mathbf{b}_2)$ defined in Eq. (3.10). Again, we expect this to be reliable as soon as no multiple overlaps occur, thus in the dilute regime $\Phi_p \lesssim 1$, where many-body intermolecular interactions can be neglected.

3.1.1 State-dependent interactions

Now the question becomes how to build coarse-grained models which are truly representative of the original system at higher densities, by preserving the single-blob representation. In principle, this can be obtained in two ways. First, one could progressively reintroduce n-body interactions among the CG molecules, thus relaxing the pairwise-additive approximation. As explained, this becomes a very complex task for increasing n.
Another possibility to widen the density range in which single-site models with pairwise effective interactions can be used is based on the introduction of potentials which explicitly depend on the thermodynamic state of the system. These state-dependent interactions are obtained as follows: one fixes the state of the system S (such as the polymer density ρ_p, or the chemical potential μ_p) and determines, at a full-monomer level, some target, reference thermodynamic properties. The pair interaction potential among the CG molecules $u^{(2)}(r;S)$, which is now function of the state S, is then determined by requiring the coarse-grained model to correctly reproduce the target properties chosen, *at the same thermodynamic point* S.
Structurally derived state-dependent potentials have been mostly discussed in the context of the canonical ensemble [70–74], hence all thermodynamic and structural quantities depend on the density[1] ρ_p. In this approach the pair potential $u^{(2)}(r;\rho_p)$ is obtained by requiring the CG model to reproduce the two-point correlation function $\mathcal{G}^{(2)}(r,\rho_p)$ defined in Eq. (3.10), at the given value of the density. The uniqueness of such a potential is guaranteed by Henderson's theorem [50]. Of course, for $\rho_p \to 0$ the potential $u^{(2)}(r;\rho_p)$ converges to the potential of mean force $u^{(2)}(r)$ considered before. The inversion of $\mathcal{G}^{(2)}(r,\rho_p)$ to extract $u^{(2)}(r;\rho_p)$ can be performed by means of iterative procedures. For instance, one could use the iterative Boltzmann inversion method [49]. For soft potentials, the hypernetted-chain inversion scheme [71, 72] is also particularly convenient. Although use of $u^{(2)}(r;\rho_p)$ allows one to reproduce the pair distribution function for any value of the density, there is no warranty that any other structural property of the underlying system—for instance, the three-body correlation function—is reproduced correctly. Moreover, state-dependent interactions introduce some inconsistencies in the calculation of standard thermodynamic properties [51, 52]. For instance, in systems with state-independent potentials there are two equivalent routes to the pressure. One can define it mechanically (virial pressure), as the force per unit area acting on the boundaries, or thermodynamically, as the derivative of the free energy with respect to density. In the presence of state-dependent interactions the two definitions are no longer equivalent [51, 52]. Moreover, in the case of density-dependent potentials none of them reproduces the correct pressure of the underlying system, although, at least in the low-density limit, the virial expression is closer to the correct pressure than the thermodynamic one [52]. Another problem of the approach is that effective state-dependent potentials depend on the ensemble in which they have been derived [52]: the equivalence of the ensembles breaks down. Therefore, different thermodynamic results are obtained by using coarse-grained models defined at the same state point of the underlying system but in different ensembles, making the computation of phase transitions and

[1] In principle, one should also consider the temperature, but such a variable does not play any role in the present discussion, hence it will never be explicitly reported.

transition lines quite challenging. As a general message, care is needed when using state-dependent interactions to derive the thermodynamics of the original system and to compute free energies. In particular, one should be careful to employ state-dependent potentials only in the statistical ensemble in which they have been derived.

3.2 Multiblob models

As discussed in Sec. 3.1, the main problem of single-blob models is the appearance of many-body intermolecular interaction terms of increasing complexity among the coarse-grained molecules. For practical reasons the interaction series must be truncated, and this truncation generates a lack of consistency between the original model and the CG one. The most common (and practical) choice is to consider only pairwise-additive interactions, an approximation which is only reliable if the average density is low. Indeed, when the density is increased the average intermolecular distance is reduced, so that different particles interpenetrate; on these distances, many-body interactions become relevant and cannot be neglected. The density scale at which these multiple overlaps start to occur is the **overlap density** defined in Eq. (2.8)

$$\rho_p^* = \frac{3}{4\pi \hat{R}_g^3}, \tag{3.22}$$

and the corresponding volume fraction is $\Phi_p = \rho_p/\rho_p^* \approx 1$. Therefore, we expect SB models with pairwise additive interactions to be reliable only in the dilute regime, when $\Phi_p \lesssim 1$.

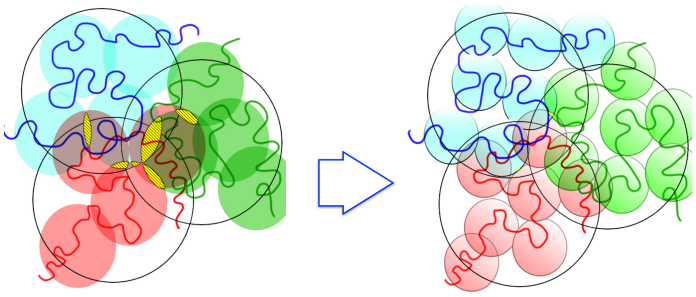

Figure 3.1. Reduction of multiple overlaps by increasing the number of blobs involved in a coarse-grained description of a polymer.

To go further up in density, while keeping only pairwise additive intermolecular interactions, we introduce **multiblob models** [83, 84]: switching to a lower level of coarse graining with respect to the single-blob case, we now map each polymer onto a soft n-atomic particle with n effective interaction sites. This concept is closely connected to the partitioning of polymers in blobs as discussed in Sec. 2.3.3.
In SB models, the density scale for the occurrence of multiple overlaps (i.e. the validity of the pairwise-additive approximation) is fixed by the overlap density ρ_p^*

defined in Eq. (2.8), which is connected to the average dimension of the polymer $\hat{R}_g$. In a multiblob representation the basic unit is the blob, so it should be reasonable to define multiple overlaps in terms of those arising among blobs belonging to different molecules. These overlaps take place at a scale which is not of the order of the dimension of the whole molecule, but rather of the order of the size of the blob $r_{g,b}$. If we consider each blob to be composed of $m = L/n$ monomers, where $1 \ll m \ll L$, the scaling relation of Eq. (2.55), $r_{g,b} \sim m^{\nu}$, holds. Defining the blob density $\rho_b = N_p n/V = \rho_p n$, and the **blob overlap density**

$$\rho_b^* = \frac{1}{V_b} = \frac{3}{4\pi r_{g,b}^3}, \tag{3.23}$$

where V_b is the average volume occupied by a blob, the condition $\rho_b < \rho_b^*$ that no multiple overlap occur among blobs belonging to different polymers becomes

$$\frac{\rho_b}{\rho_b^*} = \frac{4\pi}{3}\rho_b r_{g,b}^3 \lesssim 1. \tag{3.24}$$

The condition in Eq. (3.24) can be translated in terms of the volume fraction Φ_p by noting that $r_{g,b} \sim \hat{R}_g/n^{\nu}$. One obtains

$$\rho_b < \rho_b^* \longrightarrow \Phi_p \lesssim n^{3\nu-1}. \tag{3.25}$$

Eq. (3.25) has several interesting consequences: on one hand, it sets up the range of validity in Φ_p of a multiblob model based on zero-density pair potentials, for a given number of effective sites n. Moreover, it shows that the density range can (in principle) be widened by increasing the number of blob composing each polymer, a task which is however quite difficult in practice as n increases, due to the complexity in determining intramolecular interactions.
At this stage, Eq. (3.25) has been obtained by means of purely geometrical considerations. An equivalent, more physical derivation is based on the scaling behavior of the correlation length ξ defined in Eq. (2.53). As in all coarse-graining strategies, the large-scale behavior of the system does not change as soon as we group together degrees of freedom on scales much smaller that the macroscopic one, which is of the order of the correlation length ξ. In the case of CG models of polymers, we must be sure that the partitioning of the original molecule into mesoscopic units (or blobs) is such that the average size of the blob $r_{g,b}$ does not exceed the correlation length ξ. By combining the scaling behavior of the correlation length in the semidilute regime in Eq. (2.53) and the scaling relation

$$\frac{r_{g,b}}{\hat{R}_{g,0}} \sim n^{-\nu}, \tag{3.26}$$

and requiring that

$$\frac{r_{g,b}}{\hat{R}_{g,0}} \ll \frac{\xi(\Phi_p)}{\hat{R}_{g,0}}, \tag{3.27}$$

we again obtain

$$\Phi_p \lesssim n^{3\nu-1}, \tag{3.28}$$

which is equivalent to Eq. (3.25). As soon as Eq. (3.25) holds, the effects of many-body intermolecular interactions among polymers should be negligible.
In multiblob models, one maps each molecule onto a set of interaction sites $\mathbf{R}_{\alpha,i}$, $\alpha = 1,\dots,N_p$, $i = 1,\dots,n$. As in SB models, there is no clear prescription on how these sites should be chosen, *i.e.* on the representation of the coarse-grained molecule. One possibility consists on grouping together m microscopic units into a larger subunit, thus partitioning the original molecule into $n = L/m$ interaction sites [84]. The position vector of the j-th monomer of the i-th subunit belonging to molecule α is denoted by $\mathbf{r}^{(j)}_{\alpha,i}$, where $\alpha = 1,\dots,N_p$, $i = 1,\dots,n$ and $j = 1,\dots,m$. We then take as effective coordinate of each blob the center of mass of each subset

$$\mathbf{R}_{\alpha,i} = \mathbf{T}[\{\mathbf{r}^{(j)}_{\alpha,i}\}] = \frac{1}{m}\sum_{j=1}^{m}\mathbf{r}^{(j)}_{\alpha,i}. \tag{3.29}$$

As discussed in Sec. 3.1, the total *exact* interaction potential among the $N_p n$ effective sites is

$$V_{N_p} = V_{N_p}(\{\mathbf{R}_{1,i_1}\},\dots,\{\mathbf{R}_{N_p,i_{N_p}}\}), \tag{3.30}$$

and depends on $3(N_p n - 2)$ scalar combinations of the variables $\{\mathbf{R}_{\alpha,i}\}$ due to translational and rotational invariance. Its determination is in principle much more complex than the single-blob case, hence approximations must be introduced.
In analogy with the discussion developed in Sec. 3.1, we can perform a zero-density expansion of the total partition function. The total interaction can be written as

$$V_{N_p}(\{\mathbf{R}_{\alpha,i}\}) = V^{(0)}(N,V) + V^{(1)}(\{\mathbf{R}_{\alpha,i_\alpha}\}) + V^{(2)}(\{\mathbf{R}_{\alpha,i_\alpha}\}) + V^{(3)}(\{\mathbf{R}_{\alpha,i_\alpha}\}) + \dots, \tag{3.31}$$

where the $V^{(k)}(\{\mathbf{R}_{\alpha,i_\alpha}\})$, $k = 1,\dots,N_p$ are k-polymer intermolecular interactions which depend on the whole set $(\{\mathbf{R}_{1,i_1}\},\dots,\{\mathbf{R}_{k,i_k}\})$, $i_1,\dots,i_k = 1,\dots,n$, and are defined in the zero-density limit.
The one-body term $V^{(1)}$ defines intramolecular interactions

$$V^{(1)}(\{\mathbf{R}_{\alpha,i_\alpha}\}) = \sum_{\alpha=1}^{N_p} V^{\text{intra}}(\{\mathbf{R}_{\alpha,i_\alpha}\},n), \quad i_\alpha = 1,\dots,n, \tag{3.32}$$

where $V^{\text{intra}}(\{\mathbf{R}_{\alpha,i_\alpha}\},n)$ is the intramolecular potential among the sites $\{\mathbf{R}_{\alpha,i_\alpha}\}$ belonging to the molecule α, accounting for the connectivity and the interactions among them.
The term $V^{(2)}$ is pairwise additive between the polymers

$$V^{(2)}(\{\mathbf{R}_{\alpha,i_\alpha}\}) = \sum_{\alpha<\beta=1}^{N_p} V^{\text{inter}}(\{\mathbf{R}_{\alpha,i_\alpha}\},\{\mathbf{R}_{\beta,i_\beta}\}), \tag{3.33}$$

where $V^{\text{inter}}(\{\mathbf{R}_{\alpha,i_\alpha}\},\{\mathbf{R}_{\beta,i_\beta}\})$ is the total intermolecular interaction among the $2n$ sites belonging to polymers α and β.
Now, we assume that by reducing the average volume occupied by each molecule we have consequently reduced multiple overlaps, hence it should be reasonable to neglect all the interaction terms $V^{(k)}$, $k \geq 3$, thus retaining only pair intermolecular interactions.

As it stands, Eqs. (3.32) and (3.33) are not yet suitable for numerical calculations as we are still left with functions of $3(n-2)$ variables (intramolecular interactions) and $3(2n-2)$ variables (intermolecular interactions). Further approximations must be introduced, as we discuss in the following sections.

3.2.1 Intramolecular interactions

The first step is the definition of intramolecular interactions $V^{\rm intra}(\{\mathbf{R}_i\},n)$ among the effective sites $\mathbf{R}_i$, $i=1,\ldots,n$, belonging to a single molecule. Formally, this is not a difficult task. Let us consider a general observable $O(\mathbf{T}[\{\mathbf{r}_i^{(j)}\}])$, $i=1,\ldots,n$, which is a function of the effective coordinates of the molecule $\mathbf{R}_i$ in Eq. (3.29). The average value of this observable is

$$\langle O\rangle = \frac{1}{Q_1}\int D\mathbf{r} e^{-\beta H_1} O(\mathbf{T}[\{\mathbf{r}_i^{(j)}\}]), \tag{3.34}$$

where Q_1 is the single-polymer partition function defined in Eq. (2.25). Translational invariance allows to pick-up the coordinate of one blob, say $\mathbf{R}_1$, and define the positions of the other blobs in terms of the relative coordinates $\mathbf{R}_{1i}=\mathbf{R}_i-\mathbf{R}_1$. By introducing the set of δ-functions

$$1=\prod_{i=2}^{n}\left(\int d\mathbf{R}_{1i}\delta(\mathbf{R}_{1i}-\mathbf{T}[\{\mathbf{r}_i^{(j)}\}]+\mathbf{T}[\{\mathbf{r}_1^{(k)}\}])\right), \tag{3.35}$$

we can rewrite Eq. (3.34) as

$$\langle O\rangle = \int d\mathbf{R}_{12},\ldots,d\mathbf{R}_{1n} P^{(n)}(\mathbf{R}_{12},\ldots,\mathbf{R}_{1n}) O(\mathbf{R}_{12},\ldots,\mathbf{R}_{1n}), \tag{3.36}$$

where we defined the reduced probability distribution function $P^{(n)}$ for the set $\{\mathbf{R}_{1i}\}$, $i=2,\ldots,n$ as

$$\begin{aligned} P^{(n)}(\mathbf{R}_{12},\ldots,\mathbf{R}_{1n}) &= \frac{1}{Q_1}\int D\mathbf{r}\prod_{i=2}^{n}\left(\delta(\mathbf{R}_{1i}-\mathbf{T}[\{\mathbf{r}_i^{(j)}\}]+\mathbf{T}[\{\mathbf{r}_1^{(k)}\}])\right)e^{-\beta H_1} \\ &= \left\langle\prod_{i=2}^{n}\left(\delta(\mathbf{R}_{1i}-\mathbf{T}[\{\mathbf{r}_i^{(j)}\}]-\mathbf{T}[\{\mathbf{r}_1^{(k)}\}])\right)\right\rangle_{\mathbf{R}_1=0}. \end{aligned} \tag{3.37}$$

As usual in the analysis of polymer systems, the relevant quantities are the adimensional combinations

$$\hat{R}_g^{3(n-1)} P^{(n)}(\mathbf{R}_{12},\ldots,\mathbf{R}_{1n}), \tag{3.38}$$

where $\hat{R}_g$ is the average radius of gyration of the molecule, computed in the zero-density limit (one polymer). Indeed, in the scaling limit $L\to\infty$ these distributions tend to **universal** (hence model-independent) functions $\bar{P}^{(n)}$

$$\hat{R}_g^{3(n-1)} P^{(n)}(\mathbf{R}_{12},\ldots,\mathbf{R}_{1n}) \underset{L\to\infty}{\longrightarrow} \bar{P}^{(n)}(\mathbf{b}_{12},\ldots\mathbf{b}_{1n}), \tag{3.39}$$

where we define the adimensional combinations $\mathbf{b}_{1i} = \mathbf{R}_{1i}/\hat{R}_g$, $i = 1, \ldots, n$. The $\bar{P}^{(n)}$ clearly satisfy the normalization condition

$$\int d\mathbf{b}_{12} \ldots \mathbf{b}_{1n} \bar{P}^{(n)}(\mathbf{b}_{12}, \ldots \mathbf{b}_{1n}) = 1. \tag{3.40}$$

The universal intramolecular potential V^{intra} can be defined as

$$\beta V^{\text{intra}}(\{\mathbf{b}_i\}, n) = -\ln \left[\bar{P}^{(n)}(\mathbf{b}_{12}, \ldots, \mathbf{b}_{1n}) \right]. \tag{3.41}$$

This definition ensures that the average value of every observable $O(\mathbf{b}_1, \ldots, \mathbf{b}_n)$, when expressed in terms of the adimensional combinations $\mathbf{b}_i$, agrees in the original and CG model

$$\langle O \rangle = \langle O \rangle_{CG}, \tag{3.42}$$

where

$$\langle O \rangle_{CG} = \frac{\int d\mathbf{b}_1 \ldots d\mathbf{b}_n O(\mathbf{b}_1, \ldots, \mathbf{b}_n) e^{-\beta V^{\text{intra}}(\{\mathbf{b}_i\}, n)}}{\int d\mathbf{b}_1 \ldots d\mathbf{b}_n e^{-\beta V^{\text{intra}}(\{\mathbf{b}_i\}, n)}}. \tag{3.43}$$

Once again, the determination of the full potential $V^{\text{intra}}(\{\mathbf{b}_i\}, n)$ is far too complex in practice: due to translational and rotational invariance, a function of $3(n-2)$ scalar variables should be computed. Moreover, its many-body nature is such that it is not decomposable in terms of two, three, $\ldots, n$-body interactions. Hence, approximation must be introduced.

There is no obvious method to justify the form of the effective interactions. Our coarse-grained model for star polymers, to be presented in Chap. 5, relies on a parametrization based on a set of potentials $V_i^{CG}(x_i)$, $i = 1, \ldots, k$, each depending on a single scalar combination x_i of the blob coordinates. These scalar variables should take into account the original n-body nature of the interactions. The bond lengths $b_{ij} = |\mathbf{b}_i - \mathbf{b}_j|$ are examples of two-body variables, while the bond angles θ_{ij} among two subsequent bond vectors are examples of three-body variables. The potentials are determined in such a way that each distribution function $P_i^{CG}(x_i)$ is equal to the corresponding distribution $P_i^{FM}(x_i)$ determined by Monte Carlo simulations of the full-atomistic system. The set $V_i^{CG}(x_i)$ is then obtained by requiring that

$$P_i^{FM}(x_i) = P_i^{CG}(x_i). \tag{3.44}$$

We computed these effective interactions by means of the iterative Boltzmann inversion method [49]: starting from a reference potential $V_{0,i}^{CG}(x_i)$ (which can be chosen, for example, as $V_{0,i}^{CG}(x_i) = -\ln[P_i^{FM}(x_i)]$), by means of a Monte Carlo simulation on the CG molecules the corresponding $P_{0,i}^{CG}(x_i)$ is obtained. The iterative procedure consists in performing a sequence $(t : 0, 1, ...)$ of Monte Carlo simulations of the coarse-grained system with potentials $V_{(t,i)}^{CG}(x_i)$. After each simulation, a new potential $V_{(t+1,i)}^{CG}(x_i)$ is obtained as a correction of $V_{(t,i)}^{CG}(x_i)$ by using

$$V_{(t+1,i)}^{CG}(x_i) = V_{(t,i)}^{CG}(x_i) - a \ln \left(\frac{P_i^{FM}(x_i)}{P_{(t,i)}^{CG}(x_i)} \right), \tag{3.45}$$

where $P_{(t,i)}^{CG}(x_i)$ is the CG distribution at step t, and a is real number tuned to improve the convergence of the iterations. If the procedure converges, i.e. $P_{(t,i)}^{CG}(x_i) \to$

$P_i^{FM}(x_i)$, it provides the correct multiblob potential.
It is important to notice that this parametrization ensures that the coarse-grained model reproduces the distribution functions $P_i(x_i)$ of the scalar variables x_i, but in general **will not** reproduce exactly **every** distribution function $\tilde{P}(\mathbf{b}_1, \ldots, \mathbf{b}_k)$, $2 < k \leq n$.

3.2.2 Intermolecular interactions

At last, we need now to define the intermolecular effective potential V^{inter} among the CG effective sites. As we said in Sec. 3.2, we first neglect all the interactions among three or more molecules. The potential between two polymers

$$V_{12}^{\text{inter}}(\{\mathbf{R}_{1,i_1}\}, \{\mathbf{R}_{2,i_2}\}), \quad i_1, i_2 = 1, \ldots, n, \tag{3.46}$$

is in principle a function $3(2n-2)$ variables due to translational and rotational invariance. We can try to simplify it further by using the fact that our model is supposed to work only up to the overlap density of the blobs. Therefore, since multiple overlaps among blobs belonging to different molecules do not occur, it should be reasonable to treat the total intermolecular interaction (3.46) as **pairwise-additive between the blobs**. With this assumption, we can write Eq. (3.46) as

$$V_{12}^{\text{inter}}(\{\mathbf{R}_{1,i_1}\}, \{\mathbf{R}_{2,i_2}\}) = \sum_{i,j=1}^{n} v^{(i,j)}(|\mathbf{R}_{1,i} - \mathbf{R}_{2,j}|), \tag{3.47}$$

where $v^{(i,j)}$ is the interaction potential between the i-th blob of molecule 1 and the j-th blob of molecule 2, and is only a function of the distance due to rotational and translational invariance. Note that different sites can in principle interact by means of different potentials, so that the superscript (i,j) cannot be omitted in general. While intramolecular interactions were obtained by requiring the coarse-grained model to reproduce the correct polymer structure at zero density (one polymer), we need to determine the set of intermolecular blob-blob pair potentials $v^{(i,j)}$, appearing in Eq. (3.47), which correctly reproduce the zero-density thermodynamics of the underlying polymer system. The fundamental tools for testing the validity of the CG model are again the adimensional virial coefficients $A_i = B_i/\hat{R}_g^{3(i-1)}$ defined in Sec. 2.3.2.1. Indeed, as we saw in Sec. 3.1, they are strictly related to the structural properties of the polymer. At the level of two polymers, we then look for intermolecular interactions $v^{(i,j)}$ for which

$$A_2^{MB} = A_2^{FM}. \tag{3.48}$$

At higher orders, since we are still neglecting three,$\ldots, N_p$-polymer interactions, we know from Sec. 3.1 that we will not be able to reproduce *exactly* the virial coefficients A_i, $i \geq 3$. On the other hand, the multiblob model should have reduced the relevance of many-body intermolecular interactions: we therefore expect the third virial coefficient A_3^{MB} of the MB model to better reproduce the full-monomer predictions for A_3^{FM}, with respect to the single-blob case. This assertion can be *a posteriori* verified by means of a direct comparison of FM, SB and MB results.
In order to determine the functional form of intermolecular interactions, we now

need to find some target intermolecular properties that the coarse-grained model must reproduce, keeping in mind that Eq. (3.48) must hold.
Eq. (2.38) in Sec. 2.3.2.1 showed that the polymer second virial coefficient can be written as

$$B_2 = -\frac{1}{2}\int d\bar{\mathbf{r}}_{12}\,\langle f_{12}\rangle\,|_{0,\bar{\mathbf{r}}_{12}}, \tag{3.49}$$

where

$$f_{12} = \exp(-\beta H_{12}^{\text{inter}}) - 1, \tag{3.50}$$

and the average is performed over two isolated polymers, keeping two sites fixed at positions $\bar{\mathbf{r}}_1 = 0$ and $\bar{\mathbf{r}}_2 = \bar{\mathbf{r}}_{12}$. H_{12} is the total intermolecular interaction among the two molecules. The second virial coefficient B_2 in Eq. (3.49) is related to the potential of mean force among two sites i, j

$$\beta W_{ij}(r) = -\ln[\langle \exp(-\beta H_{12}^{\text{inter}})\rangle_{0,\bar{\mathbf{r}}_{ij}}]. \tag{3.51}$$

It should be noted that in Eq. (3.51) **the choice of the sites is completely arbitrary**. Therefore, we can equivalently pick-up any pair of effective coordinates defined in the MB model ($\mathbf{R}_{1,i}$, $\mathbf{R}_{2,j}$), $i, j = 1\ldots, n$, as reference sites, and compute

$$\beta W_{ij}(r) = -\ln[\langle \exp(-\beta H_{12}^{\text{inter}})\rangle_{0,\mathbf{R}_{ij}}] \tag{3.52}$$

at the full-monomer level. The resulting second virial coefficient B_2 is the same. The relative coordinate $\mathbf{R}_{ij} = \mathbf{R}_{2,j} - \mathbf{R}_{1,i}$ is written in terms of the microscopic coordinates by means of Eq. (3.29).
Universality again constraints the shape of these potentials of mean force, since in the scaling limit $L \to \infty$ they tend to **universal functions** $\overline{W}_{ij}$

$$\beta W_{ij}(r) \underset{L\to\infty}{\longrightarrow} \beta\overline{W}_{ij}(b), \tag{3.53}$$

where $b = r/\hat{R}_g$.
The functions $W_{ij}(r)$, $i, j = 1, \ldots, n$ in Eq. (3.52) can now be used as target quantities for the determination of the total intermolecular potential in Eq. (3.47). Indeed, if we are able to find a set of coarse-grained potentials $v^{(i,j)}$ for which we have

$$\beta W_{ij}^{CG}(r) = \beta W_{ij}^{FM}(r), \qquad \forall i, j = 1, \ldots, n, \tag{3.54}$$

where

$$\beta W_{ij}^{CG}(r) = -\ln[\langle \exp(-\beta V_{12}^{\text{inter}})\rangle_{0,\mathbf{R}_{ij}}] \tag{3.55}$$

is computed in the CG model and βW_{ij}^{FM} in a convenient microscopic model, we are guaranteed of the consistency between the second virial coefficients A_2^{MB} and A_2^{FM}. Moreover, since **the whole set** of W_{ij}^{FM}, $i, j = 1, \ldots, n$ is reproduced, we are sure that the second virial coefficient A_2^{MB} of the MB model is independent on the choice of the sites as it was in the original, microscopic model.
The determination of the intermolecular potentials $v^{(i,j)}$, $i, j = 1, \ldots, n$, which satisfy this condition is performed by means of the iterative Boltzmann inversion method. We start from a guessed set of potentials $v_0^{(i,j)}(r)$, and by means of a Monte Carlo simulation of the CG molecules the potentials of mean force $W_{0,ij}^{CG}(r)$ are obtained.

We then perform a sequence $(t : 0, 1, \ldots)$ of Monte Carlo simulations of the CG model with a set of potentials $v_t^{(i,j)}(r)$. After each simulation, we define the new potentials $v_{t+1}^{(i,j)}(r)$ as corrections of the set $v_t^{(i,j)}(r)$ by means of

$$v_{t+1}^{(i,j)}(r) = v_t^{(i,j)}(r) - a_{ij}[W_{t,ij}^{CG}(r) - W_{ij}^{FM}(r)], \tag{3.56}$$

where the $W_{t,ij}^{CG}(r)$ are the mean-force potentials obtained at time t. If this procedure converges and $W_{ij}^{CG}(r) \to W_{ij}^{FM}(r)$, we have determined the set of multiblob intermolecular potentials $v^{(i,j)}(r)$ which reproduce the full-monomer second virial coefficient A_2^{FM}.

Chapter 4

Colloid/linear-chain mixtures

Macromolecular fluid mixtures received a lot of attention in the last decades, due to the huge number of additional properties that these systems present with respect to the pure component case, with many relevant technological applications. Indeed, these soft-matter systems show complex physical behaviors, including a variety of fluid-fluid and fluid-solid transitions, glassy behaviors, microphase separations and supramolecular self-assembly. We consider mixtures of polymers, both synthetic or biological, and colloids, which, according to the International Union of Pure and Applied Chemistry are particles characterized by an extension which lies, in at least one direction, between 1 nm and 1 μm. As for the case of polymers, it is nowadays possible to realize and investigate, both theoretically and experimentally, a large variety of colloidal particles, each one with its very peculiar features, which differ in shape as well as in the nature of their interactions.
In this chapter, we analyze the thermodynamic and structural properties of mixtures composed by electrically neutral linear chains and spherical colloids, using a coarse-grained (CG) approach. The task is that of characterizing the phase diagrams for different ratios of their characteristic sizes,

$$q = \hat{R}_g / R_c \tag{4.1}$$

where $\hat{R}_g$ is the average, zero-density radius of gyration of the polymer and R_c is the radius of the colloid.
In analogy with what occurred in polymer solutions, these systems exhibit **separation of scales**. On one hand, microscopic properties strongly depend on the microscopic details: on these scales, a full-atomistic description of the polymer, of the solvent molecules as well as a realistic description of the colloid, both in structure and interactions, are needed. This level of detail is important, for example, if one wants to characterize the adsorption of a polymer on the rough surface of a large colloidal particle. On the other hand, several large-scale and thermodynamic properties, including the phase diagram, do not depend on this level of detail, but to a large extent only on the quality of the solvent and on the ratio q defined in Eq. (4.1). In good-solvents, for example, the osmotic coefficient $Z = \beta P/(\rho_p + \rho_c)$, where P is the osmotic pressure, $\rho_p = N_p/V$, $\rho_c = N_c/V$ and N_p and N_c are the number of polymers and colloids in the system, tends in the scaling limit $L \to \infty$ to

a universal (*i.e.* model-independent) function

$$Z(\rho_p, \rho_c, L, R_c) \underset{L\to\infty}{\longrightarrow} \bar{Z}(\Phi_p, \Phi_c, q), \tag{4.2}$$

when expressed in terms of the polymer volume fraction $\Phi_p = \frac{4}{3}\pi\rho_p\hat{R}_g^3$ and of the colloid volume fraction $\Phi_c = \frac{4}{3}\pi\rho_c\hat{R}_c^3$.
Once again, universality allows us to pick up one particularly convenient, simplified microscopic model, which is able to capture the correct large-scale behavior of the system. Therefore, polymers can be represented by means of the implicit-solvent models defined in Sec. 2.3.1, while colloids can be modeled as hard spheres of radius R_c. This is a first, theoretically driven, level of coarse graining. A second level of coarse graining is again dictated by necessity: the determination of high molecular-weight properties becomes more and more computationally demanding as the density increases, due to the huge number of degrees of freedom involved in an (although simplified) full-atomistic description. Therefore, most of the theoretical and numerical investigations on these systems relied on approximate theories as the coarse-grained, single blob (SB) models described in Chap. 3, in terms of zero-density or density-dependent interactions [65–69, 72, 75, 76]. In these models, each linear chain is mapped onto a soft monoatomic particle and interactions are parametrized in terms of polymer-polymer and colloid-polymer effective potentials, while the colloid-colloid interaction is the usual hard-sphere potential.
The determination of the polymer-polymer pair potential $u_{pp}^{(2)}$ has been fully described in Sec. 3.1. For what concerns the zero-density colloid-polymer pair potential, its derivation is completely analogous and will be omitted here for the sake of brevity. It is defined by

$$\beta u_{cp}^{(2)}(\mathbf{R}_p, \mathbf{R_c}) = -\ln\langle\exp(-\beta H_{cp})\rangle_{\mathbf{R}_p,\mathbf{R}_c}, \tag{4.3}$$

thus averaging the total intermolecular colloid-polymer interaction H_{cp} over the noninteracting Boltzmann measure, keeping the effective interaction site of the polymer $\mathbf{R}_p$ and the center of the colloid $\mathbf{R}_c$ fixed. This choice ensures that the universal combination $A_{2,cp} = B_{2,cp}/\hat{R}_g^3$ in the virial expansion of the osmotic coefficient in Eq. (4.2)

$$Z = \frac{\beta P}{(\rho_p + \rho_c)} = 1 + \frac{1}{(\rho_p + \rho_c)}(B_{2,pp}\rho_p^2 + B_{2,cp}\rho_p\rho_c + B_{2,cc}\rho_c^2 + \ldots), \tag{4.4}$$

agrees in the coarse-grained, single-blob model and in the original system.
Since the limits of validity of SB models are known, it is useful to perform a critical analysis by comparing their predictions with those of full-monomer (FM) simulations (when possible) and other approximate theories. In this chapter, we will first give a short historical review which illustrates some of the results on the subject presented in the literature. Thereafter, we will compare the thermodynamics of both zero-density and density-dependent SB models for pure polymer solutions with full-monomer results. This will allow us to understand the merits/demerits of the different single-blob strategies. At last, we will consider linear-chains/colloid mixtures for several values of q, and determine the SB predictions for their structure and phase diagram. We will use Monte Carlo simulations and the integral equation methods presented in Sec. 1.3. A comparison of Monte Carlo simulations of the

CG models and full-monomer results, when possible, will clarify the accuracy of single-blob models in reproducing the properties of the original, microscopic system. A comparison of Monte Carlo simulations and integral equation methods on the SB model will allow us to determine the level of accuracy of the various approximate closure relations in reproducing the exact phase behavior of the single-blob system. These results have been recently published in Refs. [96, 97].

4.1 Historical review and state of the art

The first effective coarse-grained, single blob theoretical description of colloid/polymer mixtures can be dated back to the Asakura-Oosawa-Vrij model (AOV) [54, 55], which, although very qualitative, was able to capture some of the fundamental properties of the original problem. In this model, colloids are modeled as hard spheres of radius R_c, while polymers are treated as soft penetrable spheres with an effective radius $\hat{R}_g$: the colloid-polymer interaction is a hard-core potential, and there is no polymer-polymer interaction. The AOV model predicts, in addition to the known fluid-solid transition, a fluid-fluid demixing region [56, 57] in the (Φ_c, Φ_p) plane, when the ratio q defined in Eq. (4.1) exceeds the critical value $q_c \sim 0.4$. In this region, a colloid-rich/polymer-poor phase (which in the following we will call **colloidal liquid**) coexists with a colloid-poor/polymer-rich phase (which will be called **colloidal gas**). This phase separation is induced by the so-called depletion attractive interaction [63], which arises between two colloids as a consequence of the average presence of the polymers. The AOV predictions for the phase diagram were found to be in semi-quantitative agreement with those of colloid/polymer mixtures close to the θ-point, for $q \lesssim 1$. Indeed, as we saw in Chaps. 2 and 3, in this limit the universal second polymer virial coefficient $A_{2,pp} = B_{2,pp}/\hat{R}_g^3$ and the effective pair interaction among two polymers vanishes. The failure of a single-site representation for the polymer in the case $q \gtrsim 1$ can be understood by noting that in this regime, since polymer are larger than the colloids, they can easily wrap around them, a situation which is absent in single-blob models.

An analogous phase behavior is present in the case of mixtures of colloid and interacting polymers [85–90]. In order to represent colloid-polymer mixtures in good solvents by means of a coarse-grained approach, interactions among polymers must be reintroduced. This was done by means of phenomenological extensions of the AOV model [58–62], in which polymer-polymer and colloid-polymer interactions were either oversimplified or guessed. However, the correct universal behavior for the phase diagram of the system can only be obtained by using the correct scaling-limit potentials.

For what concerns the polymer pair potential, the first estimates can be traced back to the seminal work of Flory and Krigbaum [65]. They showed that, in the center of mass (CM) representation, the effective pair potential $u^{(2)}(b)$ of Eq. (3.21) is approximately Gaussian, with a range of the order of the radius of gyration of a single chain. Though the functional form of the interaction was reasonable, their mean-field treatment predicted $u^{(2)}(b = 0)$ to scale as $L^{0.2}$ with the length L of the polymer, hence it diverged in the scaling, infinite-length limit. Later, simple scaling arguments [66], renormalization-group [67] and numerical [68] calculations confirmed

the overall shape of the interaction but found that, in the scaling limit, the potential is independent of L and it is of the order of k_BT at small distances. More recently, an accurate parametrization of the zero-density, scaling-limit potential in the CM representation was reported by Pelissetto and Hansen [69], by extrapolating the lattice Self-avoiding walks (SAW) results.

For the central monomer (MP) representation the potential is no longer bounded at the origin but diverges logarithmically[1] as $b \to 0$ [79]. This short-range exact behavior was used as a basis in the proposal of qualitative potentials in Refs. [75, 91]. An explicit parametrization of the scaling limit potential in the central monomer representation has been reported by Hsu *et al.* in Ref. [76].

As discussed in Chap. 3, zero-density single-blob models in the pairwise-additive approximation are only accurate for $\Phi_p \lesssim 1$. With the hope of obtaining more accurate results, several state-dependent potentials were proposed, which are defined so as to reproduce some finite-density structural properties obtained at the full-monomer level. In the CM representation, a state-dependent pair potential was proposed in Refs. [70–72], and a complete comparison between the underlying FM system and the CG model, mainly focused on thermodynamic, interfacial and large-scale structural properties, was reported. In particular, Ref. [72] reported an explicit parametrization of the density-dependent pair potential obtained by matching the CM-CM pair distribution function for SAWs with $L = 500$ monomers.

For what concerns the colloid-polymer potential, Ref. [92] obtained it in the CM representation by means of scaling-limit extrapolations of Monte Carlo simulations of SAWs. A phenomenological potential in the central monomer representation was instead proposed in Ref. [91]. A parametrization for the CM representation of the state-dependent colloid-polymer potential is reported in Ref. [72], again for SAWs with $L = 500$ monomers.

By means of these potentials, the phase diagrams can be computed with Monte Carlo simulations or integral-equation methods applied to the coarse-grained, single-blob system.

An integral equation analysis of the phase diagram of the zero-density qualitative single-blob model of Refs. [75, 91] in the central monomer representation is reported in Ref. [95]. The same model was studied by Monte Carlo simulations in Ref. [94].

For pure star polymer liquids (we remind that a linear chain is obtained by choosing $f = 2$ in the star polymer model), in Ref. [77] the thermodynamics of these qualitative models has been compared with that obtained by using the scaling-limit SB models of Ref. [76], finding a very poor agreement. Here we do not consider these phenomenological models. Our analysis will be based on single-blob potentials only obtained by direct full-monomer simulations in the large-L limit.

In the case of the state-dependent SB interactions proposed in Ref. [72], the phase diagram has been determined by means of Monte Carlo simulations and reported in Ref. [93]. Once again, the presence of a q-dependent fluid/fluid coexistence region in the plane (Φ_c, Φ_p) was confirmed.

In order to assess the reliability of single-blob results (both zero-density and state-

[1] As we will discuss in Chap. 5, this behavior is obtained from the theoretical prediction for star polymers in the central monomer representation. When the number of arms in the star is $f = 2$, a star polymer becomes a linear chain in the central monomer representation.

dependent), their prediction should be compared, when possible, with full-monomer results. FM studies of the phase diagram have been reported in Ref. [98]. Monte Carlo simulation of SAW models with $L = 2000$, determined the phase diagram in the protein limit case $q \gtrsim 1$, where SB model predictions are not reliable.
More recent full-monomer results are reported in Refs. [99–101]. In Ref. [100] the phase diagram of colloid/polymer mixtures for $q = 1$ is presented, although with relatively short chains. Therefore, in order to obtain the correct scaling behavior extrapolations must be performed.
In addition to single-blob models, there exist other approximate methods to determine the phase diagram of colloid/polymer mixtures. Among them, it is useful to mention the free-volume theory (FVT). Originally proposed as an approximate way of determining the phase diagram of noninteracting polymers and colloids (in an AOV model perspective), it has been later modified in order to take into account interactions among polymers [63] (generalized free-volume theory or GFVT). Recently, starting from very accurate scaling limit results obtained at a full-monomer level [102, 103], this theory has been applied to the case of colloid/polymer mixtures in the crossover regime from good to θ-solvents [104].

4.2 CG models for polymer solutions

In order to determine the reliability of the coarse-grained, single-blob approach in the description of colloid-polymer mixtures, it is useful to start the discussion by first considering the case of pure polymer solutions. In this section we will review this single-site CG strategy, comparing quantitative results obtained by using zero-density and density-dependent potentials.

4.2.1 Zero-density single-blob models

As we discussed in Chap. 3, in zero-density SB models every polymer is mapped onto a soft monoatomic molecule by choosing an effective interaction site. Since the choice of the reference site is in principle arbitrary, it is interesting to compare the thermodynamic and structural properties obtained by using different representations. At a pairwise-additive level, one needs the zero-density pair potential $u^{(2)}(b)$ among two polymers, $b = r/\hat{R}_g$, which can be computed from the pair distribution function $\mathcal{G}^{(2)}(b)$, as explained in Eq. (3.10). We determined the effective potential by means of Monte Carlo simulations of the lattice Domb-Joyce (DJ) model defined in Eq. (2.21), for $w \approx 0.5058$ at which the leading-order corrections to scaling are absent, in the central monomer (MP) and center of mass (CM) representations. Results are reported in Fig. 4.1 for $L = 2400$.
For the CM representation, an accurate parametrization of $u^{(2)}(b)$ in the scaling limit was determined by Pelissetto and Hansen [69], using a linear combination of three Gaussian functions:

$$u^{(2)}_{CM}(b) = \sum_{i=1}^{3} a_i \exp(-b^2/c_i^2), \tag{4.5}$$

with $a_1 = 0.999225$, $a_2 = 1.1574$, $a_3 = -0.38505$, $c_1 = 1.24051$, $c_2 = 0.85647$, and $c_3 = 0.551876$. Such a parametrization was obtained by fitting scaling results

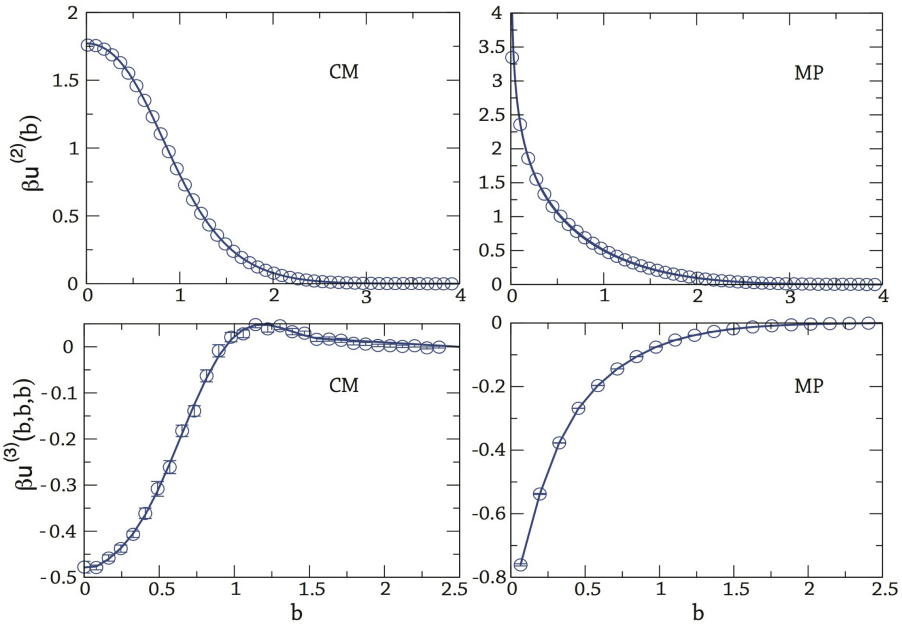

Figure 4.1. Top: Effective pair potential $u^{(2)}(b)$, $b = r/\hat{R}_g$ in the CM (left) and MP (right) representations as a function of $b = r/\hat{R}_g$. We report (circles) numerical DJ results and (full lines) the corresponding parametrizations (4.5) and (4.6). Bottom: Effective three-body potential $\beta u^{(3)}(b, b, b)$ as computed in the CM and MP representations as a function of $b = r/\hat{R}_g$. The simulation results are obtained by means of Monte Carlo simulations of the DJ model. For the CM representation, DJ results agree with those obtained by using the SAW model [69], as expected on the basis of universality.

obtained by extrapolating athermal SAW data. This curve falls on top of the Domb-Joyce result, see Fig. 4.1, further confirming the universality of $u^{(2)}(b)$. In the MP representation, the potential $u^{(2)}(b)$ has been discussed at length in the context of star polymers. For $b \to 0$ it diverges logarithmically as $\ln(1/b)$ [75, 79, 81]. An explicit parametrization has been given by Hsu et al. (see their results for a two-arm star polymer) [76],

$$u^{(2)}_{MP}(b) = \frac{1}{\tau} \ln \left[\left(\frac{\alpha}{\beta} \right)^{\tau\beta} \exp(-\delta b^2) + \exp(\tau\gamma e^{-\delta b^2}) \right] \tag{4.6}$$

where $\alpha = 1.869$, $\beta = 0.815$, $\gamma = 0.372$, $\delta = 0.405$, $\tau = 4.5$. As we explained in Sec. 3.1, the accuracy of the parametrization for the pair potential $u^{(2)}(b)$ in reproducing the zero density thermodynamics of the original system can be checked by means of the universal adimensional ratio $A_2 = B_2/\hat{R}_g^3$. Indeed, Eq. (3.17) implies

$$A_2 = \frac{B_2}{\hat{R}_g^3} = -\frac{1}{2} \int d\mathbf{b} \left(e^{-\beta u^{(2)}(b)} - 1 \right). \tag{4.7}$$

An accurate Monte Carlo estimate of the dimensionless ratio A_2 for polymers under good-solvent conditions is 5.500(3) [78]. If instead we use parametrizations of Eqs. (4.5) and (4.6) to compute the integral (4.7), we obtain $A_2 = 5.48$ (CM) and

$A_2 = 5.51$ (MP), respectively. They are quite close to the direct full-monomer (FM) estimate, confirming the accuracy of the two parametrizations.
In an *exact* CG SB procedure, many-body interaction potentials $u^{(n)}$, $n \geq 3$ must be introduced. For what concerns three-body interactions, the determination of $u^{(3)}$ defined in Eq. (3.16) requires the computation of a triplet correlation, a function of three independent scalar variables, which is a cumbersome simulation task. Therefore, we only show results for polymer configurations whose CG sites are on the vertices of an equilateral triangle of side b. The simulations results for the Domb-Joyce model are reported in Fig. 4.1. While in the MP representation the effective potential is purely attractive and diverging to $-\infty$ as $b \to 0$ (a result that can be proved on general grounds [80, 81]), in the CM representation it is soft, attractive at short distance $b < 1$, and with a small repulsive tail for $b > 1$. For the CM representation, four-body and five-body were also determined [73], at least for some particular polymer configurations. In particular, at least up to $n = 5$, it was found that the generic n-body potential at small distances is positive (repulsive) for even n's and negative (attractive) for odd n's. Moreover, the strength of the n-body potential at small distances decreases for increasing n. For the MP representation this behavior was proved for all values of n and generic star polymers with f arms [81]: moreover, it was shown that the n-body potential at full overlap $b_1 = ... = b_n = 0$ decreases logarithmically with n, at least for star polymers with a large number of arms.
The full computation of the many-body terms is difficult and of little practical use, since numerical simulations of the model using three-body or higher-order interactions would be unfeasible. Indeed, the computational cost grows as N_p^n, where n is the largest order included and N_p is the number of constituents of the system. Therefore, in most of the applications the many-body expansion is truncated, considering only the zero-density pair potential of mean force of Eq. (3.10). It is therefore important to quantify the accuracy of this very simplified effective model. As a first check of its accuracy, we consider the universal third-virial combination $A_3 = B_3/\hat{R}_g^6$, which depends explicitly on the three-body interaction term, see Eq. (3.18). Thus, comparison of A_3 computed in the full-monomer model with the value computed in the CG models provides us with a direct estimate of the quantitative relevance of the neglected three-body interactions. For polymers in the scaling limit $A_3 = 9.90(2)$ [78]. Using Eq. (3.18) with $u^{(3)} = 0$ and the parametrizations of Eqs. (4.5) and (4.6) we obtain instead $A_{3,CM} = 7.85$ and $A_{3,MP} = 4.92$ respectively. The coarse-grained model underestimates the full-monomer value $A_3 = 9.90(8)$ in both cases: by 21% in the CM case and by 50% in the MP case, respectively. This shows that three-body interactions are relevant: if they are neglected, the pressure may be significantly underestimated. Similar conclusions are reached by directly comparing the equation of state. A simple estimate of the osmotic coefficient $Z = \beta P/\rho_p$, $\rho_p = N_p/V$ in Eq. (2.6), for the CG system can be obtained by using the random-phase approximation (RPA) [4], which is expected to be accurate for systems with soft potentials and becomes exact for large densities. RPA predicts

$$\begin{aligned} Z_{RPA,CM} &= 1 + 1.71\Phi_p \\ Z_{RPA,CC} &= 1 + 1.54\Phi_p \end{aligned} \tag{4.8}$$

Clearly, the coarse-grained model does not capture the correct scaling of the osmotic

Φ_p	FM	CM-MC	CM-HNC	MP-MC	MP-HNC
0.135	1.187	1.18458(1)	1.185	1.17869(1)	1.182
0.27	1.393	1.38167(1)	1.382	1.36439(1)	1.371
0.54	1.854	1.80067(1)	1.803	1.74840(1)	1.762
0.81	2.371	2.23911(1)	2.241	2.14190(1)	2.162
1.09	2.959	2.70461(1)	2.707	2.55534(1)	2.582
2.18	5.634	4.55607(2)	4.559	4.18703(1)	4.240
4.36	12.23	8.29709(2)	8.303	7.47886(3)	7.584

Table 4.1. Compressibility factor $Z(\Phi_p) = \beta P/\rho_p$ for polymers (FM) in the scaling limit [102] and for the CG model in the center-of-mass (CM) and in the mid-point (MP) representation. Both hypernetted-chain (HNC) and Monte Carlo (MC) predictions are reported.

pressure in the semidilute regime of Eq. (2.51), *i.e.*, $Z \propto \Phi_p^{1.309}$, underestimating the correct result. Moreover, Z depends on the chosen CG representation, a dependence which would be absent in the exact mapping[2]. In particular, consistently with the results for A_3, the osmotic pressure in the CM representation is always larger than the MP representation estimate.

More quantitatively, we can compare the compressibility factor Z in a wide range of densities, representative of both the dilute and semi-dilute regimes. In Table 4.1 we report full-monomer results [102] and estimates obtained by using the CG models. In the latter case, we show both simulation results and estimates obtained by using integral-equation methods with the hypernetted-chain (HNC) closure (they are fully consistent in the whole density range, confirming the accuracy of the HNC closure for soft potentials). The coarse-grained model based on the CM representation appears to be more accurate than that based on the MP representation. However, both approaches show significant deviations from the correct full-monomer estimates in the semidilute regime. This can be easily understood. For Φ_p larger than 1, polymers overlap, so that many-body interactions, neglected in the simple coarse-grained model with pair potentials, play a relevant role.

4.2.2 State-dependent single-blob models

To extend the density range in which CG single-site models with pairwise effective interactions can be used, preserving the pairwise additivity of the model, one can try to introduce state-dependent interactions, as discussed in Sec. 3.1.1. In Ref. [72] an explicit parametrization of the density-dependent pair potential $u^{(2)}(b, \Phi_p)$ was reported. The properties of the SB model have been extensively compared to the underlying full-monomer system [70–72]. This potential was obtained by matching the CM-CM pair distribution function for SAWs with $L = 500$ monomers. Since interactions are soft and the coarse-grained model corresponds to a monoatomic liquid, the inversion procedure was performed by using an integral-equation method

[2]Heuristically, this statement can be understood by noting that the isothermal compressibility is only related to the fluctuations of the number of polymers, a quantity which is invariant under the change of representation.

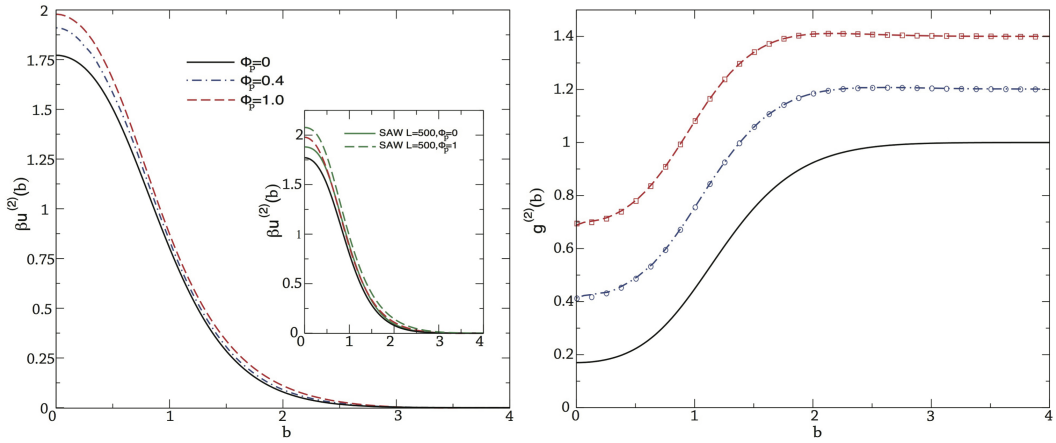

Figure 4.2. Top: Left panel: Effective pair potential $u^{(2)}(b, \Phi_p)$ for different densities, $\Phi_p = 0$, $\Phi_p = 0.4$, $\Phi_p = 1$, as obtained by HNC inversion (CM representation). In the inset we compare the effective potentials obtained in the scaling limit with those appropriate for SAWs with L = 500 sites. Right panel: Radial distribution functions between the polymer centers of mass as obtained by Monte Carlo simulations of the DJ model (lines) and of the CG model with density-dependent potential (squares and circles) for $\Phi_p = 0.4$ and $\Phi_p = 1$. We also report the zero-density distribution function (full line). Data for $\Phi_p = 0.4$ and $\Phi_p = 1$ are shifted upward for clarity.

with the hypernetted-chain closure. This method requires a minimal computational effort and provides accurate estimates of the density-dependent pair potentials.
In Fig. 4.2 we report the effective pair potential $u^{(2)}(b, \Phi_p)$ (CM representation) for linear polymers at $\Phi_p = 0, 0.4, 1$ obtained by using the HNC inversion procedure. The associated $g^{(2)}_{CM}(b; \Phi_p)$ has been computed by FM simulations of the Domb-Joyce model with polymers of length $L = 2400$. At first glance, the potentials appear to be little sensitive to the polymer volume fraction. The value at full overlap increases only slightly with density in the range of polymer volume fractions under consideration. For larger concentrations the strength of the interaction decreases again [70, 71], as a consequence of the screening of the excluded-volume interactions. Moreover, the potential has a slightly longer range compared to the zero-density case, ensuring the correct scaling behavior of the osmotic pressure in the semi-dilute regime. The accuracy of the inversion can be tested by performing Monte Carlo simulations of the CG model and comparing the resulting pair distribution functions with those used as targets in the inversion procedure. From the results shown in Fig. 4.2 we can conclude that the HNC inversion for the CM representation is an accurate method that provides structurally consistent effective pair potentials.
The results for the effective potentials reported in Ref. [72] differ somewhat from those we have determined by using long Domb-Joyce chains, which effectively provide results in the scaling limit. The reason is that in Ref. [72] finite-length SAWs ($L = 500$) were considered, without performing a scaling-limit extrapolation. SAW results are affected by relatively large scaling corrections, which increase with density (for a discussion, see Ref. [102]), even when L is of the order of 10^3. In the zero-density limit, scaling corrections are clearly visible in the result for the

pair potential, which is somewhat more repulsive than the accurate expression of Eq. (4.5), obtained by performing a proper extrapolation to the limit $L \to \infty$. In particular, the value at full overlap ($b = 0$) of the potential exceeds the asymptotic one by 6%. A similar difference is observed for the second virial coefficient, which takes the value $A_2 = 6.18$ if one uses the potential of Ref. [72], to be compared with the value $A_2 = 5.500(3)$ obtained in the scaling limit [78]. To further test the accuracy of the potential, we have determined the potential at $\Phi_p = 1$ by using the pair distribution function obtained from simulations of the DJ model, finding again a discrepancy of approximately 6% for the value at full contact, see Fig. 4.2.
Now we analyze the consistency of the results obtained by using state-dependent interactions. For this purpose, we consider SAWs with $L = 500$ as our underlying system, so that we can use the effective density-dependent potentials reported in Ref. [72], which apply to a large Φ_p interval, up to $\Phi_p = 2.5$. Then, we determine the chemical potential using three different routes, that are equivalent for systems with state-independent interactions. We report results for

$$\beta\hat{\mu} = \ln(\rho_p \hat{R}_g^3) + \beta\hat{\mu}^{\rm exc} \tag{4.9}$$

which differs from the correct chemical potential by an irrelevant, model dependent constant, but which has the advantage of being universal. First, we consider the HNC expression for the chemical potential of Eq. (1.48) [7][8]:

$$\beta\hat{\mu}_{HNC} = \ln\left[\frac{3}{4\pi}\Phi_p\right] + \frac{3}{8\pi}\Phi \int d\mathbf{b}[h(b)^2 - h(b)c(b) - 2c(b)] \tag{4.10}$$

where $h(b) = g^{(2)}(b, \Phi_p) - 1$ and the direct correlation function $c(b)$ is related to Φ_p and $h(b)$ by the Ornstein-Zernike relation defined in Eq. (1.42) [4]. A second possibility consists in determining first the compressibility factor $Z = \beta P/\rho_p$ by means of the virial expression of Eq. (1.35) [4],

$$Z_{\rm vir}(\Phi_p) = 1 - \frac{8\pi^2}{9\Phi_p}\int_0^\infty \frac{\partial\beta u^{(2)}(b,\Phi_p)}{\partial b} g^{(2)}(b,\Phi_p) b^3 db, \tag{4.11}$$

and then in computing $\hat{\mu}$ ($Z-$route)

$$\beta\hat{\mu}_Z(\Phi_p) = \ln\left[\frac{3}{4\pi}\Phi_p\right] + Z_{\rm vir}(\Phi_p) - 1 + \int_0^{\Phi_p} \frac{Z_{\rm vir}(\xi) - 1}{\xi} d\xi. \tag{4.12}$$

Finally, we consider the compressibility route (K-route), which is based on

$$\beta\hat{\mu}_K(\Phi_p) = \ln\left[\frac{3}{4\pi}\Phi_p\right] + \int_0^{\Phi_p} \frac{K(\xi) - 1}{\xi} d\xi \tag{4.13}$$

with $K(\Phi_p)$ given by (see Eq. (1.30))

$$K(\Phi_p)^{-1} = 1 + \frac{3}{4\pi}\Phi_p \int d\mathbf{b}\left[g^{(2)}(b,\Phi_p) - 1\right]. \tag{4.14}$$

For CG models with density-dependent interactions, only the K-route provides the correct chemical potential of the underlying model [51, 52]. Indeed, since the CG procedure reproduces the pair distribution function at any density, $K(\Phi_p)$, defined

Φ_p	HNC-route	Z-route	K-route	FDB	FM scaling
0.25	-1.98	-2.02	-2.03	-1.99	-2.11
0.5	-0.26	-0.36	-0.43	-0.28	-0.62
1.0	3.07	2.77	2.43	3.06	1.89
1.5	6.83	6.14	5.41	6.80	4.35
2.	11.00	9.80	8.59	10.96	6.90
2.5	15.28	13.73	11.98	15.42	9.55

Table 4.2. Polymer chemical potential $\beta\hat{\mu}$ computed in the density-dependent CG model appropriate to describe $L = 500$ SAWs (we use the parametrization of the effective pair potential reported in Ref. [72]). We report results using three different routes (the HNC-route, the Z-route, the K-route), as discussed in the text, and the expression reported in Ref. [53] (FBD). The results labelled "FM scaling" are obtained by using the full-monomer, scaling-limit equation of state reported in Ref. [102].

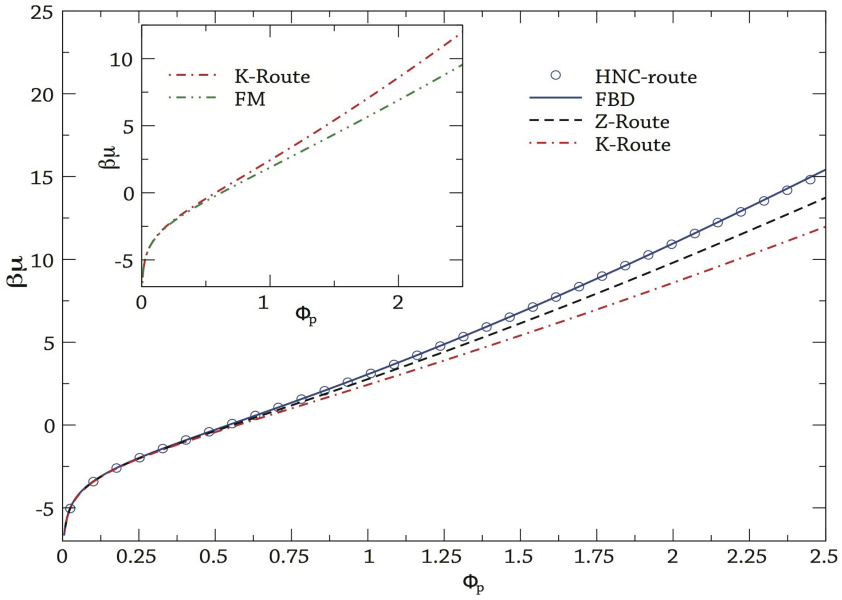

Figure 4.3. Polymer chemical potential $\beta\hat{\mu}$ computed in the density-dependent CG model appropriate to describe $L = 500$ SAWs (we use the parametrization of the effective pair potential reported in Ref. [72]). We report results using three different routes (the HNC-route, the Z-route, the K-route), as discussed in the text, and the expression reported in Ref. [53] (FBD) In the inset we compare the results using the K-route (which are the same as those computed directly by using $L = 500$ SAWs) and the analogous results obtained by using the FM, scaling-limit equation of state reported in Ref. [102].

in Eq. (4.14), is the same in the coarse-grained and in the underlying model. Hence, also $\beta\hat{\mu}_K(\Phi_p)$ defined in Eq. (4.13) is the same. Note also that the Z-route and the K-route both require the effective potential to be computed for all densities smaller than the physical density of interest, hence they have a limited predictive power. Results are reported in Table 4.2 and in Fig. 4.3. It is apparent that inconsistencies between the different routes, well beyond the degree of inaccuracy related to the use

of the HNC method, are present even in the dilute regime. The three different routes provide different predictions, satisfying $\beta\hat{\mu}_{HNC} > \beta\hat{\mu}_Z > \beta\hat{\mu}_K$ for all the densities under consideration. As a consequence, since the K-route estimate agrees with the chemical potential of the underlying system, the HNC-route and the Z-route both overestimate the correct chemical potential. It is interesting to observe that the HNC-route results are equivalent (with a small error due to hypernetted-chain approximation) to those that would be obtained in a direct canonical Monte Carlo simulation by employing Widom insertion method [82], i.e., this route corresponds to the estimate that would be obtained in the approach referred to as *passive* approach in Ref. [52]. In other words, the HNC-route result is the one that would be obtained by using standard thermodynamic relations, disregarding the density dependence of the potential. As a consequence, ensemble equivalence is satisfied. If one performs grand-canonical simulations at chemical potential $\beta\hat{\mu}_{HNC}$ with potential $u^{(2)}(b;\Phi_p)$, one obtains the correct volume fraction Φ_p.[3] However, the fact that ensemble equivalence is satisfied is completely unrelated to the question whether $\beta\hat{\mu}_{HNC}(\Phi_p)$ is a correct estimate of the chemical potential of the underlying system. Indeed, as our results show, $\beta\hat{\mu}_{HNC}(\Phi_p)$ differs significantly from the correct result. Finally, it is interesting to compare $\beta\hat{\mu}_K$ obtained here (which gives the correct chemical potential for $L = 500$ SAWs) with the chemical potential obtained by using the equation of state of Ref. [102], which refers to polymers in the scaling limit. The two quantities are reported in Table 4.2 and in the inset of Fig. 4.3. The SAW model clearly overestimates the scaling-limit result, deviations significantly increasing with Φ_p.

4.3 Colloid/polymer mixtures

We now extend the coarse-grained models in the framework of colloid-polymer mixtures. Relying on the universality of the large-scale properties, colloids will be modeled as hard spheres of radius R_c, while polymers will be modeled in an implicit solvent. As introduced in Sec. 4.1, these systems are particularly interesting as they show a complex phase diagram which depends crucially on the polymer-to-colloid size ratio $q = \hat{R}_g/R_c$: for small ratios, only fluid-solid coexistence is observed, while for larger values an additional fluid-fluid transition is present [85–90]. Even in the absence of an explicit solvent, the computation of the full phase diagram is quite difficult, especially if one is interested in polymers with a large degree of polymerization. Therefore, coarse-grained models represent an important tool to investigate these systems. A first class of CG model is obtained by integrating out all polymer degrees of freedom. The resulting system is a one-component model of colloids interacting via an effective potential. Repeating the discussion of Sec. 3.1, one obtains an effective potential with an infinite number of many-body terms. Computationally it is unfeasible to include more that the leading, two-body term. However, such a truncated model is only predictive when the polymer-to-colloid size ratio q is small. A less extreme approach consists in integrating out only the

[3] Ref. [53] checked that grand-canonical simulations at $\beta\hat{\mu}$ provide the correct value of the density, see their Fig. 4. They also provide a simple parametrization of $\beta\hat{\mu}_{HNC}$: $\beta\hat{\mu} = \ln(\rho_p\hat{R}_g^3) + 0.04658 + 11.05\rho_p\hat{R}_g^3 + 35.48(\rho_p\hat{R}_g^3)^2 - 15.71(\rho_p\hat{R}_g^3)^3$, see Fig. 4.3.

Table 4.3. Coefficients parametrizing $\beta V_{cp}(r;q)$ for different values of q. The parametrization is accurate for $1.91 \le b \le 5.38$, $0.90 \le b \le 4.54$, and $0.47 \le b \le 4.28$ for $q = 0.5, 0.8, 1$, respectively.

q	a_1	e_1	c_1	a_2	e_2	c_2	d_2
0.5	0.634486	0.305183	2.13936	15.1368	0.512611	1.629090	1.30679
0.8	0.411558	0.318504	1.40563	13.5385	0.728577	0.572266	1.56655
1.0	0.982437	0.496784	0.98100	14.1753	0.84914	0	1.6023262

internal degrees of freedom of the polymer, representing each macromolecule with a monoatomic molecule, as already discussed in Sec. 3.1. After this reduction, one obtains a two-component system, comprising colloids and monoatomic CG polymers, which can be studied with much more ease than the original system. Two-component single-site CG models have been considered in several papers [58, 60–62, 92, 93, 95] and also discussed in Ref. [104]. Here, we shall only discuss models in which pair potentials are determined accurately by using full-monomer data, in order to assess the reliability of the single-site model with pairwise interactions (other results are summarized and discussed in Ref. [104]).

In Refs. [103, 105] a careful comparison was performed, considering both the model defined at zero density and that using potentials depending on the polymer density [93], focusing on the solvation properties of a single colloid in a polymer solution and on the thermodynamics in the homogeneous phase. As expected, the model is only accurate if $q = \hat{R}_g/R_c$ is less than 1. The failure of the model when polymers are larger than colloids can be understood physically, by noting that, when $q > 1$, polymers can wrap around the colloids, a phenomenon that cannot be modelled correctly if polymers are represented as soft spheres. Moreover, the CG model is accurate only if the polymer volume fraction Φ_p is less than 1, guaranteeing that the neglected three-polymer interactions are small. Finally, the accuracy decreases with increasing colloid volume fraction $\Phi_c = \frac{4\pi}{3}\rho_c R_c^3$ ($\rho_c = N_c/V$ is the colloid density), since the relevance of the polymer-many-colloid interactions increases in this limit. Hence, we will focus on the phase diagram of colloid-polymer solutions as predicted by CG single-blob models, for polymer-to-colloid size ratios $q = 0.5, 0.8$ and 1.

Zero-density SB models are defined by means of the colloid-polymer and polymer-polymer interactions. For the polymer-polymer potential we used the accurate parametrization in the CM representation reported in Eq. (4.5) [69]. The polymer-colloid pair potential depends on q, and was determined by means of simulation of the Domb-Joyce model, with $L = 2400$. For small values of $b = r/\hat{R}_g$, i.e. for $b < b_{\min}$ ($b_{\min} \approx R_c/\hat{R}_g = 1/q$), the potential $\beta V_{cp}(r;q)$ is large, hence it is impossible (and practically irrelevant) to estimate it accurately. For $b \gtrsim b_{\min}$ we parametrize it as

$$\beta V_{cp}(r;q) = a_1(q) e^{-[(b-c_1(q))/e_1(q)]^2} + a_2(q) e^{-[|b-c_2(q)|/e_2(q)]^{d_2(q)}}, \tag{4.15}$$

where $b = r/\hat{R}_g$. Estimates of the coefficients are reported in Table 4.3.

To verify the accuracy of the parametrization, we compare the estimate of $A_{2,cp} = B_{2,cp}/\hat{R}_g^3$ ($B_{2,cp}$ is the second polymer-colloid virial coefficient in Eq. (4.4)) obtained

by using the parametrized potential and the estimate of the same quantity in the full-monomer model [103]. Using the parametrized potentials we obtain $A_{2,cp} = 106.79, 41.52, 27.50$ for $q = 0.5$, 0.8, and 1, respectively, to be compared with the full-monomer results $A_{2,cp} = 107.4(3)$, 41.7(1), 27.54(6). Differences are small (they are less than 0.6%), confirming the accuracy of the results.
In Sec. 4.3.1 the phase diagram will be investigated by means of Monte Carlo simulations on the single-blob model, both for zero-density and state-dependent potentials, and compared with full-monomer (when possible) or generalized free-volume theory (GFVT) results. This will allow us to determine the reliability of single-blob models in the computation of the phase behavior of the system [96].
In Sec. 4.3.2, we will compute the phase diagram of colloid-polymer mixtures in the CG single-blob approach by means of integral equation methods, and compare it with the SB Monte Carlo results presented in Sec. 4.3.1. In this way, we will then be able to determine the accuracy of the various approximate integral equation methods in reproducing the correct phase behavior of the system [97].

4.3.1 Monte Carlo simulations

Here we determine the phase diagram of polymer-colloid solutions, as predicted by the CG SB models, by means of Monte Carlo simulations. To assess their accuracy we need reference results to compare with. For $q = 1$ we will use full-monomer results of Refs. [99–101]. To the best of our knowledge, there are no such results for $q < 1$, hence we will compare our Monte Carlo estimates for the CG model with the binodals obtained by using the generalized free-volume theory (GFVT) [63, 89, 104], which is expected to become increasingly accurate as q decreases. We consider three values of q, $q = 0.5, 0.8$, and 1. For the CG models with zero-density and density-dependent interactions, we perform standard grand-canonical simulations using a recursive umbrella-sampling algorithm [106, 107]. Insertions and deletions of colloids and polymers are performed by using the cluster moves introduced by Vink and Horbach [108, 109], which considerably improve the performance of the simulation. Simulation parameters are the fugacities z_p and z_c, which are normalized so that $z_p \approx \rho_p \hat{R}_g^3$ and $z_c \approx \rho_c R_c^3$ for $\rho_p, \rho_c \to 0$. Instead of z_c we shall usually quote $\beta\hat{\mu}_c = \ln z_c$, while, as often in the literature, instead of reporting z_p, we will report the volume fraction $\Phi_p^{(r)}$ of a polymer reservoir at the same value of z_p. For the zero-density CG model the reservoir volume fraction can be obtained by inverting the corresponding equation of state ($z_p = e^{\beta\hat{\mu}_p}$) which we have parametrized as:

$$Z(\Phi_p) = \frac{(1 + 6.05117\Phi_p + 11.6205\Phi_p^2 + 10.2588\Phi_p^3)^{1/2}}{(1 + 3.42865\Phi_p)^{1/2}} \tag{4.16}$$

$$\beta\hat{\mu}_p(\Phi_p) = \ln\left[\frac{3}{4\pi}\Phi_p\right] + Z(\Phi_p) - 1 + \int_0^{\Phi_p} \frac{Z(\xi) - 1}{\xi} d\xi. \tag{4.17}$$

4.3.1.1 Results for $q = 1$

Before studying the phase separation of the CG model, we have determined the reference binodal, using the full-monomer results of Ref. [100]. Given the computational complexity of the system, the simulated chains are relatively short. Therefore,

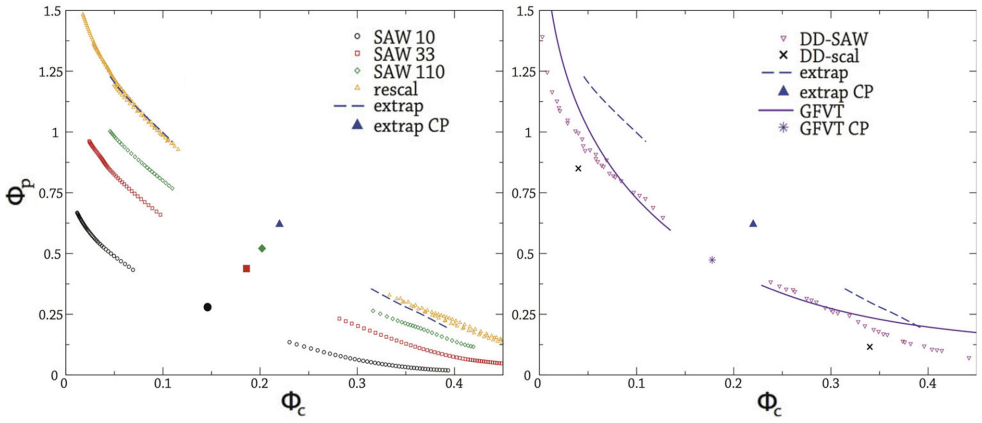

Figure 4.4. Left: binodal curves for $q = 1$ obtained by using the results of Ref. [100]. We report the finite-L data ($L = 10$, $L = 33$, $L = 110$), the extrapolation obtained by using Eq. (4.18) ("extrap"), and the binodal obtained by the simple rescaling mentioned in the text ("rescal") starting from the results with $L = 110$. CP is the extrapolated critical point. Right: we report the FM binodal (extrap), the GFVT prediction, and that obtained in Ref. [93] using polymer-density-dependent potentials appropriate for $L = 500$ SAWs (DD-SAW). We also report two points (crosses, DD-scal) belonging to the binodal obtained using polymer-density-dependent potentials appropriate for scaling-limit polymers.

the results of Ref. [100] show significant corrections to scaling, which should be taken into account before any comparison with the coarse-grained results. The scaling-limit binodal curve can be obtained by extrapolating the data of Ref. [100], along the lines of the critical-point extrapolation performed in Ref. [104]. In Sec. IV.B of Ref. [104] the estimates of the critical points $\Phi_{c,\mathrm{crit}}(L)$ and $\Phi_{p,\mathrm{crit}}(L)$ were considered, for three systems with $L = 10, 33, 110$ and approximately $q = 1$, and the critical point in the scaling limit was determined. The resulting critical point was [104]: $\Phi_{c,\mathrm{crit}}(\infty) \approx 0.22$ and $\Phi_{p,\mathrm{crit}}(\infty) \approx 0.62$. Analogously, if $\Phi_p^{\mathrm{bin}}(L, \Phi_c)$ gives the position of the binodal for the system with chains of length L, we fit the data to[4]

$$\Phi_p^{\mathrm{bin}}(L, \Phi_c) \approx \Phi_p^{\mathrm{bin}}(\Phi_c) + \frac{a_1(\Phi_c)}{\sqrt{L}}. \tag{4.18}$$

The curve $\Phi_p^{\mathrm{bin}}(\Phi_c)$ is our estimate of the scaling-limit binodal. Another less rigorous possibility consists in rescaling the finite-L binodal for each value of the length L, so as to obtain the correct critical point. In other words, we set

$$\Phi_p^{\mathrm{bin}}(\Phi_c) = a\Phi_p^{\mathrm{bin}}(L, b\Phi_c), \tag{4.19}$$

with

$$a = \frac{\Phi_{p,\mathrm{crit}}(\infty)}{\Phi_{p,\mathrm{crit}}(L)} \qquad b = \frac{\Phi_{c,\mathrm{crit}}(L)}{\Phi_{c,\mathrm{crit}}(\infty)}. \tag{4.20}$$

The binodals computed with this method turn out to be essentially independent of

[4] In polymer-colloid mixtures the leading scaling corrections behave as $L^{-\Delta}$, $\Delta \approx 0.52$ and $L^{-\nu}$, $\nu \approx 0.59$, see Ref. [103] for a discussion. The two exponents are very close, so that we simply

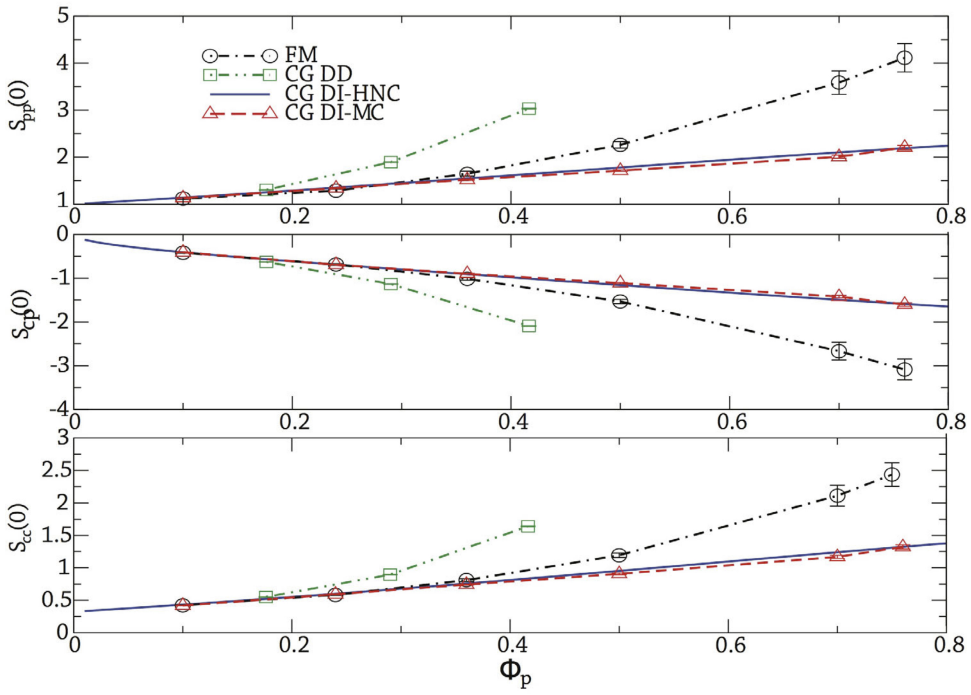

Figure 4.5. Partial structure factors at $k = 0$ as a function of Φ_p for $\Phi_c = 0.15$. We report full-monomer (circles, FM) results obtained by using Domb-Joyce (DJ) chains of length $L = 2400$, CG results obtained by using the zero-density model [Monte Carlo results (triangles, CG DI-MC) and HNC results (lines, CG DI-HNC)], and by using the density-dependent model (squares, CG DD).

the value of L, supporting the method, and quite close to that computed by direct extrapolation. The different extrapolations are reported in Fig. 4.4, together with the corresponding finite-L results.

Once the reference binodal was determined, we considered the single-site, coarse-grained model with zero-density potentials. We systematically increased z_p and for each value of this parameter we performed several runs with different values of z_c, covering colloid volume fractions from 0.1 to 0.35. In all cases no sign of coexistence[5] was observed for systems of size $V = (17.7\hat{R}_g)^3$. Of course, one might fear that systems are too small to allow us to identify a phase transition. Therefore, we repeated the analysis using integral-equation methods. We considered the binary system and used the hypernetted-chain closure defined in Eq. (1.47) for all correlations. Again, no sign of phase separation was observed.

The evidence of a wide region of stability of the homogeneous phase, well beyond the full-monomer phase boundaries, is surprising. Indeed, one does not expect the single-site model to be accurate if colloids and polymers have the same size, hence quantitative differences are not surprising. The unexpected feature is that the CG

extrapolate the data assuming a behavior $a + b/\sqrt{L}$.

[5]For $\Phi_c = 0.1, 0.2, 0.3$ the CG model is homogeneous at least up to $\Phi_p = 2.12, 1.73, 1.33$, respectively, corresponding to $\Phi_p^{(r)} \approx 2.5$.

model is not even able to predict the qualitative behavior of the system.
To understand why the coarse-grained model does not show phase separation, we have determined the partial structure factors $S_{\alpha\beta}(k)$ ($\alpha, \beta = p, c$) defined in Eq. (1.38) and determined their limiting value for $k \to 0$. Such quantities are indeed order parameters of the fluid-fluid transition. We have determined these quantities for the Domb-Joyce model with chains of length $L = 600$ and for the CG model for $\Phi_c = 0.15$ and several values of Φ_p. For the CG model we have determined the structure factors both by performing Monte Carlo simulations, and by using integral-equation methods (we use the hypernetted-chain closure) on very large systems $V = (64\hat{R}_g)^3$.[6] Results are reported in Fig. 4.5. For small polymer volume fractions, the CG and DJ results are in full agreement, but, as Φ_p increases, the CG model significantly underestimates the structure factors. At coexistence, which should occur for $\Phi_p \approx 0.7 - 0.8$, the full-monomer estimates are $S_{pp}(0) \approx 4$, $S_{cc}(0) \approx 2.5$, which are significantly larger than the CG estimates. More precisely, for $\Phi_p = 0.76$ we obtain $S_{pp}(0) = 4.1$ and 2.3 for the DJ and the CG model, respectively. For $S_{cc}(0)$, we obtain correspondingly $S_{cc}(0) = 2.2$ (DJ) and 1.3 (CG). If we further increase Φ_p, the coarse-grained results change only slightly. We obtain $S_{pp}(0) = 2.5$ and $S_{cc}(0) = 1.5$ for $\Phi_p = 1.0$. Clearly, even increasing polymer density the CG system appears to be unable to develop long-range correlations.
The results for the CG model are in contrast with those of Ref. [93], which observed phase coexistence for $q = 1$, using the model with density-dependent interactions. Quantitatively, the binodal obtained in Ref. [93] differs somewhat from that obtained by using the full-monomer estimates, see Fig. 4.4. The results for Ref. [93] refer to SAWs with $L = 500$ monomers, hence one might fear that the differences between the coarse-grained and the full-monomer results are due to the different reference system. To clarify the issue, we have redetermined the density-dependent potential for $\Phi_p = 1$ using scaling-limit, full-monomer data and recomputed the position of the binodal for such a value of Φ_p . We find coexistence between $(\Phi_c, \Phi_p) = (0.04, 0.86)$ and $(0.34, 0.12)$. These two points are also reported in Fig. 4.4. They show that, in the (Φ_c, Φ_p) plane, the binodal computed by using the density-dependent potential appropriate for scaling-limit polymers is located below the one computed in Ref. [93], appropriate for $L = 500$ SAWs. Hence, the differences observed with respect to the full-monomer results are not due to the different reference system, but are a consequence of the CG representation[7]. It is interesting to note that the generalized free-volume theory (GFVT) binodal is essentially on top of the binodal of Ref. [93]. In view of the previous discussion, however, such an agreement looks accidental.
To understand why the coarse-grained model with density-dependent potentials predicts phase separation, we have computed the partial structure factors also in this case. They are shown in Fig. 4.5. It is clear that the model with zero-density

[6] Differences between Monte Carlo and HNC results for the CG model increase with increasing Φ_p, but remain always relatively small, confirming the accuracy of the final results and the absence of significant finite-volume effects. For instance, for $\Phi_p = 1$, beyond the FM binodal, we find $S_{pp}(0) = 2.35(8)$ by canonical simulations and $S_{pp}(0) = 2.46$ by using the HNC closure. Analogously, we obtain $S_{cc}(0) = 1.51(6)$ and 1.62 by using the two methods, respectively.

[7] For $\Phi_c = 0.04$, phase separation occurs for $\Phi_p = 0.97$ (binodal of Ref. [93] obtained by using the CG model appropriate for $L = 500$ SAWs) and $\Phi_p = 1.24$ (full-monomer binodal). For $\Phi_c = 0.34$, phase separation occurs for $\Phi_p = 0.19$ (Ref. [93]) and $\Phi_p = 0.30$ (FM).

potential provides a better approximation to the full-monomer results than that using density-dependent potentials. However, this is not relevant to obtain phase separation. The important point is that the CG model with density-dependent potentials overestimates significantly $S_{pp}(0)$ and $S_{cc}(0)$, hence it exhibits phase separation, while the model with zero-density potentials, although more accurate in the considered range of densities, underestimates $S_{pp}(0)$ and $S_{cc}(0)$, so that no transition occurs, at least in the density range investigated.

$\Phi_p^{(r)}$	$\Phi_c^{(I)}$	$\Phi_p^{(I)}$	$\Phi_c^{(II)}$	$\Phi_p^{(II)}$
0.820	0.164	0.575	0.331	0.336
0.824	0.157	0.588	0.340	0.325
0.827	0.149	0.603	0.351	0.314
0.831	0.140	0.619	0.361	0.301
0.835	0.132	0.635	0.372	0.288
0.838	0.123	0.651	0.382	0.275
0.842	0.115	0.666	0.391	0.265
0.846	0.107	0.680	0.399	0.255
0.849	0.101	0.693	0.407	0.246
0.857	0.089	0.718	0.420	0.231
0.866	0.080	0.740	0.432	0.219

Table 4.4. Binodal line for $q = 0.5$. We report the values of Φ_c and Φ_p in the colloid-gas, polymer-liquid (I) and in the colloid-liquid, polymer-gas (II) phase. Results for cubic boxes of size $31.2\hat{R}_g$.

$\Phi_p^{(r)}$	$\Phi_c^{(I)}$	$\Phi_p^{(I)}$	$\Phi_c^{(II)}$	$\Phi_p^{(II)}$
1.604	0.177	1.09	0.327	0.666
1.610	0.175	1.10	0.330	0.661
1.616	0.173	1.115	0.333	0.655
1.621	0.171	1.125	0.337	0.649
1.627	0.168	1.14	0.340	0.643
1.633	0.166	1.15	0.344	0.637
1.639	0.163	1.16	0.347	0.631
1.645	0.160	1.18	0.351	0.624
1.650	0.157	1.19	0.354	0.617
1.656	0.154	1.20	0.358	0.610
1.662	0.151	1.22	0.362	0.604
1.668	0.148	1.23	0.365	0.597
1.673	0.145	1.24	0.369	0.590

Table 4.5. Binodal line for $q = 0.8$. We report the values of Φ_c and Φ_p in the colloid-gas, polymer-liquid (I) and in the colloid-liquid, polymer-gas (II) phase. Results for cubic boxes of size $23.1\hat{R}_g$.

4.3.1.2 Results for $q = 0.5$ and $q = 0.8$

Let us now consider the behavior for $q = 0.5$ and 0.8. In this case we do not have reference, full-monomer results to compare with. Therefore, we use the GFVT predictions [104] that are expected to become increasingly accurate as q decreases. Moreover, the full-monomer results for $q = 1$ provide us with an upper bound in Φ_p on the correct binodal. For a given value of Φ_c, phase separation for $q < 1$ should occur at polymer volume fractions that are smaller than those at which coexistence occurs for $q = 1$. We limited our investigation here to the CG model with density independent potentials.

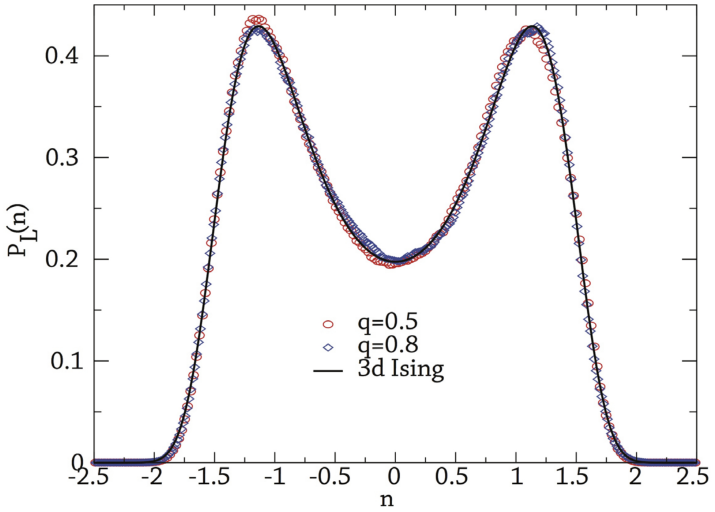

Figure 4.6. Critical-point distribution of the renormalized magnetization.

To identify the coexistence line, we proceed as follows. We fix z_p and determine the distribution of N_c and N_p for several values of z_c, either directly or by applying the standard reweighting method [110]. Then, the value of z_c corresponding to the binodal, $z_c^{\rm bin}(z_p)$, is obtained by applying the usual equal-area criterion: the areas below the two peaks characterizing the distributions of both N_c and N_p should be equal. Once $z_c^{\rm bin}(z_p)$ has been identified, the averages of N_c and N_p over the two peaks give the number of polymers and colloids in the two phases. Results are reported in Tables 4.4 and 4.5 for $q = 0.5$ and $q = 0.8$, respectively. They have been obtained using reasonably large cubic systems, of side $31.2\hat{R}_g$ and $23.1\hat{R}_g$ for $q = 0.5$ and $q = 0.8$, respectively. We expect size effects to be small, except close to the critical point.

To identify the critical point we use the method of Wilding [111], exploiting the fact that the transition is in the same universality class as the three-dimensional Ising transition. In the spin system the order parameter is the magnetization M, whose distribution at the critical point is known quite accurately [112]:

$$P(M) = K \exp\left[-\left(\frac{M^2}{M_0^2} - 1 \right)^2 \left(c + d\frac{M^2}{M_0^2} \right) \right], \tag{4.21}$$

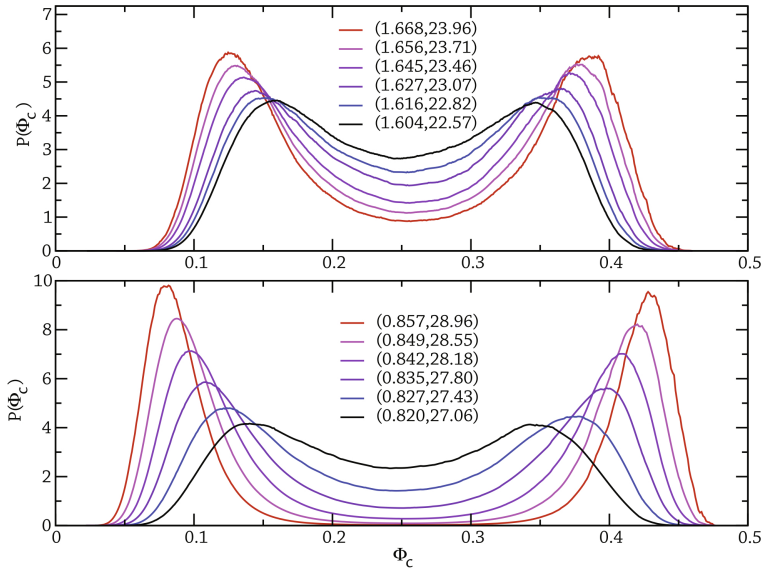

Figure 4.7. Distribution of Φ_c at the binodal: (top) $q = 0.8$, (bottom) $q = 0.5$. We report curves for different values of $\Phi_p^{(r)}$, $\beta\hat{\mu}_c$ (they are reported in the legend).

with $K = 0.486642$, $c = 0.776$, $d = 0.158$. The normalization constant M_0^2 can be determined by noting that $\langle M^2 \rangle = 0.777403 M_0^2$. For the mixture the order parameter analogous to the magnetization is a linear combination of N_c and N_p that can be defined as $n = A(N_c - aN_p + b)$. Using the distributions of N_c and N_p computed for each value of z_p and $z_c^{\rm bin}(z_p)$, we determine a and b by requiring $\langle n \rangle = 0$ and the distribution to be symmetric around $n = 0$. Finally, A is determined by requiring $\langle n^2 \rangle = 1$. Thus, for each value of the binodal we obtain a distribution function of the variable n, which is compared with the distribution in Eq. (4.21). The best matching occurs at a value z_p, which is then identified with the critical point. The distributions at the critical point are compared with the Ising one in Fig. 4.6, where we report the Ising distribution with $n = 1.13417 M/M_0$ and the distributions obtained using the data for $q = 0.5$ and 0.8. The agreement is very good. The mixing of N_c and N_p is very small. We obtain $a = 0.069$, and 0.148 for $q = 0.5$ and $q = 0.8$, respectively. This is further confirmed by the distributions of N_c shown in Fig. 4.7: they are already quite symmetric along the binodal.

For $q = 0.5$, the analysis of the data gives $z_{p,\rm crit} = 2.28$ (equivalently $\Phi_{p,\rm crit}^{(r)} = 0.823$), $\beta\hat{\mu}_{c,\rm crit} = 27.2$. Correspondingly, we have $\Phi_{c,\rm crit} = 0.25$ and $\Phi_{p,\rm crit} = 0.46$. We have not performed a detailed analysis of the finite-box error on these results, but it should be of the order of 0.01 on both critical volume fractions. For $q = 0.8$ the analysis of the data gives $z_{p,\rm crit} = 60.11$ (equivalently $\Phi_{p,\rm crit}^{(r)} = 1.621$) and $\beta\hat{\mu}_{c,\rm crit} = 22.9$. Correspondingly, we obtain $\Phi_{c,\rm crit} = 0.25$ and $\Phi_{p,\rm crit} = 0.89$.

Let us now compare the results with other estimates, see Fig. 4.8. For $q = 0.8$ it is evident that the binodal of the coarse-grained model is located at polymer densities that are too large. Consider, for instance, the location of the critical point. For $q = 1$, Ref. [104] estimates for the full-monomer model are $\Phi_{c,\rm crit} = 0.22$ and

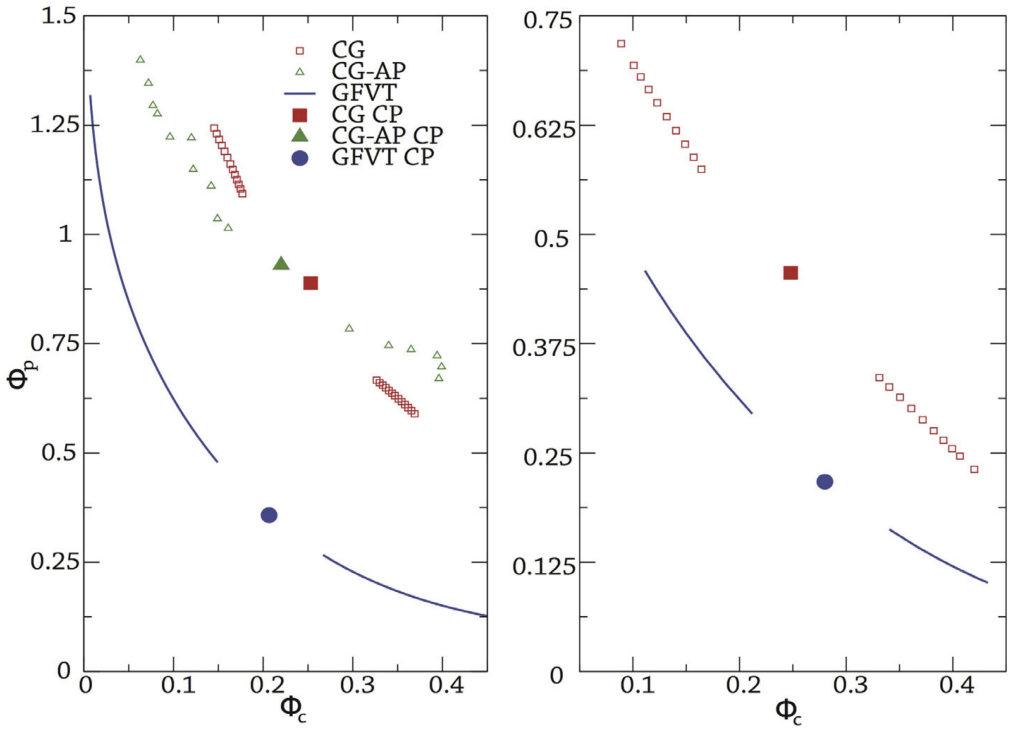

Figure 4.8. Fluid-fluid binodals for $q = 0.8$ (left) and $q = 0.5$ (right). We report the single-site (CG) result and the GFVT prediction. For $q = 0.8$ we also report the binodal computed using the simplified model of Ref. [62] (CG-AP). For each binodal we also report the corresponding critical point (CP).

$\Phi_{p,\mathrm{crit}} \approx 0.62$, hence the obtained estimate of $\Phi_{p,\mathrm{crit}} = 0.89$ is too large for $q = 0.8$. This is also confirmed by the GFVT results [104], that predict phase separation to occur at significantly smaller polymer densities. For instance, the critical point is predicted at $\Phi_{c,\mathrm{crit}} = 0.21$ and $\Phi_{p,\mathrm{crit}} = 0.36$ by GFVT [104]. It is interesting to note that the simplified model of Ref. [62] gives a binodal which is not very different from the one computed here. For instance, the critical point was located at $\Phi_{c,\mathrm{crit}} = 0.22$ and $\Phi_{p,\mathrm{crit}} = 0.93$ [62], quite close to the value obtained by using the exact CG model. For $q = 0.5$ the CG binodal is compatible with the upper bound provided by the full-monomer results with $q = 1$. However, comparison with the GFVT results (see Fig. 4.8) indicates that, most likely, the single-site CG model predicts phase separation at values of Φ_p that are too large also for this value of q.

4.3.2 Integral equation methods

In this section we will investigate thermodynamic and structural properties of colloid-polymer mixtures, for $q = 0.5, 0.8$ and 1, by means of the integral equation methods introduced in Sec. 1.3. For simple fluids these methods cannot compete nowadays with Monte Carlo and molecular-dynamics simulations. Nonetheless, they have the advantage of providing reasonably accurate estimates of thermodynamic quantities with a very limited effort, and they are therefore a very valuable tool when the

system under investigation depends on many parameters, for instance in the case of multi-component systems. Moreover, they are still very useful for the analysis of systems for which atomistic simulations are particularly slow, for instance in glassy systems; see, *e.g.*, Refs. [113–116].

Liquid-state integral equations have also been extensively used to compute fluid-fluid phase-coexistence lines. In the density region in which the system demixes, integral equations may not converge, or may converge to physically unacceptable solutions. The relation between the boundary of this nonconvergence region (we will call it *termination line*) and the binodal and the spinodal curves characterizing the two-phase unstable region has been the subject of many studies, see, e.g., Refs. [117–120]. In particular, it has been shown that, except in the case of very simple approximations, thermodynamic quantities do not show any particular divergence on the termination line, hence it cannot be taken as an approximate estimate of the spinodal line. However, it is usually assumed that it is somewhat close to the line where phase separation occurs.

By computing these termination lines in the case of coarse-grained, single-blob models for colloid-polymer mixtures, and comparing them to the Monte Carlo phase diagram presented in Sec. 4.3.1, we will be able to elucidate whether these non-convergence lines (when present) are truly connected to an instability of the homogeneous phase. Moreover, although we take specific pair potentials appropriate to describe, in a CG SB fashion, a binary system of hard-sphere colloids and long polymers under good-solvent conditions [46], the conclusions should apply to a general class of soft-matter systems that can be modeled as mixtures of soft and hard spheres, interacting via short-range potentials which present a strongly non-additive nature. In the analysis, we employ the hypernetted-chain (HNC) closure (1.47), which is known to be accurate for "soft" interactions [4], the Percus-Yevick (PY) (1.50), the Rogers-Young (RY) (1.57), and the reference-HNC (RHNC) closures (1.61) [4, 12, 14, 15]. Since for hard spheres the PY closure relation (1.50) is more accurate than the HNC closure, we consider a hybrid closure (HNC/PY in the text), which uses the HNC closure (1.47) for polymer-polymer and polymer-colloid correlations and the PY closure (1.50) for the colloid-colloid correlations. For small polymer densities, we will also be able to compute by Monte Carlo simulations the bridge functions—quantities that have an intrinsic interest in liquid-state theories—which will then be compared with the approximate ones considered in the different approaches.

In Sec. 4.3.1, we showed that density-dependent SB models, on one hand, poorly reproduce the properties of the original system, also in the homogeneous phase. On the other hand, criticalities arise as a consequence of the state-dependence of the interaction itself. Hence, we will not consider them in the analysis, considering only zero-density, accurate scaling limit potentials. The colloid-colloid potential is the usual hard-spheres potential, the polymer-polymer potential is reported in Eq. (4.5), and the colloid-polymer potential is reported in Eq. (4.15).

Table 4.6. Estimates of the structure factors $S_{\alpha\beta}(k=0)$ (1.38), of the concentration factor $S_c(k)$ (1.40), of the virial pressure $P^{(\mathrm{vir})}$ (1.41), and of the compressibility κ_T (1.29) computed using Eq. (1.56) for $\Phi_c = 0.3$, $\Phi_p = 0.09$, $q = 0.5$, and for the HNC closure. We report results for several values of N and Δr.

	$N = 32768$			$N = 65536$			
$\Delta r/\hat{R}_g =$	0.001	0.002	0.004	0.0005	0.001	0.002	0.004
$\beta P^{(\mathrm{vir})} R_c^3$	0.956	0.955	0.953	0.956	0.956	0.955	0.953
$\beta R_c^3/\kappa_T$	1.763	1.762	1.756	1.764	1.763	1.761	1.756
$S_{pp}(0)$	3.399	3.436	3.560	3.384	3.399	3.436	3.560
$S_{cp}(0)$	−0.792	−0.801	−0.830	−0.788	−0.792	−0.801	−0.830
$S_{cc}(0)$	0.263	0.264	0.271	0.261	0.262	0.264	0.271
$S_c(0)$	0.396	0.400	0.414	0.393	0.396	0.400	0.414

4.3.2.1 Technical details

In the integral-equation approach, pair and direct correlation functions are discretized on N regularly spaced points, $r_n = n\Delta r$. Moreover, all functions are assumed to be zero at a cut-off distance $R_{\max} = N\Delta r$. Typically, we take $\Delta r = 0.001\hat{R}_g$ and $N = 32768$ or 65536. The grid is extremely fine and and the box reasonably large, to guarantee that results are stable with respect to changes of the parameters Δr and N. In Table 4.6 we report several thermodynamic quantities as a function of $\Delta r/\hat{R}_g$ and N for the HNC closure at $\Phi_c = 0.3$, $\Phi_p = 0.09$ for $q = 0.5$, a state point that, as we will discuss, is very close to the termination line. Estimates do not change as N changes, indicating that the cut-off distance is large enough. The step size is more crucial, but $\Delta r/\hat{R}_g = 0.001$ should be accurate enough. In the paper, most of the analysis use $\Delta r/\hat{R}_g = 0.001$ and $N = 32768$. In a few cases, we have checked the results, by changing Δr and/or N by a factor of 2. The independence of the results on the chosen parameters allows us to exclude that the observed behavior is due either to a too small cut-off distance or to a too coarse discretization of the correlation functions.

We use the standard Picard iterative method [4], which converges quite fast, except close to the termination line. We improve convergence by considering a mixing parameter α. If $c_{\mathrm{ini}}^{(n)}(r)$ and $c_{\mathrm{end}}^{(n)}(r)$ indicate the direct correlation functions at the beginning and at the end of the n-th step of the iterative procedure, respectively, we set $c_{\mathrm{ini}}^{(n+1)}(r) = (1-\alpha)c_{\mathrm{ini}}^{(n)}(r) + \alpha c_{\mathrm{end}}^{(n)}(r)$. Far from the termination line, α is not a relevant parameter. However, close to the termination line, convergence is only obtained if α is small. In some cases, we took $\alpha \sim 10^{-2}$.

4.3.2.2 Termination lines

In order to determine the termination line, we work as follows. We fix the colloid volume fraction $\Phi_c = 4\pi R_c^3 N_c/3V$, (where N_c is the number of colloids present in the box of volume V) and solve the equations for a small value of the polymer density. Typically, if $\Phi_p = 4\pi\hat{R}_g^3 N_p/3V$, we start at $\Phi_p^{(0)} \approx 0.005$ for $\Phi_c \gtrsim 0.2$ and at

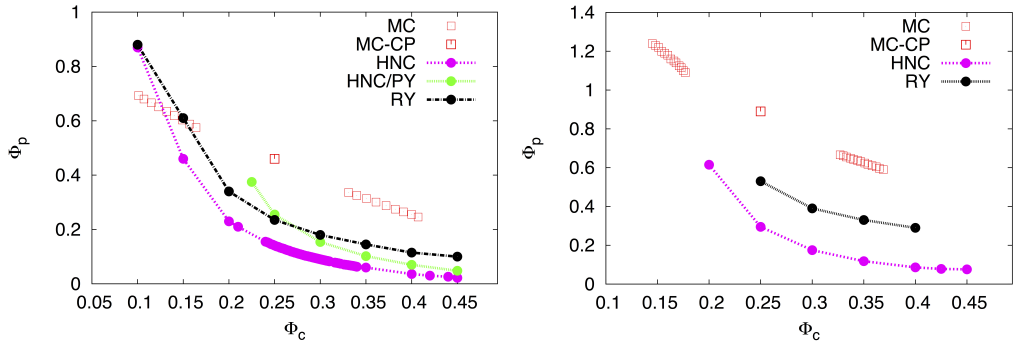

Figure 4.9. Phase diagram for $q = 0.5$ (left) and $q = 0.8$ (right). We report the binodals obtained by Monte Carlo simulations (MC), the corresponding critical point (MC-CP), and the termination lines for each of the closures. We have also computed (not reported in figure) the termination point for the RHNC closure, for $q = 0.5$ and $\Phi_c = 0.3$: $\Phi_p = 0.104$.

$\Phi_p^{(0)} \approx 0.01$ for smaller colloid volume fractions. Then, we increase Φ_p by steps $\Delta\Phi_p$: we successively solve the equations for $\Phi_p^{(n)} = \Phi_p^{(0)} + n\Delta\Phi_p$, starting the iterations for the n-th density from the solution obtained at $\Phi_p^{(n-1)}$. For $q = 1$ we are able to increase Φ_p at will. On the other hand, for $q = 0.8$ (in all cases except for the HNC/PY closure) and for $q = 0.5$ we find termination lines, see Fig. 4.9. Indeed, if $\Delta\Phi_p$ is large or the mixing parameter in the Picard iterations is of order 1, we end up at a density $\Phi_p^{(M)}$ where the iterations no longer converge. In this case, we consider again the solution of the equations obtained at $\Phi_p^{(M-1)}$, but now we significantly decrease $\Delta\Phi_p$ and the mixing parameter (in some cases we take a parameter as small as 0.01). If we increase again Φ_p, we now observe that the Picard iterations converge. However, at a very specific value of Φ_p the stable solution is no longer physical, as the concentration structure factor $S_c(k)$ defined in Eq. (1.40) becomes discontinuous at a finite value of k. We identify the termination line as the smallest polymer density at which $S_c(k)$ [the same occurs for all structure factors $S_{\alpha\beta}(k)$] develops a discontinuity. It is interesting to observe that while the position of the termination line is independent of the protocol used to increment Φ_p, the singular solution depends on $\Delta\Phi_p$. As an example, in Fig. 4.10 we show the estimates of $S_c(k = 0)$ for $q = 0.5$ and $\Phi_c = 0.3$ for three different values of $\Delta\Phi_p$. Incrementing Φ_p, at the termination line $\Phi_p \approx 0.0903$ we always observe a jump in $S_c(0)$ to a new value. However, such value depends on $\Delta\Phi_p$. If we further increase Φ_p beyond the termination line and then decrease again Φ_p, the unphysical solution appears to be stable: The structure factor changes smoothly with Φ_p. Moreover, once Φ_p is again below the termination-line value, if we use a small mixing parameter, we always stay with the unphysical solution. For $q = 1$ we have been able to increase Φ_p up to 2.5 for all values of $\Phi_c \leq 0.40$: We always find a regular solution of the integral equations. This is not surprising, as, for this value of q, the Monte Carlo simulation results of Section 4.3.1 indicate that the fluid-fluid binodal either does not exist or is located at quite large values of the polymer volume fraction. For $q = 0.8$ integral equations do not show any singular behavior if the HNC/PY closure is used. These

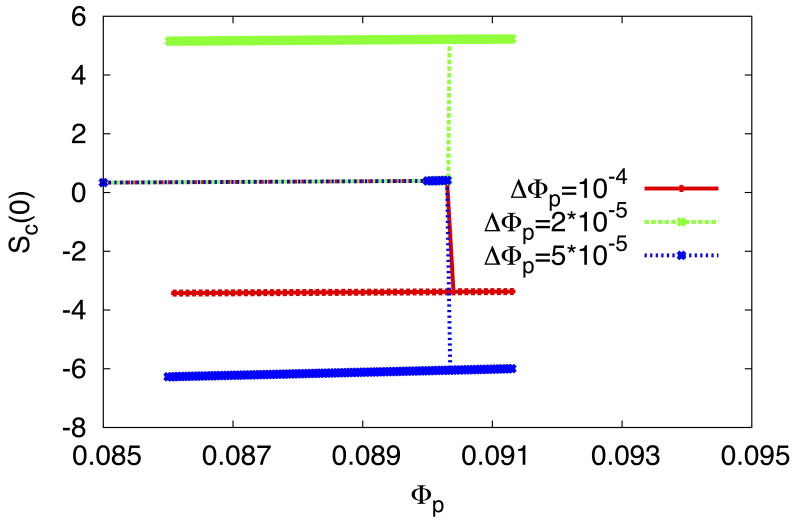

Figure 4.10. Estimate of $S_c(k=0)$ for $q=0.5$ and $\Phi_c=0.3$. Results for three different $\Delta\Phi_p$ and the HNC closure. We start from the values of $c_{\alpha\beta}(r)$ and $h_{\alpha\beta}(r)$ for $\Phi_p=0.9$ and increase Φ_p by steps $\Delta\Phi_p$ up to $\Phi_p=0.0915$, then we decrease Φ_p with the same schedule up to $\Phi_p=0.086$. The termination line occurs for $\Phi_p=0.0903$.

results are therefore not even qualitatively correct, as Monte Carlo simulations show demixing for this value of q. On the other hand, a termination line is observed if we use the HNC or the RY closures, see Fig. 4.9. Note, however, that the termination lines are quite far from the correct binodal, indicating that the results are only qualitatively correct. For $q=0.5$ all closures predict a termination line, although, also in this case, the results are quite different from the Monte Carlo predictions, see Fig. 4.9. We have also considered the RHNC closure. Since this approach is quite complex, we have only analyzed one case: $q=0.5$ and $\Phi_c=0.3$. For $\Phi_p\approx 0$, the effective radius R_p is equal to $0.837\hat{R}_g$. The polymer effective radius was computed by means of the Lado criterion defined in Eq. (1.62), for a fixed colloidal radius R_c. This is a completely reasonable value, indicating that polymers are effectively equivalent to hard spheres of radius approximately equal to $\hat{R}_g$. As Φ_p increases, the effective radius R_p decreases quite rapidly: for $\Phi_p=0.1$ we find $R_p=0.60\hat{R}_g$. Again, this is consistent with intuition, as we expect the polymers to shrink as Φ_p increases. Unfortunately, we are not able to go much beyond $\Phi_p=0.1$, as the RHNC equation ceases to converge at $\Phi_p=0.104$. Hence, this approach represents only a modest improvement with respect to the HNC approach (the HNC termination line occurs at $\Phi_p\approx 0.090$).

In conclusion, our results show that none of the closures we considered provides accurate results for the demixing transition, although the RY closure performs better than the HNC one, which stops converging at very small values of Φ_p in the colloid-liquid phase. In all cases the termination line is significantly below the correct binodal, especially in the colloid-liquid phase $\Phi_c \gtrsim 0.25$. Clearly, the convergence to an unphysical solution is not directly related to singularities in the thermodynamic behavior of the model. Therefore, the termination line provides a very poor approximation of the phase-separation line.

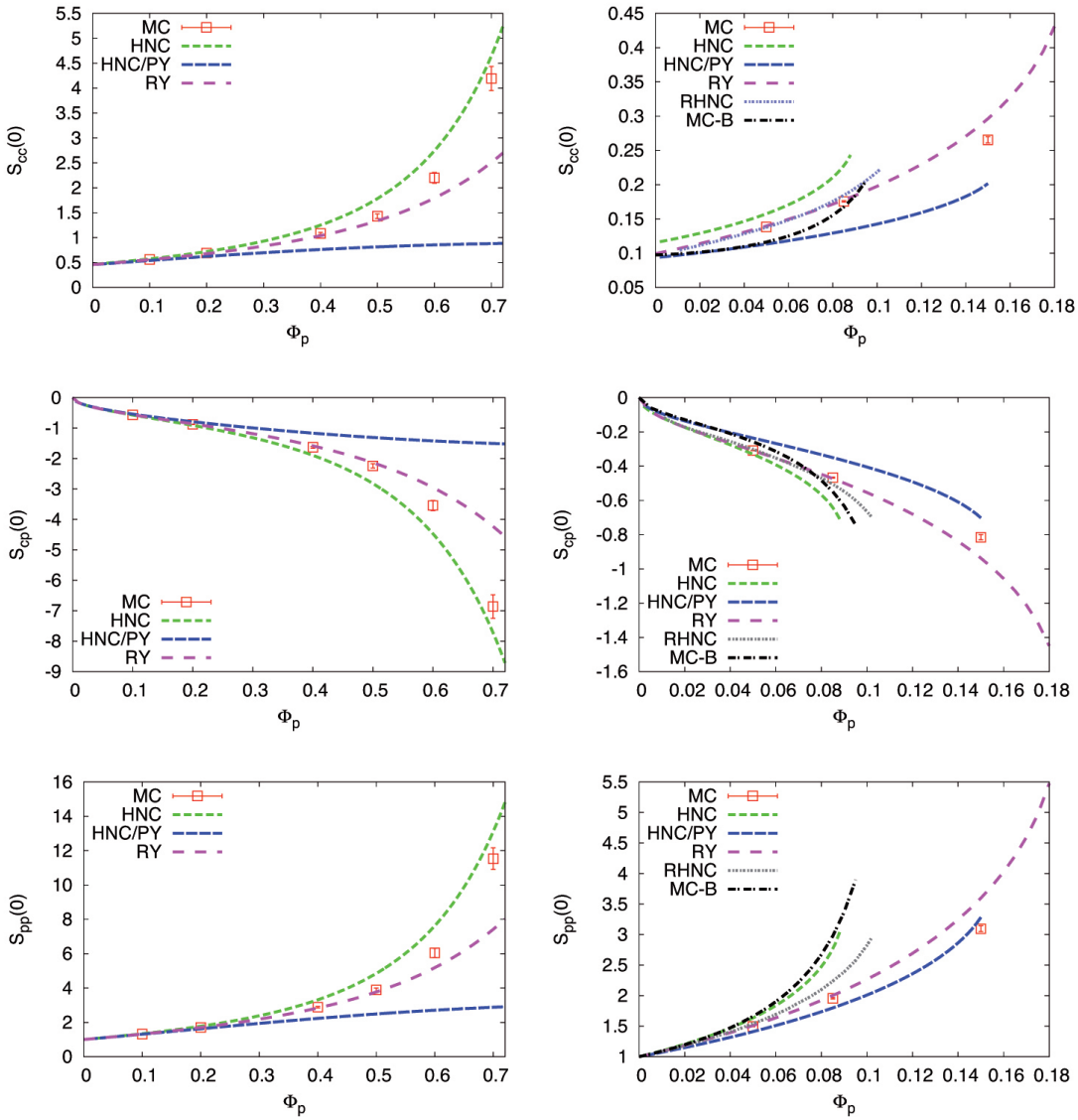

Figure 4.11. Structure factors $S_{\alpha\beta}(k=0)$ for $q=0.5$ and $\Phi_c=0.1$ (left) and $\Phi_c=0.3$ (right). Lines are the results obtained by using the HNC, HNC/PY, and RY closures. Symbols are Monte Carlo data. For $\Phi_c=0.3$ we also include results for the RHNC closure and results obtained by using the zero-polymer-density Monte Carlo bridge functions (MC-B), as discussed in Sec. 4.3.2.3.

4.3.2.3 Structural behavior in the homogeneous phase

We wish now to compare the integral-equation predictions with the Monte Carlo ones in the homogeneous phase. We consider the case $q=0.5$, in which a termination line occurs for all considered closure relations. We begin by analyzing the structure factors $S_{\alpha\beta}(k=0)$, which are directly related to thermodynamics by the compressibility equations [4, 5]. In Fig. 4.11 we report the corresponding estimates for two values

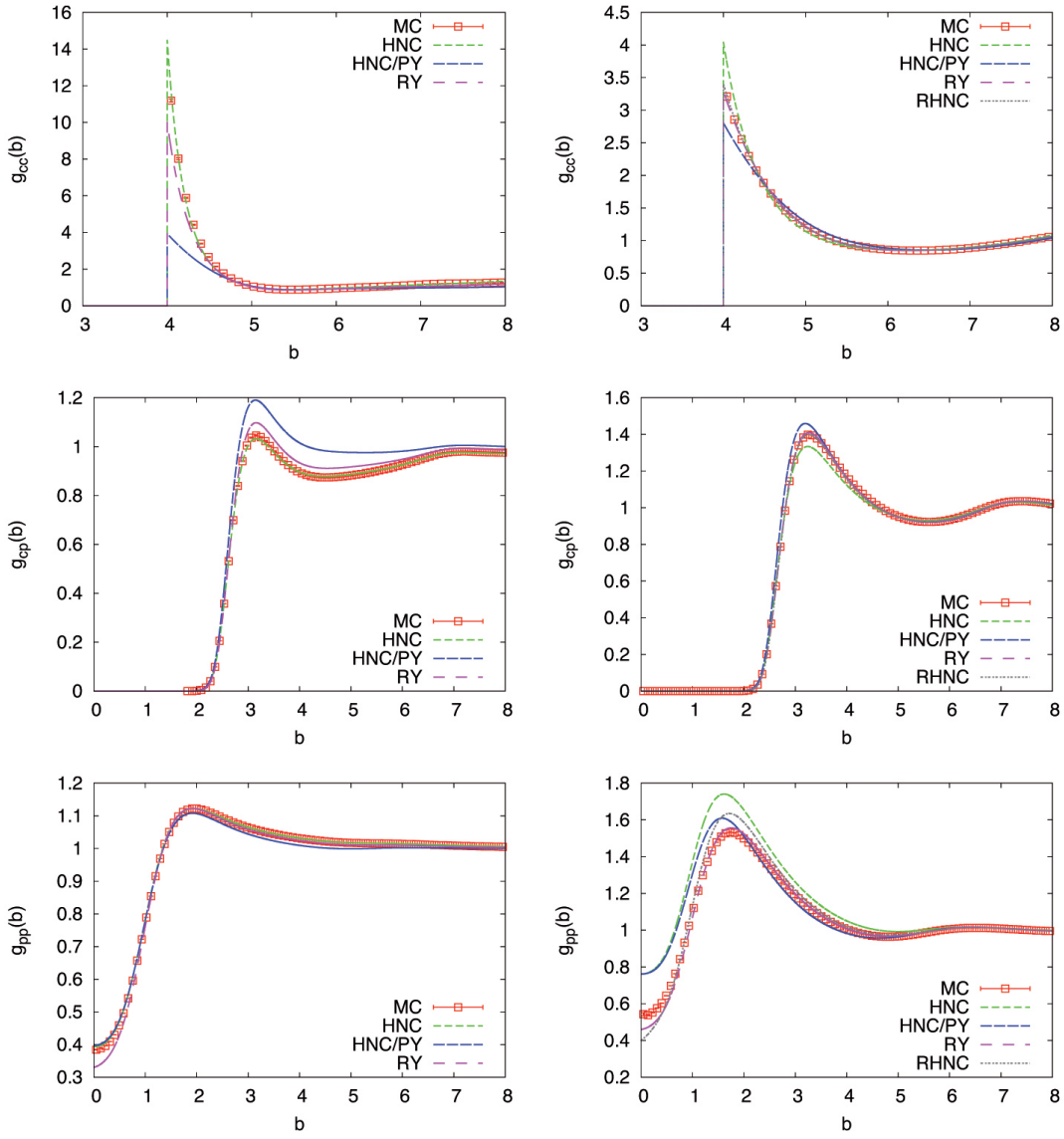

Figure 4.12. Pair correlation functions $g_{\alpha\beta}(r)$ as a function of $b = r/\hat{R}_g$ for $q = 0.5$ at two different state points: $\Phi_c = 0.1$, $\Phi_p = 0.70$ (left) and $\Phi_c = 0.3$, $\Phi_p = 0.085$ (right). Lines are the results obtained by using the HNC, HNC/PY, RY, RHNC closures. Symbols are Monte Carlo data.

of Φ_c, $\Phi_c = 0.1$ and 0.3, that lie on opposite sides with respect to the critical point located at $\Phi_{c,\mathrm{crit}} = 0.25$, $\Phi_{p,\mathrm{crit}} = 0.46$, as estimated by Monte Carlo simulations. For $\Phi_c = 0.1$ the HNC/PY closure significantly underestimates the structure factors. Clearly, $|S_{\alpha\beta}(0)|$ increases too slowly as Φ_p increases, explaining why convergence is observed at least up to $\Phi_p = 2.5$. The HNC and RY estimates increase faster. The latter are more accurate than the HNC ones for small densities, but they significantly underestimate $|S_{\alpha\beta}(0)|$ close to the binodal, which is located at $\Phi_p \approx 0.70$. The fact that the RY results are less accurate than the HNC ones near the binodal may

be surprising, as the RY closure is a generalization of the HNC closure. It simply indicates that the requirement of thermodynamic consistency does not necessarily lead to more accurate results. Note that both HNC and RY integral equations also converge for some values of Φ_p in the metastable region beyond the binodal, see Fig. 4.9. In this domain the structure factors $S_{\alpha\beta}(0)$ are quite large [on the binodal, Monte Carlo simulations give $S_{pp}(0) = 11.5(6)$, $S_{cp}(0) = -6.7(4)$, $S_{cc}(0) = 4.2(2)$]. Therefore, even though we do not observe an exact divergence of $S_{\alpha\beta}(k = 0)$, for this value of Φ_c we can take the termination line as a good estimate of the spinodal line. For $\Phi_c = 0.3$ the behavior is quite different and the termination lines occur at values of Φ_p significantly smaller than that of the binodal. Moreover, integral equations stop converging when the structure factors $|S_{\alpha\beta}(0)|$ are relatively small, at least if compared with the values they assume on the binodal at $\Phi_c = 0.1$. For instance, the HNC and HNC/PY equations both cease to converge when $S_{pp}(0) \approx 3$, while $S_{pp}(0) \approx 5$ on the RY termination line. Comparing the integral-equation estimates with the Monte Carlo results, we see that the RY closure is here the most accurate, in agreement with previous studies [121, 122], although it fails to converge well before the binodal. As for the RHNC, the estimates of $S_{cc}(0)$ and $S_{cp}(0)$ are consistent with the RY ones and the Monte Carlo data up to $\Phi_p \approx 0.08$. On the other hand, the RHNC estimates of $S_{pp}(0)$ increase too fast for $\Phi_p \gtrsim 0.04$, looking similar to the HNC estimates. Also in this case the termination line occurs for $S_{pp}(0) \approx 3$.

As a second test let us compare the pair distribution functions. For $\Phi_c = 0.1$ and $\Phi_p = 0.7$, i.e., on the binodal, see Fig. 4.12, all closures reasonably reproduce the polymer-polymer distribution function. Deviations are instead observed for the polymer-colloid and especially for the colloid-colloid distribution function. The largest deviations are observed for the HNC/PY closure. For instance, the colloid-colloid correlation is significantly underestimated at contact. While an extrapolation of the Monte Carlo data predicts $g_{cc}(2R_c) \approx$ 13-14, we estimate $g_{cc}(2R_c) \approx 4$ by using the HNC/PY closure. The RY closure performs better, although it is also unable to predict the correct value of $g_{cc}(r)$ at contact and slightly overestimates $g_{cp}(r)$ at the first peak. The HNC closure is the most accurate one for this value of Φ_c, as the HNC curves fall on top of the Monte Carlo data.
At $\Phi_c = 0.3$ the behavior is quite different, see Fig. 4.12. For $\Phi_p = 0.085$, close to the HNC termination line, HNC results are not accurate, especially for $g_{pp}(r)$, which is significantly overestimated for $r \lesssim 2\hat{R}_g$. The value of $g_{cc}(r)$ at contact is also significantly overestimated. The HNC/PY closure gives results that are only marginally better than the HNC ones, while the RY estimates are in full agreement with the Monte Carlo data. The RHNC estimates of $g_{cc}(r)$ and $g_{cp}(r)$ are in agreement with the data, but this is not the case for $g_{pp}(r)$, which is overestimated for $1 \lesssim r/\hat{R}_g \lesssim 2$, the region in which the correlation function shows the first peak. At $\Phi_p = 0.15$ we only have RY data, as integral equations no longer converge for the other closures. The results are reported in Fig. 4.13. Pair correlations $g_{cc}(r)$ and $g_{cp}(r)$ are well reproduced, while relatively small deviations are observed for $g_{pp}(r)$. Apparently, RY estimates are relatively accurate even close to the corresponding termination line, located at $\Phi_p \approx 0.18$.

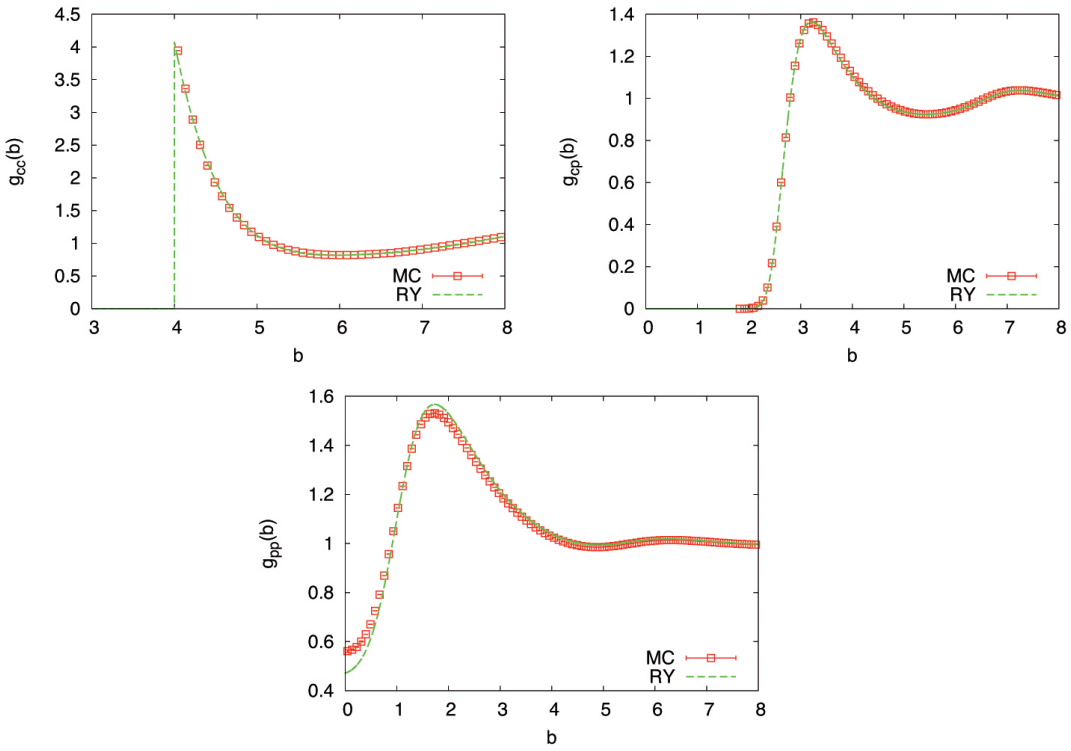

Figure 4.13. Pair correlation functions $g_{\alpha\beta}(r)$ as a function of $b = r/\hat{R}_g$ for $q = 0.5$ at $\Phi_c = 0.3$, $\Phi_p = 0.15$. Lines are the results obtained by using the RY closure. Symbols are Monte Carlo data.

4.3.2.4 Bridge functions at zero polymer density

The failure of integral-equation methods to reproduce the thermodynamics for $\Phi_c \gtrsim 0.2$ and to provide a reasonably accurate estimate of the boundary of the two-phase region clearly indicates that none of the closures we used is appropriate for the problem at hand. To understand better the origin of the discrepancies, we now compare the bridge functions used in the integral-equation approach with the exact estimates obtained numerically, by using the Monte Carlo results for the pair correlation functions. For this purpose we should compute $g_{\alpha\beta}(r)$ accurately on large boxes. It turns out that this is feasible only for $\Phi_p \to 0$, the case we will study below. The input numerical quantities are $g_{cc}(r)$ (we use the accurate expressions that can be obtained as discussed in Refs. [15, 20]), $g_{cp}(r)$, and $g_{pp}(r)$. To determine the last two quantities, we perform simulations for different values of Φ_p on systems of linear size $L/\hat{R}_g \approx 32$, 24 for $q = 0.5$ and 1, and perform an extrapolation to $\Phi_p \to 0$. Then, we determine the direct correlation functions by inverting the OZ

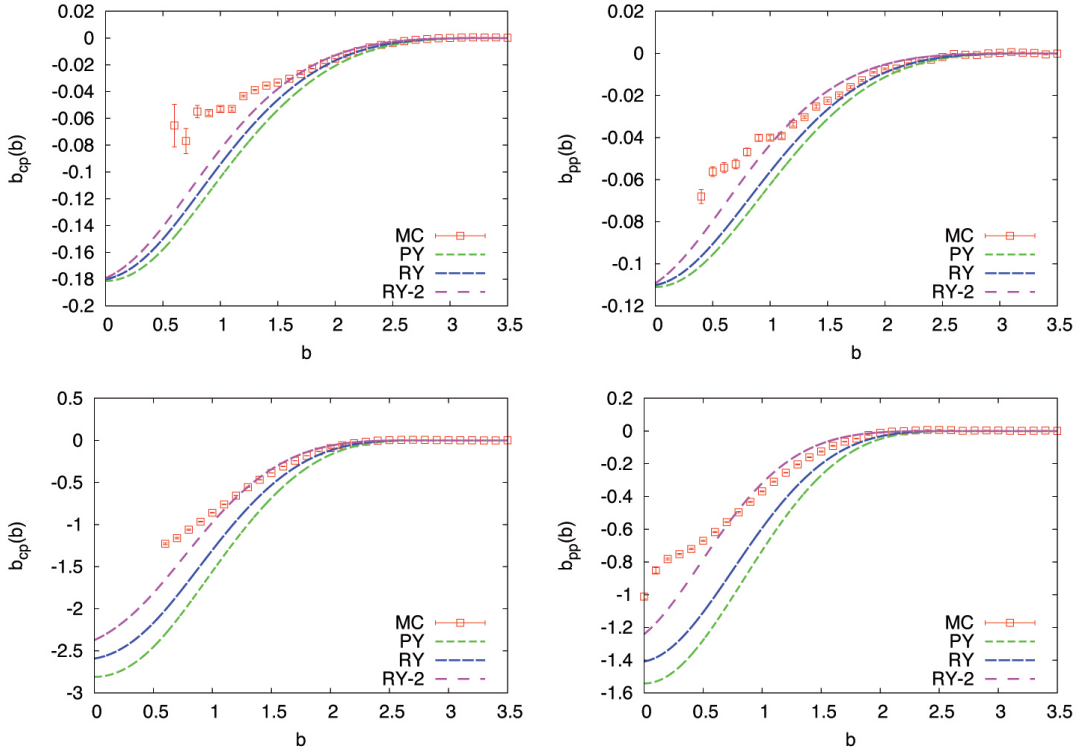

Figure 4.14. Bridge functions for $q = 1$ as a function of $b = r/\hat{R}_g$: on the left we report $b_{cp}(r)$, on the right $b_{pp}(r)$. Top: $\Phi_c = 0.1$; bottom: $\Phi_c = 0.3$. We report the Monte Carlo estimates (MC) as well as those obtained by using the different closures. RY-2 labels the results obtained by using the two-parameter RY closure discussed in the text.

relations, which, for $\Phi_p \to 0$, simplify to

$$\begin{aligned} \hat{c}_{cc}(k) &= \frac{\hat{h}_{cc}(k)}{1 + \rho_c \hat{h}_{cc}(k)}, \\ \hat{c}_{cp}(k) &= \hat{h}_{cp}(k) - \rho_c \hat{c}_{cc}(k) \hat{h}_{cp}(k), \\ \hat{c}_{pp}(k) &= \hat{h}_{pp}(k) - \rho_c \hat{c}_{cp}(k) \hat{h}_{cp}(k). \end{aligned} \tag{4.22}$$

Finally, we define the bridge functions

$$b_{\alpha\beta}(r) = \ln \left[g_{\alpha\beta}(r) e^{\beta V_{\alpha\beta}(r)} \right] + c_{\alpha\beta}(r) - h_{\alpha\beta}(r). \tag{4.23}$$

We will focus on the polymer-polymer and colloid-polymer functions, as $b_{cc}(r)$ depends only on the hard-sphere fluid, a case that has already been extensively discussed in the literature. Note that $\beta V_{cp}(r)$ is large for $r \lesssim R_c$, hence, we are not able to obtain reliable estimates of $b_{cp}(r)$ for $r \lesssim R_c$. For the HNC closure, we have $b_{cp}(r) = b_{pp}(r) = 0$. In all other cases, the bridge functions are obtained from Eq. (4.23), using the correlation functions obtained by means of the different closures. For the values of r for which $V_{cp}(r)$ is large, it is convenient to express $g_{cp}(r) e^{\beta V_{cp}(r)}$ in terms of $h_{cp}(r) - c_{cp}(r)$ using the closure relation. This trick allows

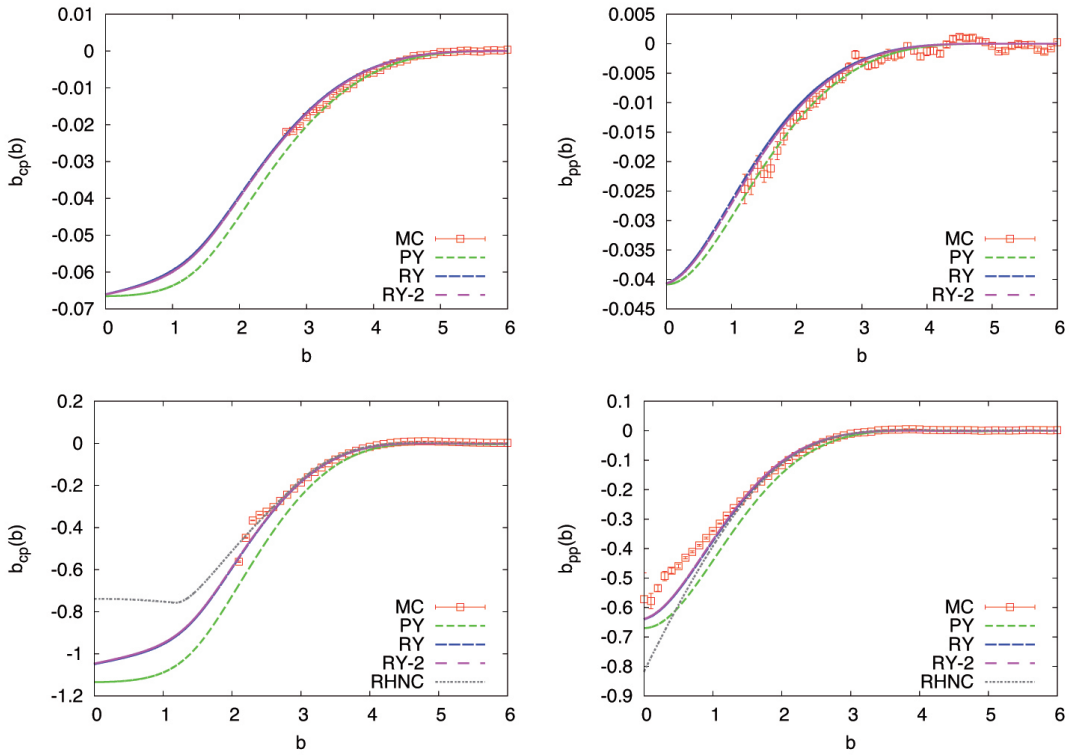

Figure 4.15. Bridge function for $q = 0.5$ as a function of $b = r/\hat{R}_g$: on the left we report $b_{cp}(r)$, on the right $b_{pp}(r)$. Top: $\Phi_c = 0.1$;bottom: $\Phi_c = 0.3$. We report the Monte Carlo estimates (MC) as well as those obtained by using the different closures. RY-2 labels the results obtained by using the two-parameter RY closure discussed in the text.

us to compute the bridge functions $b_{cp}(r)$ inside the core region $r \lesssim R_c$, although here they cannot be compared with the Monte Carlo results. In this section we do not consider the HNC/PY, as it has the same bridge functions of the HNC closure. We will instead discuss the full PY closure, in which Eq. (1.50) is used for all correlations. The bridge functions for $\Phi_c = 0.1$ and 0.3 are reported in Figs. 4.14 and 4.15 for $q = 1$ and 0.5, respectively. For $\Phi_c = 0.1$ the bridge functions are tiny, explaining why the HNC closure works reasonably well. The PY and RY closures are essentially equivalent. Small deviations are evident for $q = 1$ and $r \lesssim 2\hat{R}_g$ — but in this range data become increasingly less accurate — while for $q = 0.5$ no deviations are observed in the region in which data appear to be reliable. As Φ_c increases, the bridge functions become increasingly negative for small values of r. For $q = 1$ and $\Phi_c = 0.3$, none of the closures appears to be accurate, although the RY closure is marginally better, and large deviations are observed for $r \lesssim 2\hat{R}_g$. For $q = 0.5$ the RY closure reproduces well $b_{cp}(r)$ up to $r \approx 2\hat{R}_g$—the region outside the colloid core. On the other hand, deviations are clearly observed for $b_{pp}(r)$ when $r \lesssim \hat{R}_g$. The PY closure is clearly worse, as it underestimates both bridge functions for $r \lesssim 2\hat{R}_g$-$3\hat{R}_g$. The RY optimization at $\Phi_p = 0$ uses only the colloid-colloid correlations. Indeed, in

this limit the consistency condition between the compressibilities (1.55) and (1.56) is

$$\left(\frac{\partial\beta P^{(\mathrm{vir})}}{\partial\rho_c}\right)_{\rho_p=0} = 1 - \rho_c\hat{c}_{cc}(0). \tag{4.24}$$

Therefore, one might think that the relatively poor agreement for the polymer-polymer correlations for small values of r is related to the fact that the procedure does not take into account polymer properties. We have thus considered a two-parameter optimization. We set $\chi_{pp} = \chi_1/\hat{R}_g$ and $\chi_{cc} = \chi_2/R_c$ as free parameters, while χ_{pc} is, somewhat arbitrarily, set equal to $(\chi_1 + \chi_2)/(\hat{R}_g + R_c)$. As consistency conditions, we consider Eq. (4.24) and [5]

$$\left(\frac{\partial\beta P^{(\mathrm{vir})}}{\partial\rho_p}\right)_{\rho_c,\rho_p=0} = 1 - \rho_c\hat{c}_{cp}(0), \tag{4.25}$$

which involves polymer-colloid correlations. In Figs. 4.14 and 4.15, we also report the bridge functions for this case (they are labelled RY-2). For $q = 1$ we observe a significant improvement with respect to the one-parameter RY case, although significant differences with Monte Carlo data are still present for $r/\hat{R}_g \lesssim 1$. For $q = 0.5$ instead, the two different RY closures yield equivalent estimates.

As a final case, we consider the RHNC closure, which relies on the assumption that the bridge functions can be accurately parametrized by those of a binary additive hard-sphere mixture. To verify if this is the case, we consider $q = 0.5$ and $\Phi_c = 0.3$, and compute

$$\Delta(R_p) = \int \left| b_{pp}^{MC}(r) - b_{pp}^{HS}(r, R_p) \right| r^2 dr, \tag{4.26}$$

for different values of the effective polymer radius R_p. The optimal value (minimal Δ) is obtained for $R_p = 0.842\hat{R}_g$. We can compare this result with that obtained by using the Lado criterion [15, 16]. For $\Phi_p = 0$, Eq. (1.62) is satisfied as we use the very accurate hard-sphere correlation function of Ref. [21]. To determine R_p one needs to consider the linear term in the polymer density, i.e., the equation

$$\int r^2 [h_{cp}(r) - h_{cp}^{HS}(r; R_p, R_c)] \frac{\partial b_{cp}^{HS}(r; R_p, R_c)}{\partial R_p} = 0. \tag{4.27}$$

Alternatively, one can determine R_p for several small values of Φ_p, performing an extrapolation to $\Phi_p \to 0$ at the end. The first method gives $R_p = 0.837\hat{R}_g$, while the second one gives $R_p = 0.828\hat{R}_g$. Both results are very close to the estimate $R_p = 0.842\hat{R}_g$ obtained by a direct matching of the bridge functions. This confirms that the Lado criterion provides the bridge functions that are the best approximations of the exact ones. The resulting bridge functions are reported in Fig. 4.15. The RHNC estimate of $b_{cp}(r)$ is in agreement with the Monte Carlo function for $r \gtrsim 2\hat{R}_g$. As for $b_{pp}(r)$, the RHNC estimate agrees with the Monte Carlo one for $r \gtrsim \hat{R}_g$. At smaller distances, instead, the RHNC bridge function underestimates the correct one and appears to provide a worse approximation than the RY closure.

This analysis for $\Phi_p = 0$ further confirms the results obtained in Sec. 4.3.2.3. For $\Phi_c = 0.1$, the bridge functions are quantitatively small, confirming the accuracy of the HNC approximation. On the other hand, for $\Phi_c = 0.3$, the RY closure

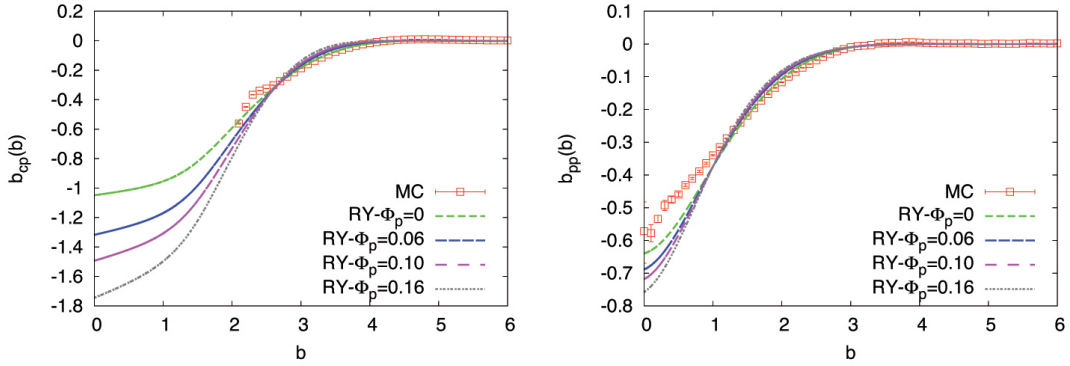

Figure 4.16. Bridge functions for $\Phi_c = 0.3$ and $q = 0.5$ as a function of $b = r/\hat{R}_g$. We report the zero-density function obtained by Monte Carlo simulations (MC), and the RY functions for different values of the polymer volume fraction Φ_p.

is the one that provides the best approximation, while the HNC closure is the least accurate one as it cannot reproduce the small-distance behavior of the bridge functions. Note that, while $b_{cp}(r)$ is correctly reproduced in the relevant region $r \gtrsim R_c$, the polymer-polymer bridge function is always poorly reproduced for $r \lesssim \hat{R}_g$. This discrepancy gives rise to similar discrepancies in the correlation functions, as discussed in Sec. 4.3.2.3.

4.3.2.5 Integral equations with Monte Carlo bridge functions

As a final test we decided to determine the solutions of the integral equations by using the zero-density Monte Carlo bridge functions computed in Sec. 4.3.2.4. In other words, we consider the closure relation (1.46), setting for all values of Φ_p, $b_{pp}(r;\Phi_c,\Phi_p) = b_{pp}^{MC}(r;\Phi_c,\Phi_p=0)$, $b_{cp}(r;\Phi_c,\Phi_p) = b_{cp}^{MC}(r;\Phi_c,\Phi_p=0)$, and $b_{cc}(r;\Phi_c,\Phi_p) = b_{cc}^{HS}(r;\Phi_c)$, where the last quantity is the bridge function of a pure hard-sphere system [18]. This approximation is exact for $\Phi_p = 0$ and one may wonder whether it provides a reasonable approximation also for $\Phi_p > 0$. We have tested the approach for $q = 0.5$ and $\Phi_c = 0.3$. The results for the structure factors, reported in Fig. 4.11 (they are labelled MC-B), show that this approach is only marginally better than that based on the HNC closure. Also the termination point, $\Phi_p = 0.11$, is only slighly above the HNC one, $\Phi_p = 0.090$.
To clarify the origin of the discrepancies, we have determined the RY bridge functions for several values of Φ_p. As the RY estimates reasonably agree with the Monte Carlo data up to the termination line, we take them as estimates of the exact density-dependent $b_{\alpha\beta}(r;\Phi_c,\Phi_p)$. As one can see from the results shown in Fig. 4.16, the density dependence of the bridge functions is not large (for $b_{cp}(r)$ the relevant region is $b = r/\hat{R}_g \gtrsim 2$). Yet, this relatively small difference is the cause of the different results obtained. In practice, this simple exercise shows that results are extremely sensitive to the specific form of the bridge functions in the colloid-liquid phase $\Phi_c \gtrsim 0.25$. Hence, accurate results can only be obtained by using accurate bridge functions, that none of the methods we investigated is able to provide.

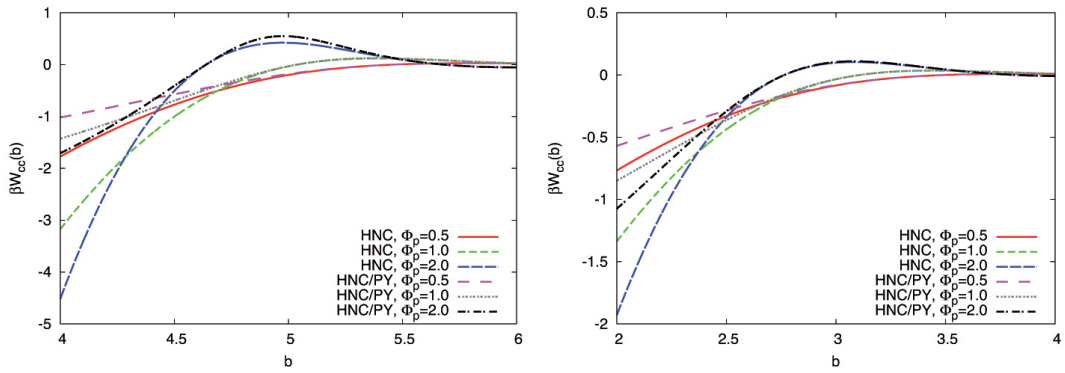

Figure 4.17. Effective colloid-colloid pair potential as a function of $b = r/\hat{R}_g$ for different values of Φ_p. Results for $q = 0.5$ (left) and $q = 1$ (right). We use the HNC and the HNC/PY closures (RY results are identical, on the scale of the figure, to the HNC ones).

4.3.2.6 Effective colloid-colloid pair potential

It is interesting to adopt a different CG approach, computing the effective colloid-colloid pair potential, which is obtained by integrating out the polymer degrees of freedom in the limit of zero colloidal density. Such an approach has been extensively used in the past, due to its simplicity and its connection with the Asakura-Oosawa-Vrij [54, 55] description. Here, we use it to further understand if the merits/demerits of the different closures we have discussed can be rationalized in this simpler approach. To determine the effective potential, we should compute the pair distribution function $g_{cc}(r)$ for $\Phi_c \to 0$ as a function of Φ_p and then define

$$\beta W_{cc}(r; \Phi_p) = -\ln g_{cc}(r). \tag{4.28}$$

Results obtained by using the HNC and the HNC/PY closures are reported in Fig. 4.17 (the RY ones cannot be distinguished from the HNC results on the scale of the figure). As expected, the potentials are strongly attractive at contact, i.e. for $r = 2R_c$. We expect the HNC closure to provide essentially exact estimates as this closure is very accurate for soft potentials (a discussion in the hard-wall case, $q \to 0$, is reported in Ref. [74]). On the other hand, the HNC/PY appears to be inaccurate close to contact. Attraction is too weak, a consequence of the fact that the HNC/PY closure underestimates the value of the pair correlation function at contact, a result already observed at finite values of Φ_c (see Fig. 4.12).

It is interesting to use potential $W_{cc}(r)$ to determine the presence/absence of phase separation. For this purpose, we can use the results of Refs. [123, 124] that predict separation when $B_2^*(\Phi_p) = B_2(W)/B_{2,HS} \lesssim -1.5$, where $B_2(W)$ is the second virial coefficient computed by using $W_{cc}(r; \Phi_p)$ and $B_{2,HS} = 4\pi(2R_c)^3/3$ is the corresponding quantity for a pure hard-sphere system. Results are reported in Fig. 4.18.

For $q = 1$, $B_2^*(\Phi_p)$ is always larger than -1.5, indicating the absence of phase separation, in agreement with the Monte Carlo results of Section 4.3.1. For $q = 0.5$, the HNC potential predicts the critical point to occur at (reservoir) polymer volume fraction $\Phi_p^{(r)} \approx 0.8$, which is in very good agreeement with the Monte Carlo estimate

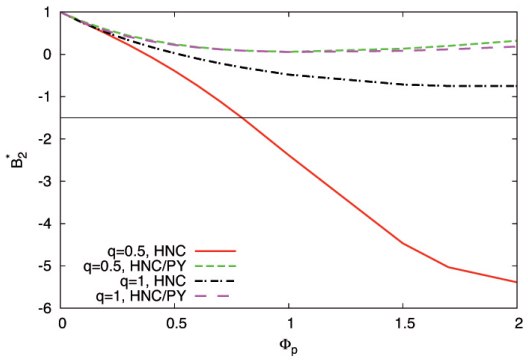

Figure 4.18. Reduced second virial coefficient, $B_2^* = B_2(W)/B_{2,HS}$, as a function of Φ_p for $q = 0.5$ and $q = 1$.

$\Phi_p^{(r)} \approx 0.823$ of Section 4.3.1, confirming the correctness of the phenomenological criterion introduced in Refs. [123, 124]. Note that no phase transition is predicted by using the HNC/PY closure, which is therefore incorrect even at the qualitative level. This is clearly related to the fact that the HNC/PY closure strongly underestimates the short-range depletion attraction.

Chapter 5

Star polymers

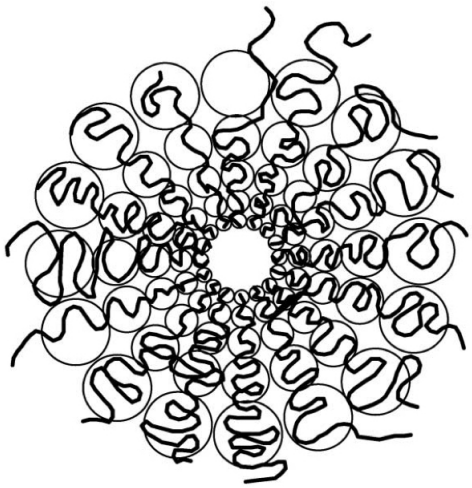

Figure 5.1. Schematic representation of a star polymer [46].

Star polymers are macromolecules obtained by tethering f linear chains (f is called the **functionality** of the star and each linear chain is called arm) to a central common core [46], where each arm is composed by $L \gg 1$ monomers, see Fig. 5.1. They belong to the class of branched macromolecules, and present many well-known technological applications, from lubricant additives to paints. Star polymers are a typical soft-matter system, but show additional properties with respect to the linear-polymer case, which depend on the functionality f. Indeed, while for small values of f the stars behave essentially as linear chains, by increasing f conformations become more spherical, stiffer, and they essentially behave as soft colloids: this "polymer-to-colloid" crossover behavior raised great interest in the literature, due to the growing importance of building-up materials with tunable properties.
As in the case of linear chains, star polymer solutions exhibit large-scale universality for several structural and thermodynamic observables, in the large degree of polymerization limit $L \to \infty$ [125, 126]. However, due to their complex geometry, star polymers are much more difficult to investigate than their linear counterparts, both theoretically and numerically, especially in the colloidal limit $f \gg 1$. In the last

decades, even the "simple" characterization of the conformational properties of a single molecule has been the subject of debate, and mostly analyzed by means of simple phenomenological models [129, 130].
For what concerns their thermodynamic behavior, little is known. Indeed, the field-theoretical methods which are so successful in the description of linear polymers [29–31] cannot be applied to the case of star polymers for large values of f [127, 128]. Therefore, these systems have been mostly analyzed by considering coarse-grained models, such as those discussed in Chapt. 3, both in the single-blob and multiblob pictures.
Several quantitative as well as qualitative zero-density pair potentials in the scaling-limit have been proposed, in a coarse-grained (CG) approach and at the single-blob (SB) level [75, 76]. Most of the discussion has been based on the central-monomer representation, for which some exact, theoretical predictions for the zero-density (two polymers) pair potential at full overlap $u^{(2)}(r \approx 0)$ are available [79].
In this chapter, we will start the discussion by presenting the Daoud-Cotton model [129], which is able to provide some phenomenological predictions for the conformation of a single star polymer, and we will critically analyze its limits of validity.
Thereafter, we will present coarse-grained, single-blob models for star polymers in good solvents, using both the center of mass (CM) and the central-monomer (MP) representations.
Since SB models are predictive only in the dilute regime, we will then present a multi-site model for star polymers, which should be able to describe the thermodynamic behavior of star polymer solutions with up to $f = 40$ arms and for volume fraction $\Phi_p = 4\pi/3\rho_p \hat{R}_g^3 \lesssim 2.4$, thus reaching the semidilute regime. The multi-site and single-site predictions for the thermodynamic and structural properties of star polymers in good solvents will then be compared.

5.1 Daoud-Cotton model

The Daoud-Cotton model [129] provides, in a phenomenological approach, several predictions for the conformational properties of a single star polymer in a good solvent.[1] In this model, a star polymer is composed by f polymer chains of $L \gg 1$ monomers each, tethered to a common center located at $\mathbf{r} = 0$, see Fig. 5.1. The system is reasonably assumed to have spherical symmetry around this center. The presence of a central point generates inhomogeneity in the monomer density $\rho_m(r)$ around the central monomer, which is expected to be a decreasing function of r.
The average dimension of the star polymer is characterized by means of the so-called **corona radius** R_c, which is defined by the relation

$$Lf = 4\pi \int_0^{R_c} r^2 \rho_m(r) dr. \tag{5.1}$$

Being R_c a quantity which describes (although in a very crude way) the average radius of the molecule, it is natural to suppose that it should be somehow related to the average radius of gyration $\hat{R}_g$.
In analogy with the blob description of linear chains developed in Section 2.3.3, in the

[1] An analogous description of star polymers has been developed in Ref. [130].

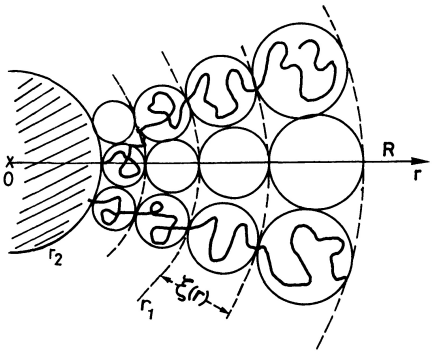

Figure 5.2. Partitioning of the star polymers into blobs of size ξ as assumed by the Daoud-Cotton model [129].

Daoud-Cotton model every arm is divided into a succession of blobs of average size ξ, so that no overlaps among different blobs occur, see Fig. 5.2. The fundamental difference between linear chains and star polymers is that in the latter the correlation length ξ depends on the distance from the center: $\xi(r)$ is expected to be an increasing function of r as a consequence of the screening of the excluded volume interactions. The screening arises at high monomer concentrations, hence it will become more and more relevant as we move from the outer shell towards the core.
The dependence of ξ on r and f can be obtained by assuming the sphere of radius r to be fully covered by the f blobs, one for each arm, so that $\xi^2 f \sim r^2$. Hence, we obtain the scaling relation

$$\xi(r) \sim r f^{-1/2}. \tag{5.2}$$

While this is a poor assumption in the low functionality limit, it should become more and more accurate when $f \gg 1$. We therefore expect the Daoud-Cotton model to be reliable in the colloidal limit only.
In order to determine the monomer density profile $\rho_m(r)$, the star is assumed to be divided in three different concentration regions, see Fig. 5.2. In the outer shell or **swollen region**, for distances $r > r_1 \sim b_m f^{1/2}$ [129], where b_m is the typical size of the microscopic monomer, inside each blob we have interactions of excluded volume type (there is no overlap among different arms). For $r \lesssim b_m f^{1/2}$, we have the inner shell or **unswollen region**, where there is strong overlap among the different arms, so that monomers inside each blob behave as ideal subchains, and the central shell or **core** where the monomer concentration is constant.
Here, we will focus only on the swollen region, since it is the only relevant region in the scaling limit $L \to \infty$.[2] If $n(r)$ is the number of monomers inside a blob at a distance r from the core, we have from Eq. (2.55)

$$\xi(r) \sim n(r)^{\nu}. \tag{5.3}$$

[2]This can be noted by the fact that the swollen region extends on distances $b_m f^{1/2} \lesssim r \lesssim R_c$. In the scaling limit $L \to \infty$, R_c becomes large while b_m remains finite. Therefore, the fraction of monomers in the inner regions becomes vanishingly small.

By combining Eq. (5.2) and Eq. (5.3), we obtain

$$\rho_m(r) \sim \frac{n(r)}{\xi^3(r)} \sim \xi^{(1/\nu-3)} \sim f^{(3\nu-1)/2\nu} r^{(1-3\nu)/\nu}. \tag{5.4}$$

In good solvents, $\nu \approx 0.588$ and the Daoud-Cotton model predicts

$$\rho_m(r) \sim f^{0.65} r^{-1.3}, \quad r > r_1. \tag{5.5}$$

In the unswollen region, the model predicts $\rho_m(r) \sim f^{1/2} r^{-1}$, while in the core the density is constant [129]. Combining these behaviors, and by means of Eq. (5.1), the Daoud-Cotton model predicts for the corona radius the scaling form

$$R_c^2 \sim f^{1-\nu} L^{2\nu}. \tag{5.6}$$

The corona radius R_c of the Daoud-Cotton model, defined in Eq. (5.1), is a phenomenological quantity for the characterization of the size of a star, and should be connected to physical quantities such as the average center-to-end distance $\hat{R}_{ce}$ or the average radius of gyration of the molecule $\hat{R}_g$. In the scaling limit $L \to \infty$, they are expected to behave as

$$\hat{R}_{ce}^2 \sim a_{ce}^*(f) L^{2\nu}, \tag{5.7}$$

$$\hat{R}_g^2 \sim a_g^*(f) L^{2\nu}, \tag{5.8}$$

where $a_{ce}^*(f)$ and $a_g^*(f)$ are non-universal amplitudes. A universal quantity in the limit $L \to \infty$ is the ratio

$$\frac{\hat{R}_g^2}{\hat{R}_{ce}^2} = H(f) = \frac{a_g^*(f)}{a_{ce}^*(f)}. \tag{5.9}$$

In order to determine the Daoud-Cotton prediction for $\hat{R}_g$ and $\hat{R}_{ce}$, we proceed as proposed in Ref. [135]. In the colloidal limit $f \to \infty$, the center of mass of the star moves towards the central monomer, hence we should have

$$\frac{1}{fL} \int d^3 r r^2 \rho_m(r) = \hat{R}_g^2. \tag{5.10}$$

The monomer density $\rho_m(r)$ is not a universal quantity, being dimensionful. A universal quantity is obtained if one considers

$$\bar{\rho}_m(r) = \frac{\hat{R}_g^3 \rho_m(r)}{Lf}, \tag{5.11}$$

which becomes a universal function of $b = r/\hat{R}_g$ in the scaling limit $L \to \infty$, and satisfies the normalization condition

$$4\pi \int_0^\infty db b^2 \bar{\rho}_m(b) = 1. \tag{5.12}$$

From Eq. (5.10), in the limit $f \to \infty$ we have

$$\mathcal{N} = 4\pi \int_0^\infty db b^4 \bar{\rho}_m(b) \underset{f\to\infty}{\longrightarrow} 1. \tag{5.13}$$

The Daoud-Cotton predictions for the universal quantity $\bar{\rho}_m(b)$ in the limit $L \to \infty$ of Eq. (5.5) can be summarized as

$$\begin{aligned} \bar{\rho}_m(b) &= C_{DC} b^{-\epsilon} \quad b \leq R_c/\hat{R}_g \\ \bar{\rho}_m(b) &= 0 \qquad b \leq R_c/\hat{R}_g, \end{aligned} \tag{5.14}$$

where $\epsilon = (3\nu - 1)/\nu \approx 1.298$. Imposing the normalization condition (5.12) and $\mathcal{N} = 1$ one obtains

$$\frac{R_c}{\hat{R}_g} = \left(\frac{5-\epsilon}{3-\epsilon}\right)^{1/2} \approx 1.475, \tag{5.15}$$

$$C_{DC} = \frac{3-\epsilon}{4\pi}\left(\frac{5-\epsilon}{3-\epsilon}\right)^{(\epsilon-3)/2} \approx 0.0699. \tag{5.16}$$

Since the corona radius R_c is of the order of the radius of gyration $\hat{R}_g$, by comparing Eqs. (5.8) and (5.7) with Eq. (5.6) we see that the Daoud-Cotton model predicts

$$a_g^*(f), a_{ce}^*(f) \sim f^{1-\nu} \approx f^{0.41}, \quad f \gg 1. \tag{5.17}$$

The Daoud-Cotton predictions for the star polymer size and structure have been extensively tested in the literature. A molecular dynamics simulation analysis of a continuum star polymer model was performed by Grest [131], which confirmed the scaling behavior of Eq. (5.17) for a_{ce}^*, and the monomer density $\rho_m(r)$ behavior given by Eq. (5.4) for $f \gtrsim 10$, although with quite short arms, each composed of $L = 100$ monomers. Later, in Ref. [132] Hsu *et al.* performed an extensive study of star polymers with functionalities up to $f = 80$, by means of Monte Carlo simulation of the lattice Domb-Joyce (DJ) model [35]. The behavior of the average center-to-end distance $\hat{R}_{ce}$ was analyzed, and they found that their data for $f \leq 80$ were consistent with $a_{ce}^*(f) \sim f^{0.235}$, to be compared to the Daoud-Cotton scaling result of Eq. (5.17). Therefore, they concluded that the Daoud-Cotton predictions, if valid, should hold only for $f \gg 80$.[3]

The monomer density profile $\rho_m(r)$ was analyzed in Refs. [133, 134] by means of molecular dynamics simulations of star polymers with $10 \leq f \leq 30$ arms, each composed by $L \approx 50$ monomers. They confirmed the scaling relation $\rho_m(r) \sim f^{0.65} r^{-1.3}$ occurring in an interval of values of r up to $r \approx R_c$, followed by a Gaussian decay for $r \gtrsim R_c$, which is not predicted by the Daoud-Cotton model.

In Ref. [135], a comprehensive analysis of the structure and zero-density thermodynamic behavior of star polymer solutions was performed by means of Monte Carlo simulations of the lattice Domb-Joyce and Self-avoiding walk models. Several values of L in the interval $100 \lesssim L \lesssim 1000$ for $f \leq 40$ and in $100 \lesssim L \lesssim 400$ for $f = 80$ and 120 were considered, and the resulting data were extrapolated to the scaling limit $L \to \infty$. They confirmed the Daoud-Cotton prediction (5.17), although significant correction to scaling were present even at $f = 120$. They moreover confirmed, in addiction to the scaling behavior of the monomer density of Eq. (5.5), the presence of a Gaussian tail in the monomer density at $r \gtrsim b_c = R_c/\hat{R}_g$, and for $f \leq 40$.

[3] It is important to stress that for $1 \leq f \leq 40$, they simulated stars with $L \leq L_{\max} \approx 10^3$, while their data for $f = 50, 60, 70, 80$ were obtained with $L < L_{\max} \approx 100$, hence correction to scaling are present.

Since the meaning of the "colloidal limit" is not yet very well understood, they critically analyzed the structural behavior and the zero-density thermodynamics for $f \to \infty$. For what concerns the universal ratio $H(f)$ defined in Eq. (5.9), they found [135]

$$\lim_{f\to\infty} H(f) = H_\infty = 0.58(1), \tag{5.18}$$

which is very close to the value of $\hat{R}_g^2/R^2$ for hard spheres, $H_{HS} = 3/5 = 0.6$.
The same consistency holds if one considers the universal ratio $g^*(f) = A_3(f)/A_2^2(f)$, where $A_2(f) = B_2(f)/\hat{R}_g^3$ and $A_3(f) = B_3(f)/\hat{R}_g^6$. They found

$$\lim_{f\to\infty} g^*(f) = g^*_\infty \approx 0.61, \tag{5.19}$$

which is very close to the hard-sphere value $g_{HS} = 5/8 = 0.625$. One could then guess that in the limit $f \to \infty$ these systems behave essentially as hard spheres. However, they found that the compatibility between the zero-density thermodynamics of star polymer and hard spheres only holds at the level of the ratio g^*: indeed, their extrapolation for the coefficient $A_2(\infty)$ for star polymers in the colloidal limit differ from $A_{2,HS}$ for hard spheres of radius R_c, thus leading to different thermodynamic properties [135].

5.2 Single-blob models

The numerical investigation of the thermodynamic properties of star polymers in the high molecular-weigth limit becomes rapidly unfeasible due to the huge number of degrees of freedom involved. Therefore, most of the literature relied on qualitative and quantitative single-blob models in the pairwise-additive approximation, such as those introduced in Sec. 3.1, mainly focusing on the central monomer (MP) representation. The choice of this representation is based on the results of Ref. [79], which is able to relate the behavior of the intermolecular potential at short distance $u^{(2)}_{MP}(b \approx 0)$ to the star polymer partition function in the scaling limit and the Flory exponent ν [79]. In the large-L limit, the star polymer partition function scales as

$$Q_1(L, f) \sim \tau^{Lf} L^{\gamma_f - 1}, \tag{5.20}$$

where τ is a model dependent prefactor, while γ_f is a universal exponent. The short-distance behavior of the zero-density pair potential $u^{(2)}_{MP}(b)$ is obtained by noting that when two star polymers of f arms each are brought at distances of the order of the bond length, the system can be seen as a star polymer with $2f$ arms. One obtains

$$u^{(2)}_{MP}(b \approx 0) = -\frac{2\gamma_f - \gamma_{2f} - 1}{\nu} \ln|b|, \quad b \approx 0, \tag{5.21}$$

where $b = r/\hat{R}_g$ and γ_f and γ_{2f} are the universal exponents characterizing the partition function of star polymer with f and $2f$ arms, respectively.

The potential shows a soft logarithmic divergence, and its amplitude is tuned by the parameter $b_f = (2\gamma_f - \gamma_{2f} - 1)/\nu$. In Ref. [81], Pelissetto performed an analysis based on general grounds, predicting the prefactor b_f to scale as $b_f \sim f^{1.68}$ in the colloidal limit $f \to \infty$. In Ref. [75], by means of the phenomenological Daoud-Cotton

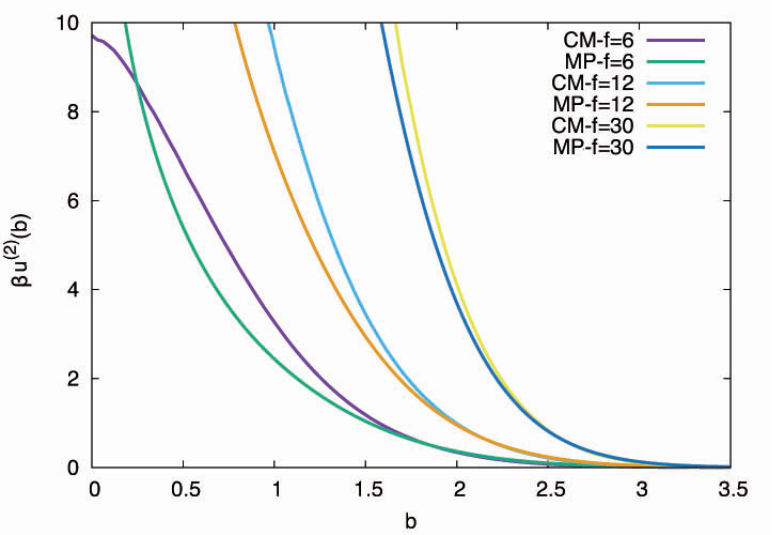

Figure 5.3. Effective pair potential $\beta u^{(2)}(b)$ in the CM and MP representations, as a function of $b = r/\hat{R}_g$, for $f = 6$, 12 and 30.

model, the prefactor b_f was predicted to scale as $b_f \sim f^{3/2}$ and a qualitative pair potential was proposed, which should be valid for $f \gg 1$ (where the Daoud-Cotton model applies). It showed the correct logarithmic behavior for short distances, while a Yukawa decay was postulated for the tail of the interaction. Later, in Ref. [132] Hsu *et al.* performed a careful analysis of the exponents γ_f in the scaling limit, by means of Monte Carlo simulations of the lattice Domb-Joyce model, and in Ref. [76] reported the scaling limit pair potential for star polymers. They confirmed the logarithmic form of the interaction on short distances [79]

$$u_{MP}^{(2)} \approx u_{WP}^{(2)} = b_f \ln(a_f b), \quad b \lesssim 1, \tag{5.22}$$

and predicted the prefactor b_f to scale as $b_f \sim f^{1.58}$. For $b \gtrsim 1$, the form of the interaction was compatible with a Gaussian decay

$$u_{MP}^{(2)} \approx u_G^{(2)} = c_f e^{-d_f b^2}, \quad b \gtrsim 1. \tag{5.23}$$

Their final parametrization for the pair potential $u_{MP}^{(2)}(b)$ reads [76]

$$u_{MP}^{(2)} = \frac{1}{\tau_f} \ln \left[e^{\tau_f u_{WP}^{(2)}(b) - d_f b^2} + e^{\tau_f u_G^{(2)}(b)} \right], \tag{5.24}$$

where the coefficients b_f, a_f, c_f, d_f e τ_f where computed for functionalities $2 \leq f \leq 35$, and are reported in Ref. [76].
The comparison of the thermodynamics of the qualitative SB potentials proposed in Ref. [75], based on the Daoud-Cotton model, with that of the exact potential of Eq. (5.24) was performed in Ref. [77], finding for $2 \leq f \leq 40$ a very poor agreement. Therefore, these phenomenological potentials for star polymers will not be considered any further in the discussion.

In Sec. 4.2 we discussed that single-blob models for linear polymers present strong representation problems: quite different thermodynamics are obtained if one chooses different effective interaction sites, such as the central monomer or the center of mass. Hence, we perform the same analysis for star polymers. For the central monomer representation we use the parametrization of Eq. (5.24), while the pair potential $u^{(2)}_{CM}$ in the center of mass representation is obtained by means of Monte Carlo simulations of the lattice Domb-Joyce model, and Eq. (3.10).
A comparison of the pair potentials $u^{(2)}$ in the center of mass and central monomer representations is reported in Fig. 5.3, for $f = 6$, 12 and 30. We see that the logarithmic divergence of $u^{(2)}_{MP}(b)$ for $b \approx 0$ is not shared by $u^{(2)}_{CM}(b)$, which at $f = 6$ is reasonably soft at full overlap, although the CM potential is slightly more repulsive than the MP potential at intermediate distances. As expected, the two representations tend to coincide as f increases, since the center of mass of the star tends to the central monomer for $f \gg 1$. As discussed in Sec. 3.1, pairwise-additive SB models neglect many-body intermolecular interactions among the coarse-grained molecules, which should become relevant in the semidilute regime $\Phi_p \gtrsim 1$, when different molecules are able to overlap. Three-body interactions in the central monomer representation have been studied in Ref. [136] for the particular configuration of three star polymers on the edge of a equilateral triangle of side b. They predicted a negative, ultrasoft logarithmic divergence of the three-body interaction for $b \to 0$. An analysis based on general considerations has been performed in Ref [81]. The generic n-body potential has been proven to be repulsive for n even and attractive for n odd, with a logarithmic divergence when **all** the n polymers are at full overlap.

5.3 Multiblob model

As explained in Sec. 3.2, in multiblob (MB) models every polymer is mapped onto a set of n effective interaction sites, obtained by grouping together the monomers into subunits. The interactions among these sites are parametrized in terms of intramolecular and intermolecular potentials. This mapping should reduce multiple overlaps among different molecules, so that many-body intermolecular interactions should be negligible even in the semidilute regime. In this way, polymers interact by means of zero-density intramolecular potentials, and intermolecular interactions at a two-polymer level. Intramolecular interactions [see Eq. (3.32)] are inherently n-body, because they must account for the connectivity and the long-range repulsion among the sites of a single molecule. Intermolecular interactions [see Eq. (3.33)] can be simplified further, as long as no multiple overlaps among blobs belonging to different molecules occur, by working in the blob pairwise-additive approximation. In this section, we will apply these concepts to the development of a multiblob model which is able to describe the scaling properties of star polymers in good solvents, with an increasing number of arms f.
The first step is the choice of the effective interaction sites $\mathbf{R}_{\alpha,i}$ defined in Eq. (3.29). We decide to divide each star polymer into $(f + 1)$ subunits of $m = Lf/(f + 1)$ monomers each, one for the center and one for each arm, as shown in Fig. 5.4. Each effective interaction site $\mathbf{R}_{\alpha,i}$, $\alpha = 1, \ldots, N_p$, $i = 0, \ldots, f$ (we identify $\mathbf{R}_{\alpha,0}$ with the

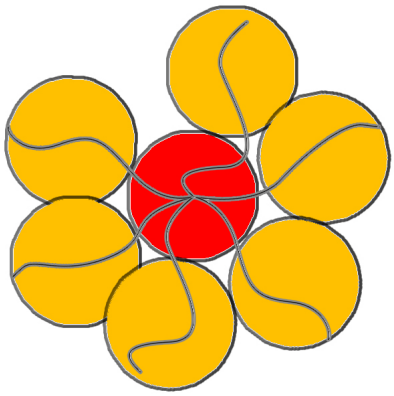

Figure 5.4. Schematic representation of the multiblob model for star polymers, as explained in the text: each star is divided into $(f+1)$ subunits or blobs, one for the center and one for each arm.

central blob of each molecule) is then obtained as the center of mass of each subunit

$$\mathbf{R}_{\alpha,i} = \mathbf{T}[\{\mathbf{r}^{(j)}_{\alpha,i}\}] = \frac{1}{m}\sum_{j=1}^{m} \mathbf{r}^{(j)}_{\alpha,i}, \tag{5.25}$$

where $\mathbf{r}^{(j)}_{\alpha,i}$, $\alpha = 1,\dots,N_p$, $i = 0,\dots,f$, $j = 1,\dots,m$ is the coordinate of the i-th monomer belonging to the j-th subunit of molecule α.
By neglecting many-body intermolecular interactions, as explained in Sec. 3.2, the total interaction among the effective sites reads

$$V_{N_p}(\{\mathbf{R}_{\alpha,i}\}) = \sum_{\alpha=1}^{N_p} V^{\text{intra}}(\{\mathbf{R}_{\alpha,i_\alpha}\}, f+1) + \sum_{\alpha<\beta=1}^{N_p} V^{\text{inter}}(\{\mathbf{R}_{\alpha,i_\alpha}\},\{\mathbf{R}_{\beta,i_\beta}\}), \tag{5.26}$$

where $i_\alpha, i_\beta = 0,\dots,f$. V^{intra} and V^{inter} are the intramolecular and intermolecular interactions, obtained in the zero-density limit (one or two star polymers). Once again, the determination of their *exact* form is far too complex in practice, hence an approximate set of intramolecular and intermolecular potentials must be introduced. In the next sections we will describe our approach in the case of star polymers, and how this set of interactions has been parametrized and obtained.

5.3.1 Intramolecular interactions

As explained in Sec. 3.2.1, the determination of the *exact* total intramolecular potential $V^{\text{intra}}(\{\mathbf{R}_i\}, f+1)$ defined in Eq. (3.41), $i = 0,\dots,f$, is unfeasible in practice, as it is a function of $3(f-1)$ scalar combinations of the blob coordinates $\mathbf{R}_i$, due to translational and rotational invariance.
Hence, approximations must be introduced. There is no clear prescription for the choice of the effective, approximate interactions: our choice, which is mostly dictated by practical considerations, is to define a set of scalar coordinates x_i, which are

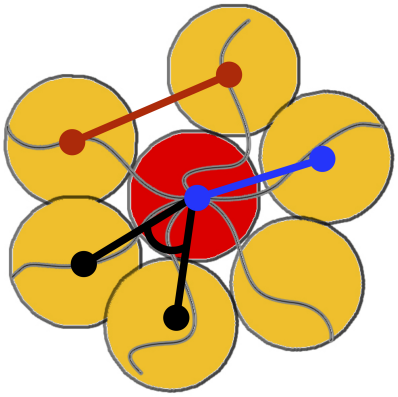

Figure 5.5. Scalar variables chosen for the description of intramolecular interactions: center-arm distance (blue line), arm-arm distance (red line), bond angle (black line).

functions of the blob coordinates $\mathbf{R}_i$, and parametrize the total interaction as a sum of potential $V_i(x_i)$, each depending on one of the scalar variables

$$V^{\text{intra}}(\{\mathbf{R}_i\}, f+1) = \sum_i V_i(x_i). \tag{5.27}$$

It is important to stress that the variables x_i must take into account the original $(f+1)$-body nature of the interactions.
In the case of star polymers, as shown in Fig. 5.5, we choose as scalar variables the distances $s_i = |\mathbf{R}_i - \mathbf{R}_0|$, $i = 1, \ldots, f$, from each arm to the central blob, the arm-arm distances $s_{ij} = |\mathbf{R}_i - \mathbf{R}_j|$, $i, j = 1, \ldots, f$ and the cosines of the bond-angle of two arms in respect to the central blob

$$\cos\theta_{ij} = \frac{(\mathbf{R}_i - \mathbf{R}_0) \cdot (\mathbf{R}_j - \mathbf{R}_0)}{|\mathbf{R}_i - \mathbf{R}_0||\mathbf{R}_j - \mathbf{R}_0|}. \tag{5.28}$$

While the bond lengths s_i and s_{ij} are two-body variables, the cosines of the bond angles $\cos(\theta_{ij})$ are three-body variables.
Everything is invariant under the exchange of the arm blobs, therefore we need to introduce only three potentials: the center-arm potential $V_{\text{ca}}(r)$, the arm-arm potential $V_{\text{aa}}(r)$, and the bond-angle potential $V_{\text{th}}(\cos\theta)$. Our multiblob parametrization for the total intramolecular interaction of a star polymer is therefore

$$V^{\text{intra}}(\{\mathbf{R}_i\}, f+1) = \sum_{i=1}^{f} V_{\text{ca}}(|\mathbf{R}_i - \mathbf{R}_0|) + \sum_{i<j=1}^{f} V_{\text{aa}}(|\mathbf{R}_i - \mathbf{R}_j|) + \sum_{i<j=1}^{f} V_{\text{th}}(\cos\theta_{ij}). \tag{5.29}$$

In order to determine the potentials $V_{\text{ca}}(r)$, $V_{\text{aa}}(r)$ and $V_{\text{th}}(\cos\theta)$ we proceed as follows. By construction, the model must be able to reproduce the structure of the underlying polymer model, at least for the set of variables chosen.[4] The center-arm

[4]Indeed, since we are introducing only a subset of approximate interactions of the original many-body problem, the multiblob model will not in general be able to reproduce *every* distribution function.

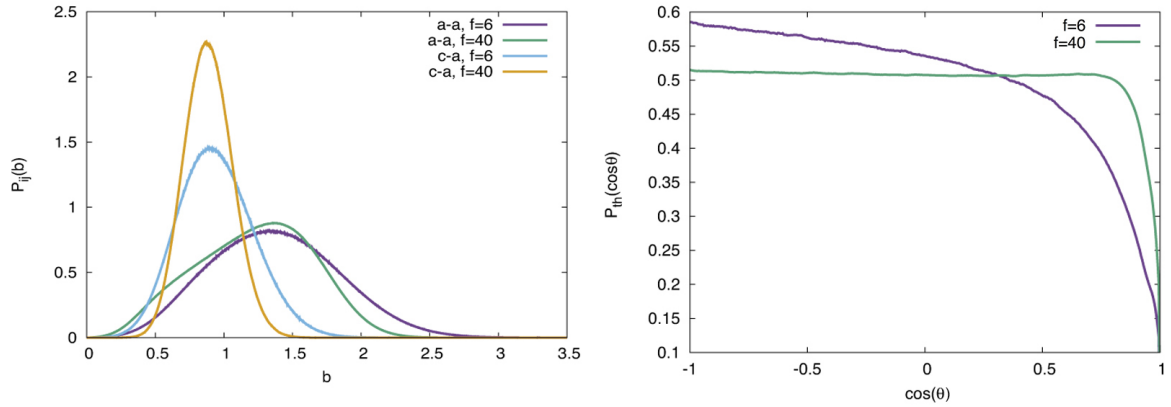

Figure 5.6. Probability distribution functions of the scalar variables chosen in the description of intramolecular interactions, for $f = 6, 40$. Left: arm-arm (a-a) and center-arm (c-a) distance probability distributions, as a function of $b = r/\hat{R}_g$. Right: bond angle probability distribution as a function of $\cos\theta$

distance probability distribution function is defined as

$$P_{\mathrm{ca},i}(r) = \langle \delta(r - |\mathbf{R}_i - \mathbf{R}_0|) \rangle, \tag{5.30}$$

where the average is performed over the full microscopic model. Everything is invariant under the exchange of the arms, so that $P_{\mathrm{ca},i}(r) = P_{\mathrm{ca},j}(r)$, $i \neq j = 1, \ldots, f$, and we can define

$$P_{\mathrm{ca}}(r) = \frac{1}{f} \sum_{i=1}^{f} P_{\mathrm{ca},i}(r) = \frac{1}{f} \left\langle \sum_{i=1}^{f} \delta(r - |\mathbf{R}_i - \mathbf{R}_0|) \right\rangle. \tag{5.31}$$

Analogously, we can define the arm-arm distance probability distribution function as

$$P_{\mathrm{aa}}(r) = \frac{2}{f(f-1)} \sum_{i<j=1}^{f} P_{\mathrm{aa},ij}(r) = \frac{2}{f(f-1)} \left\langle \sum_{i<j=1}^{f} \delta(r - |\mathbf{R}_i - \mathbf{R}_j|) \right\rangle. \tag{5.32}$$

These distributions are nonuniversal, *i.e.* model-dependent, and satisfy the normalization condition

$$\begin{aligned} \int_0^\infty dr P_{\mathrm{ca}}(r) &= 1, \\ \int_0^\infty dr P_{\mathrm{aa}}(r) &= 1. \end{aligned} \tag{5.33}$$

Universal distributions are obtained if one considers the adimensional combinations $\hat{R}_g P_{\mathrm{ca}}(r)$ and $\hat{R}_g P_{\mathrm{aa}}(r)$. Indeed, in the scaling limit one has

$$\hat{R}_g P_{\mathrm{ca}}(r), \underset{L\to\infty}{\longrightarrow} \bar{P}_{\mathrm{ca}}(b), \tag{5.34}$$

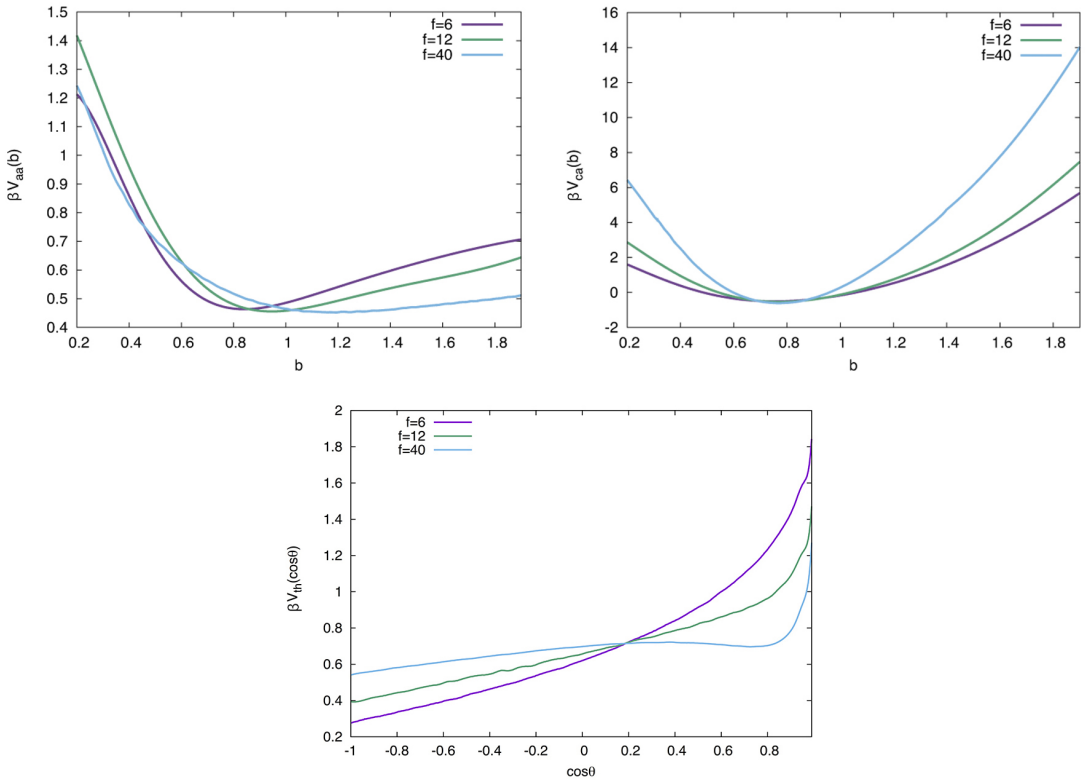

Figure 5.7. Intramolecular potentials for $f = 6$, 12 and 40. Top: arm-arm potential $\beta V_{\rm aa}$ [left] and center-arm potential $\beta V_{\rm ca}$ [right], as a function of $b = r/\hat{R}_g$. Bottom: Bond-angle potential $\beta V_{\rm th}$, as a function of $\cos\theta$

$$\hat{R}_g P_{\rm aa}(r), \underset{L\to\infty}{\longrightarrow} \bar{P}_{\rm aa}(b), \tag{5.35}$$

where $b = r/\hat{R}_g$.
The probability distribution function of the cosine of the bond angle

$$P_{\rm th}(a) = \frac{2}{f(f-1)} \sum_{i<j=1}^{f} P_{{\rm th},ij}(a) = \frac{2}{f(f-1)} \left\langle \sum_{i<j=1}^{f} \delta(a - \cos\theta_{ij}) \right\rangle \tag{5.36}$$

is adimensional, and universal in the limit $L \to \infty$. It satisfies the normalization condition

$$\int_{-1}^{1} da P_{\rm th}(a) = 1. \tag{5.37}$$

These distributions were computed in the microscopic model by means of Monte Carlo simulations of the lattice Domb-Joyce model, and are shown in Fig. 5.6, for $f = 6$ and 40. By increasing the number of arm from $f = 6$ to $f = 40$, we see that the star configurations become stiffer (the center-arm distribution function $P_{\rm ca}(b)$ becomes more sharply localized) while, at the same time, the bond-angle probability distribution profile $P_{\rm th}(\cos\theta)$ becomes flatter for $\cos\theta \lesssim 0.8$, and decreases sharply as $\cos\theta \to 1$.

f	$\hat{R}^2_{g,b}/\hat{R}^2_g$ (FM)	$\hat{R}^2_{g,b}/\hat{R}^2_g$ (MB)
6	0.759	0.760
12	0.772	0.771
40	0.793	0.795

Table 5.1. Comparison of the full-monomer (FM) and multiblob (MB) normalized average radius of gyration in the blob model $\hat{R}^2_{g,b}/\hat{R}^2_g$, for $f = 6$, 12 and 40.

The CG multiblob potentials $\beta V_{\rm ca}(r)$, $\beta V_{\rm aa}(r)$ and $\beta V_{\rm th}(\cos\theta)$ which reproduce these distributions are determined by means of the iterative Boltzmann inversion method (IBI) [49]. As explained in Sec. 3.2.1, we require

$$P_i^{\rm FM}(x_i) = P_i^{\rm CG}(x_i), \tag{5.38}$$

where the superscript FM and CG indicates the set of distributions in the full-monomer and in the coarse-grained models, respectively. At each step of the iterative procedure, the potential were corrected as defined in Eq. (3.45).

The CG multiblob intramolecular potentials obtained by means of the IBI method are shown in Fig. 5.7, for $f = 6$, 12 and 40.

The center-arm potential $V_{\rm ca}$ is repulsive at short distance where blobs overlap, with an attractive tail at long distances, which is necessary to bind each arm to the center of the stars. It has a soft nature for $f = 6$, with $V_{\rm ca} \approx 2k_BT$ at full overlap, but it becomes harder for $f = 40$, with $V_{\rm ca} \approx 7k_BT$, confirming an increasing conformational rigidity of the star polymer as f increases. The arm-arm potential $V_{\rm aa}$ has a soft, repulsive core and an attractive tail which tends to vanish as f increases. The bond angle potential $V_{\rm th}$ is repulsive, and prevents the bond angle to vanish, as a consequence of the repulsive interaction among different arms. As f increases it becomes almost constant in the region $\cos\theta \lesssim 0.8$.

In order to assess the accuracy of the intramolecular coarse-grained potentials in reproducing the structure of the star polymer, we compare the full-monomer and CG average radius of gyration in the blob model, which is defined as

$$\hat{R}^2_{g,b} = \langle \mathbf{R}^2_{g,b} \rangle = \frac{1}{2(f+1)^2} \left\langle \sum_{i,j=0}^{f} (\mathbf{R}_i - \mathbf{R}_j)^2 \right\rangle . \tag{5.39}$$

It does not coincide with the average radius of gyration $\hat{R}_g$ of the original system, defined in Eq. (2.2). Indeed, the two quantities are related by

$$\hat{R}^2_g = \hat{R}^2_{g,b} + \hat{r}^2_{g,b}, \tag{5.40}$$

where $\hat{r}^2_{g,b}$ is the average blob radius of gyration

$$\begin{aligned} \hat{r}^2_{g,b} &= \frac{1}{(f+1)} \sum_{i=0}^{f} \hat{r}^2_{g,b,i}, \\ \hat{r}^2_{g,b,i} &= \frac{1}{2m} \left\langle \sum_{j,k=1}^{m} (\mathbf{r}_i^{(j)} - \mathbf{r}_i^{(k)})^2 \right\rangle . \end{aligned} \tag{5.41}$$

In Table 5.1, we report the average, blob model radius of gyration in the $\hat{R}^2_{g,b}/\hat{R}^2_g$, normalized to the average radius of gyration, comparing full-monomer and multiblob results. Differences are small, confirming the accuracy of the parametrization for intramolecular interactions.

5.3.2 Intermolecular interactions

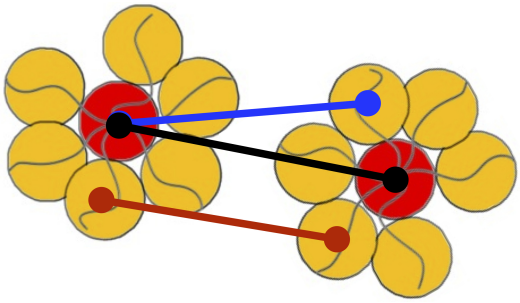

Figure 5.8. Relevant variables in the blobs pairwise-additive approximation for intermolecular interactions: center-arm distance (blue line), arm-arm distance (red line), center-center distance (black line).

We now define the set of intermolecular interactions employed in our multiblob model. As discussed in Sec. 3.2, by switching to a lower level of coarse graining we should be able to neglect many-body intermolecular interactions as soon as $\Phi_p \lesssim n^{3\nu-1}$. Hence, we need to determine the pair potential

$$V_{12}^{\text{inter}}(\{\mathbf{R}_{1,i_1}\},\{\mathbf{R}_{2,i_2}\}), \quad i_1, i_2 = 0,\dots,f. \tag{5.42}$$

This interaction is in principle a function of $6f$ scalar combinations of the blob coordinates, due to translational and rotational invariance. We can try to simplify it further by using the fact that our model is supposed to work only up to the overlap density of the blobs. Hence, we should be able to safely neglect many-body intermolecular interactions, working in the **pairwise-additive approximation among blobs**.
Due to translational and rotational invariance, the pair potentials among the blobs must be only function of the distance $r_{ij} = |\mathbf{R}_{1,i} - \mathbf{R}_{2,j}|$. Moreover, the invariance in the exchange of the arms implies that we need to determine only three potentials: the intermolecular center-arm potential $\tilde{V}_{\text{ca}}$, the intermolecular arm-arm potential $\tilde{V}_{\text{aa}}$ and the intermolecular center-center potential $\tilde{V}_{\text{cc}}$. We report the set of intermolecular variables in Fig. 5.8. The total intermolecular interaction then reads

$$\begin{aligned} V_{12}^{\text{inter}}(\{\mathbf{R}_{1,i_1}\},\{\mathbf{R}_{2,i_2}\}) &= \sum_{i,j=1}^{f} \tilde{V}_{\text{aa}}(|\mathbf{R}_{1,i} - \mathbf{R}_{2,j}|) + \\ &+ \sum_{\alpha,\beta\neq\alpha}^{2} \sum_{i=1}^{f} \tilde{V}_{\text{ca}}(|\mathbf{R}_{\alpha,i} - \mathbf{R}_{\beta,0}|) + \tilde{V}_{\text{cc}}(|\mathbf{R}_{1,0} - \mathbf{R}_{2,0}|). \end{aligned} \tag{5.43}$$

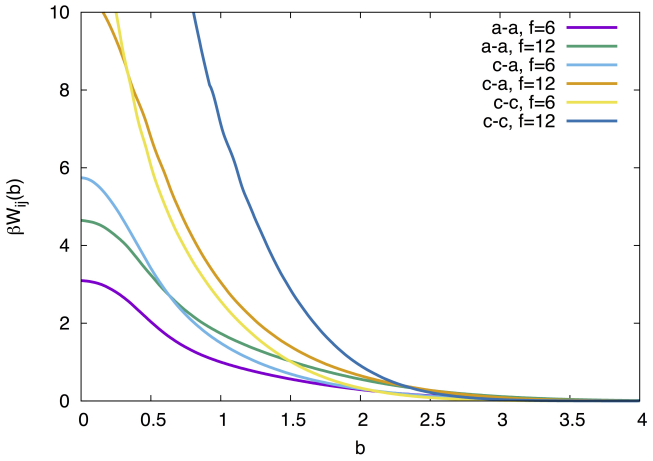

Figure 5.9. Potentials of mean force $\beta W_{\rm aa}$ (a-a), $\beta W_{\rm ca}$ (c-a) and $\beta W_{\rm cc}$ (c-c) as a function of $b = r/\hat{R}_g$, for star polymers with $f = 6$ and 12 arms.

In order to determine the three potentials $\tilde{V}_{\rm ca}$, $\tilde{V}_{\rm aa}$ and $\tilde{V}_{\rm cc}$, we proceed as described in Sec. 3.2.1. We require the multiblob model to correctly reproduce the thermodynamic behavior of the original system in the zero-density limit, at the level of the universal adimensional combination $A_2 = B_2/\hat{R}_g^3$, where B_2 is the second virial coefficient defined in Eq. (3.49). A_2 is strictly related to the potentials of mean force W_{ij}, $i, j = 0, \ldots, f$, defined in Eq. (3.52). Due to the invariance in the exchange of the arms, in the multiblob model we have only three independent functions, the center-arm, the arm-arm and the center-center potentials of mean force, which read, respectively

$$\begin{aligned}
\beta W_{\rm aa}(r) &= -\ln[\langle \exp(-\beta H_{12}^{\rm inter})\rangle_{\mathbf{R}_{1,i}=0,\mathbf{R}_{2,j}=r}], \quad i,j \neq 0,\\
\beta W_{\rm ca}(r) &= -\ln[\langle \exp(-\beta H_{12}^{\rm inter})\rangle_{\mathbf{R}_{1,0}=0,\mathbf{R}_{2,j}=r}], \quad j \neq 0,\\
\beta W_{\rm cc}(r) &= -\ln[\langle \exp(-\beta H_{12}^{\rm inter})\rangle_{\mathbf{R}_{1,0}=0,\mathbf{R}_{2,0}=r}].
\end{aligned} \tag{5.44}$$

These adimensional quantities tend, in the limit $L \to \infty$, to universal functions $\beta\overline{W}_{ij}(b)$, where $b = r/\hat{R}_g$. We computed them by means of Monte Carlo simulations of the lattice Domb-Joyce model, and report them in Fig. 5.9 for $f = 6$ and 12.
We see that the mean force potentials become more repulsive as f increases. As expected, star polymers become stiffer and compact object by increasing the number of arms.
The set of CG multiblob intermolecular potentials are required to reproduce the whole set of mean force potentials, hence

$$\beta W_{\rm ij}^{CG}(r) = \beta W_{\rm ij}^{FM}(r). \tag{5.45}$$

As discussed in Sec. 3.2.2, this choice ensures that the adimensional combination A_2 of the coarse-grained model will reproduce the full-monomer one. This was

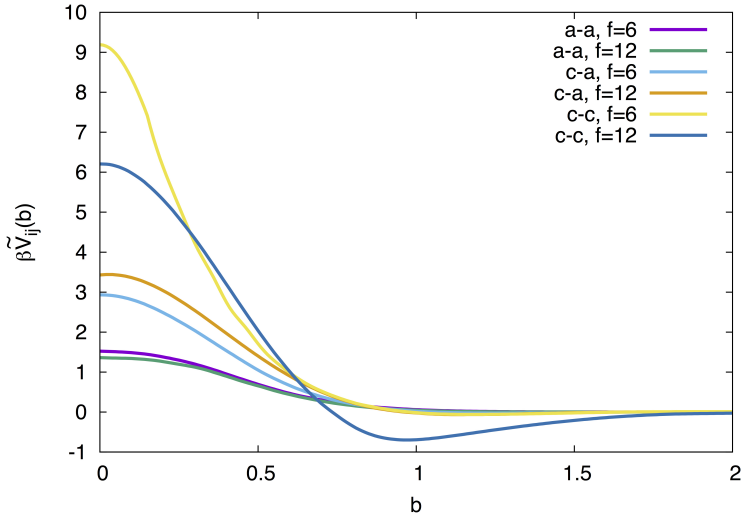

Figure 5.10. Intermolecular interactions of the multiblob model for $f = 6$ and 12. We show the arm-arm potential $\beta\tilde{V}_{\rm aa}$, the center-arm potential $\beta\tilde{V}_{\rm ca}$ and the center-center potential $\beta\tilde{V}_{\rm cc}$.

achieved by means of Monte Carlo simulations of the CG multiblob model, and the iterative Boltzmann inversion method [49]. At each step of the iterative procedure, the potentials were corrected with the prescription reported in Eq. (3.56). As f increases, however, we see from Fig. 5.9 that the mean force potentials W_{ij} develop long tails, up to $r/\hat{R}_g \approx 4$. In the iterative procedure, the presence of these tails gives rise to similar tails in the effective potential, which increase with the iterations. To avoid this effect, we modified the procedure by introducing functional corrections $a_{\rm ij}(r)$ in the IBI method, so that the update of the potentials at the end of each iterative step becomes

$$\tilde{V}_{(t+1),{\rm ij}}(r) = \tilde{V}_{t,{\rm ij}}(r) - a_{\rm ij}(r)[W^{CG}_{t,{\rm ij}}(r) - W^{FM}_{\rm ij}(r)]. \tag{5.46}$$

The mixing parameters $a_{\rm ij}(r)$ in Eq. (5.46) were fixed, somehow arbitrarily, to Gaussian functions

$$a_{\rm ij}(r) = A_{\rm ij} e^{-(r/\sigma_{\rm ij})^2}, \tag{5.47}$$

with amplitudes $A_{\rm ij}$ and standard deviations $\sigma_{\rm ij}$ which depend on the sites chosen (arm-arm, center-arm or center-center).
The set of intermolecular coarse-grained pair potentials $\beta V_{\rm ij}$ obtained by means of the IBI method are shown in Fig. 5.10, for $f = 6$ and 12. It is important to stress that each potential is only relevant for those distances at which $W^{FM}_{\rm ij}(r)$ is not too large. In particular, the c-c potential we determine is not meaningful for $b \lesssim 0.2$, 0.8 for $f = 6$, 12. This is not crucial, however, since the probability of visiting these regions is extremely low.

The arm-arm interaction is purely repulsive, and reasonably soft at contact, $\tilde{V}_{\rm aa}(b = 0) \approx 1.5 k_B T$. It increases only slightly passing from $f = 6$ to $f = 12$. The center-arm interaction is more repulsive than the arm-arm interaction, $\tilde{V}_{\rm ca}(b = 0) \approx 3 k_B T$, $3.5 k_B T$ for $f = 6$ and 12 respectively, but the two are comparable in range. The center-center potential is the most repulsive interaction. For small b it decreases from $f = 6$ to $f = 12$. However this occurs at distances at which the potential is not meaningful. Moreover, it develops an attractive tail for $r/\hat{R}_g \approx 1$, whose depth increases from $f = 6$ to $f = 12$.
We can test the accuracy of our multiblob model for star polymers by comparing its prediction for the universal combination $A_2 = B_2/\hat{R}_g^3$ with that obtained by means of full-monomer simulations. Our model predicts $A_2 = 14.231(4)$ for $f = 6$ and $A_2 = 23.782(5)$ for $f = 12$, to be compared with the accurate full-monomer results of Ref. [135], which reports $A_2 = 14.202(12)$ for $f = 6$ and $A_2 = 23.543(28)$ for $f = 12$. Differences are small, or the order of 1%, confirming the accuracy of our model in reproducing the potentials of mean force.

5.4 Results

In this section, we analyze the thermodynamic and structural properties of star polymer solutions in good-solvents, both at zero and finite density. As far as we know, there are no full-monomer results available in the literature for the scaling-limit behavior of this system, up to the semidilute regime. Hence, we will use the scaling-limit coarse-grained models introduced in Sec. 5.2 and 5.3.
Most of the literature on the subject has been based on the qualitative single-blob potential proposed in Ref. [75]. By means of this potential, several prediction for the phase diagram of star polymer solutions were obtained. In Ref. [137], a fluid-solid transition was predicted, for functionalities f above a critical value $f > f_c \approx 34$ in a volume fraction interval $1.5 \lesssim \Phi_p \lesssim 2$, where $\Phi_p = 4\pi/3 \rho_p \hat{R}_g^3$ is the star polymer volume fraction and $\rho_p = N_p/V$, with reentrant melting for higher values of Φ_p. The same model was then generalized to mixtures of colloid and star polymers [91], and mixtures of star polymers and linear chains [133]. The corresponding phase diagrams are reported in Refs. [94, 95] for the case of colloid/star-polymer mixtures, and in Ref. [138] for the case of mixtures of star polymers and linear chains. In Ref. [77], we determined the thermodynamic and structural properties using the accurate potential (5.24) of Ref. [76]. The results were compared to those obtained by using the qualitative potential of Ref. [75], finding a very poor agreement. In Ref. [77], by means of phenomenological approaches, we confirmed the presence of a fluid-solid transition to occur in the system. The critical functionality was set to $f_c \approx 35$, and the interval of coexistence $1.5 \lesssim \Phi_p \lesssim 2$. This interval, however, is beyond the limits of validity of zero-density SB models, which are expected to be accurate only in the dilute regime $\Phi_p \lesssim 1$.
In order to test the accuracy of single-blob models in the semidilute regime, in this section we compare the thermodynamic of the scaling-limit SB models defined in Sec. 5.2 with that of the multiblob model defined in Sec. 5.3, which will be taken as reference system. Since we know that SB models present problems connected to the choice of the representation, the analysis will be performed for both the central

	$f = 6$		$f = 12$	
	A_2	A_3	A_2	A_3
SB-CM	14.25	88.87	23.55	287.12
SB-MP	14.66	85.6	23.97	288
MB	14.231(4)	88.61(62)	23.782(5)	289(2)
FM	14.202(12)	90.3(4)	23.543(28)	290(2)

Table 5.2. Universal adimensional combinations A_2 and A_3 for $f = 6$, 12. We show single-blob models, center of mass (SB-CM) and central monomer (SB-MP) representations, multiblob model (MB), and the full-monomer (FM) results of Ref. [135].

monomer and the center of mass representations.
Moreover, the residual flexibility of the multiblob model allows us to analyze the single-molecule structural properties of star polymers as the density increases, a task which is impossible in zero-density SB models. This represents a significant improvement towards a better characterization of the aforementioned polymer-to-colloid crossover, which is expected to hold in the system as f increases.

5.4.1 Zero density

As explained in Chapt. 3, the accuracy of coarse-grained models in reproducing the correct thermodynamic behavior of the underlying microscopic system can be tested by means of the adimensional virial coefficients $A_i = B_i/\hat{R}_g^{3(i-1)}$ defined in Sec. 2.3.2.1.
Zero-density SB models with pair interactions, by definition reproduce the adimensional combination $A_2 = B_2/\hat{R}_g^3$, see Eq. (3.17). For what concerns our multiblob model, it is by construction able to reproduce the full-monomer site-site potentials of mean force $W_{\rm ij}$ defined in Eq. (3.52). Therefore, because of Eq. (3.49), the coefficient A_2 is reproduced as well.
We checked the accuracy of the various CG parametrizations by comparing their predictions for A_2 to the accurate FM value of Ref. [135]. Results for $f = 6$, 12 are presented in Table 5.2. We see that all CG models, both in the single and multiblob approximation, reproduce the FM value for A_2, the larger deviations ($\approx 3\%$) being observed for the central monomer representation.
The effect of three-body interactions on the thermodynamic behavior, which are neglected in all the CG approaches, can be tested by comparing the values of $A_3 = B_3/\hat{R}_g^6$ of the full-monomer model with those obtained by means of the coarse-grained models. As discussed in Sec. 3.2, we expect that the introduction of a multiblob description of star polymers should have reduced multiple overlaps: consequently, the contributions of many-body intermolecular interactions should become smaller. Therefore, we expect the third normalized virial coefficient A_3 of the MB model to better approximate full-monomer results than that of the SB models. We checked this assumption by computing A_3 in the various CG models, and by comparing them with the accurate full-monomer predictions of Ref. [135]. Results

are shown in Table 5.2. Since different single-blob representations lead to different values of A_3, we report the single-blob predictions in both the central monomer (SB-MP) and center of mass (SB-CM) representations.
All the CG models reproduce the full-monomer results, for $f = 6$ and 12. For what concerns single-blob models, the MP representation slightly underestimates A_3 for $f = 6$, if compared to the CM representation. However, deviations are again of the order of 3% and are probably connected to the parametrization of $u^{(2)}_{MP}$ presented in Ref. [76]. Deviations from full-monomer results are even smaller for the SB model in the center of mass representation and for the multiblob model.
We conclude that all the coarse-grained models we discuss succeed in reproducing the zero-density thermodynamics of the underlying polymer system, for $f = 6$ and 12.
It is interesting to compare the single-blob results for star polymers with the case of linear chains presented in Sect. 4.2.1. For linear chains, SB models underestimate the third virial coefficient A_3 in both cases: by 21% in the CM representation and by 50% in the MP representation. In star polymers, at a SB level, A_3 is instead well reproduced. We may infer that since these molecules are much more compact than their linear counterpart, multiple overlaps are rare, and thermodynamic behavior is dominated by pair interactions. This has been commonly assumed in the literature, stating that single-blob models with pair interactions should become more and more accurate as the number of arms f increases.
Moreover, the zero-density thermodynamic behavior of SB models for star polymers seem not to exhibit problems connected to the choice of the effective interaction site, as the universal coefficients A_2 and A_3 of the center of mass and central monomer representations are fully consistent. One may guess that this consistency holds even at higher densities.
All these conclusions, which are based on the zero-density thermodynamics only, must be validated by performing a finite-density analysis of the system.

5.4.2 Finite density

In this section, we compute the thermodynamic and structural behavior of coarse-grained models for star polymers at finite density, up to the semidilute regime. As far as we know, there are no scaling-limit, full-monomer results for star polymers to compare with, hence we will take the multiblob results as reference and compare its predictions with those obtained by means of single-blob models, in order to test their accuracy in reproducing the thermodynamic behavior of the system. It is important to first derive the limits of validity of our MB model, as predicted by Eq. (3.25), which states that a multiblob model with n effective sites should be accurate up to $\Phi_p \lesssim n^{3\nu-1}$. Although we take $f + 1$ sites to describe each star polymer, due to its geometrical construction the level of resolution of our model is not higher than a trimer representation, thus with $n = 3$. Eq. (3.25) then predicts $\Phi_p \lesssim 3^{3\nu-1} \approx 2.4$. For this reason, we decided not to use our MB model for volume fractions higher than $\Phi_p \approx 2$. For single-blob models, we computed the thermodynamic quantities by means of integral equation methods, and the Rogers-Young closure defined in Eq. (1.53). Indeed, as we saw in Chapt. 4, integral equations reasonably reproduce

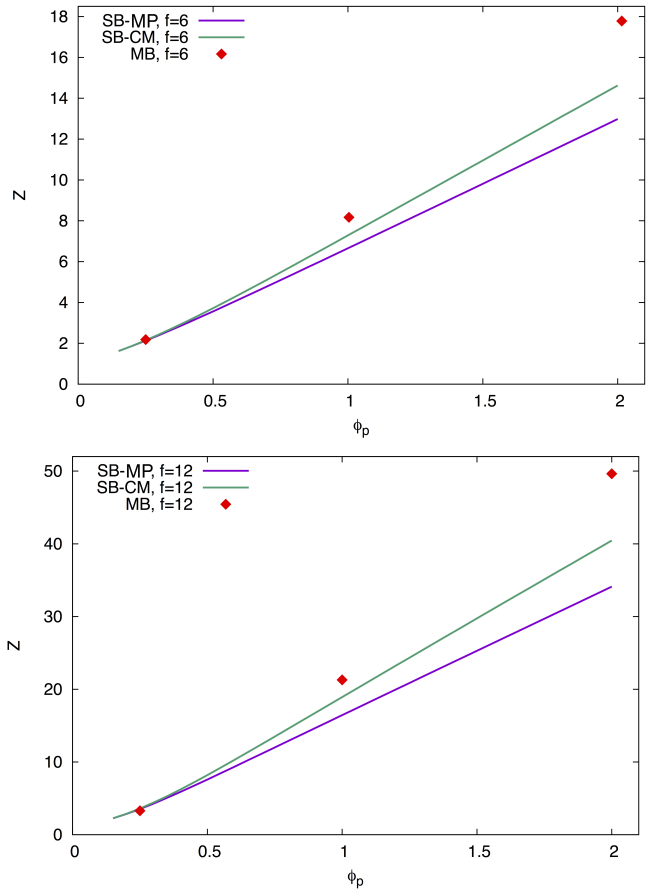

Figure 5.11. Osmotic coefficient $Z = \beta P/\rho_p$ as a function of the volume fraction Φ_p, for $f = 6$ (top) and $f = 12$ (bottom). We report multiblob (MB) results, single-blob results in the center of mass (SB-CM) and central monomer (SB-MP) representations.

the thermodynamic behavior of solutions of linear chains[5]. We decided to use the Rogers-Young closure instead of the hypernetted-chain closure, which showed to be very accurate in the case of linear chains, due to the most repulsive nature of the star polymer interaction. Multiblob results were computed by means of canonical Monte Carlo simulations in a box of volume $V \approx (30\hat{R}_g)^3$ with periodic boundary conditions, up to $\Phi_p = 2$.

We start the discussion by comparing the universal virial osmotic coefficient $Z(\Phi_p) = \beta P/\rho_p$. Its definition in SB models is reported in Eq. (1.35), while for the MB model we used the molecular definition of the virial pressure reported in Ref. [140, 141]. We report the results for $f = 6$ and 12 in Fig. 5.11.

For $f = 6$ and $f = 12$, the three models are fully consistent for low volume fraction $\Phi_p = 0.25$, further confirming the results of Sec. 5.4.1 on the zero-density thermodynamic consistency of the various coarse-grained models. At higher volume fractions, both SB models underestimate the osmotic coefficient of the MB model.

[5]See the results of Sec. 4.2.1 for solutions of linear chains, and of Sec. 4.3.2 for colloid-linear chains mixtures, in the limit of low colloid volume fractions.

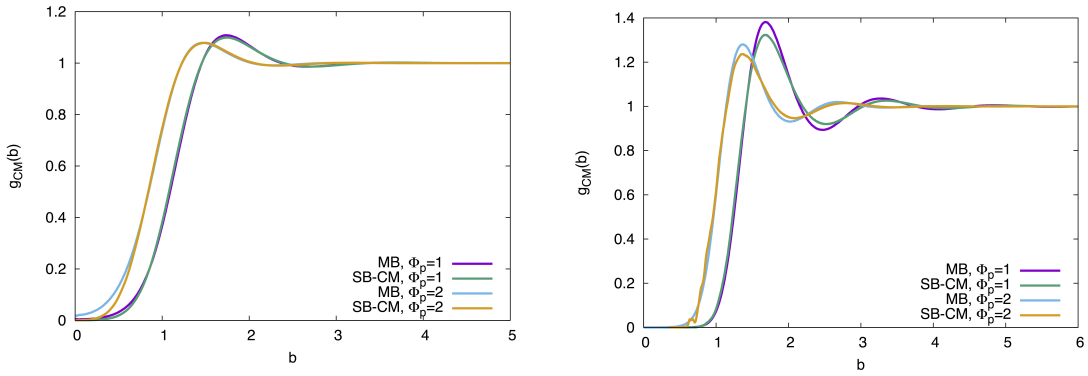

Figure 5.12. Center of mass distribution function $g_{CM}(r)$, as a function of $b = r/\hat{R}_g$, for $f = 6$ (left) and $f = 12$ (right). Results are shown for the mutliblob model (MB) and the single-blob model in the center mass representation (SB-CM), and for $\Phi_p = 1$ and 2.

As for the case of linear chains, the largest deviation is observed for the SB model in the central monomer representation. At $\Phi_p = 1$, we have $\Delta Z_{\rm MP}/Z_{\rm MB} \approx 20\%$, while $\Delta Z_{\rm CM}/Z_{\rm MB} \approx 12.5\%$, for both $f = 6$ and $f = 12$. At $\Phi_p = 2$, we have $\Delta Z_{\rm MP}/Z_{\rm MB} \approx 30\%$, while $\Delta Z_{\rm CM}/Z_{\rm MB} \approx 20\%$ again for both $f = 6$ and 12.
We conclude that zero-density SB models with pairwise-additive interactions poorly reproduce the thermodynamic behavior of star polymers solutions in the semidilute regime. As we obtained in the case of linear chains, problems connected to the choice of the effective interaction site are present. Moreover, since the deviations we observed are independent on f, at least for $f = 6$ and 12, one may question the validity of the assumption that zero-density single-blob models should become more and more accurate as we increase the functionality f of the stars, reaching the colloidal limit. Higher values of f, up to $f = 40$, are currently in preparation in order to test this result.
We now compare the predictions of the multiblob model with those of single-blob models for what concerns the intermolecular structure, focusing on the center-of-mass radial distribution function $g_{CM}(r)$. In this case, we will obviously consider the single-blob model in the CM representation only, as this distribution cannot be computed in the MP representation. The results for the correlation functions are shown in Fig. 5.12, for $f = 6$ and 12, at volume fractions $\Phi_p = 1$, 2.
In all cases, the positions of the peaks are reproduced. We see that although the multiblob model has been defined and parametrized only in terms of the effective interaction sites, it is able to reproduce the intermolecular structural properties of star polymers, when we further map each MB molecule onto its center of mass. Hence, the MB model can be truly seen as a bridging technique between a fully atomistic (FM) and a fully coarse-grained (SB) description of the system. For $f = 6$, we see that the MB and the SB-CM results are quantitatively comparable, both for $\Phi_p = 1$ and $\Phi_p = 2$. For $\Phi_p = 2$, the multiblob model seems to be softer at full overlap. Notwithstanding this, in Fig. 5.11 we see that the osmotic coefficient $Z(\Phi_p)$ is underestimated. For $f = 12$, the distribution functions are qualitatively comparable for both values of Φ_p, although the heights of the peaks are quantitatively

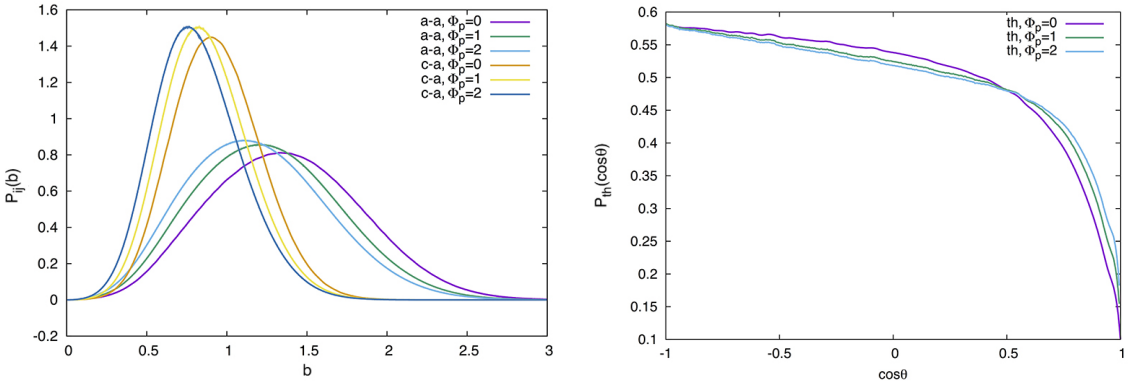

Figure 5.13. MB intramolecular distribution function $P_{\rm ca}(b)$, $P_{\rm aa}(b)$ as a function of $b = r/\hat{R}_g$ (left), and $P_{\rm th}(\cos\theta)$ as a function of $\cos\theta$ (right), for $f = 6$. Results are shown for $\Phi_p = 0$, 1 and 2.

different.

Again, since structural properties deviations of the SB model from the MB model seem to increase from $f = 6$ to $f = 12$, one may furthermore question the assumption of an increasing accuracy of single-blob models in the description of the system as f grows.

As a final analysis, we now discuss the aforementioned "polymer-to-colloid" crossover which is expected to occur in the system by increasing the functionality of the stars f. Roughly speaking, star polymers are believed to become more and more compact as f grows, behaving as hard spheres for $f \to \infty$. This result, however, is far from obvious, since we are considering the universal physical properties of polymers in the scaling limit, when $L \to \infty$. The residual flexibility of our multiblob model with respect to the single-blob ones allows us to investigate the density effects on the structural properties of a single star polymer, in order to test the stiffness of the system as the functionality f grows. We then determine the set of intramolecular distribution function $P_{\rm ca}(b)$, $P_{\rm aa}(b)$ and $P_{\rm th}(\cos\theta)$ for the arm-arm distance, the center-arm distance and the bond angle, as the density increases. Their definitions are presented in Eqs. (5.34), (5.35) and (5.36) respectively. We report in Fig. 5.13 the results for $f = 6$, obtained for volume fractions $\Phi_p = 0$, 1 and 2.

For what concerns the probability distribution functions of the center-arm and arm-arm distances $\bar{P}_{\rm ca}$ and $\bar{P}_{\rm aa}$, passing from $\Phi_p = 0$ to $\Phi_p = 2$ we see that these significantly decrease in range. Each star polymer, as expected, tends to shrink as a consequence of the repulsive interactions with the other molecules in the system. On the contrary, the bond angle distribution $\bar{P}_{\rm th}$ varies smoothly in the range of densities investigated.

The shrinkage of the molecules as the density increases can be quantified by means of the average blob model radius of gyration $\hat{R}_{g,b}(\Phi_p)$ defined in Eq. (5.39). Again, we recall that $\hat{R}_{g,b}(\Phi_p)$ is not the radius of gyration $\hat{R}_g(\Phi_p)$ of the micriscopic model, their difference being related to the average size of the blob $\hat{r}_{g,b}$. In Fig. 5.14, we report the Φ_p-behavior of the adimensional universal combination $\hat{R}_{g,b}(\Phi_p)/\hat{R}_{g,b}(0)$ of the multiblob model, for $f = 6$ and 12.

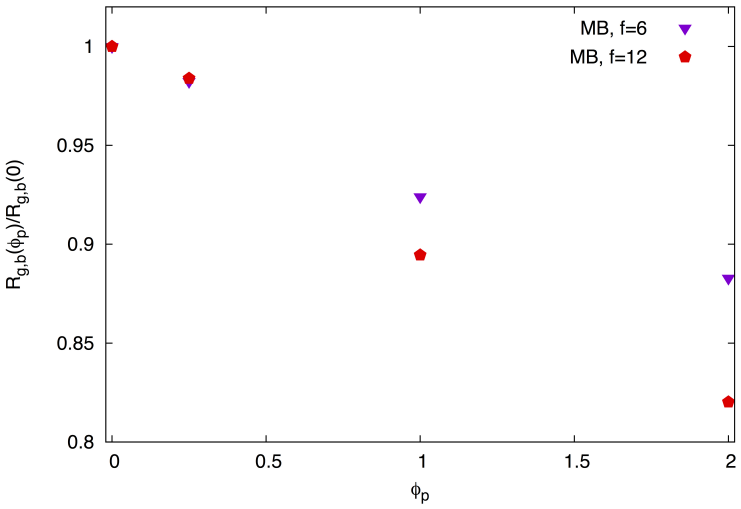

Figure 5.14. Adimensional combination $\hat{R}_{g,b}/\hat{R}_{g,b}(0)$ in the multiblob (MB) model as a function of Φ_p, for $f = 6$ and 12.

As we expected, molecules significantly as $\Phi_p = 0$ increases to $\Phi = 2$. For $f = 6$, and at $\Phi_p = 2$, the size of a star polymers is $\hat{R}_{g,b}(\Phi_p) \approx 0.9\hat{R}_{g,b}(0)$. More surprisingly, for $f = 12$ and at $\Phi_p = 2$, we have $\hat{R}_{g,b}(\Phi_p) \approx 0.8\hat{R}_{g,b}(0)$, hence the size of these molecules is reduced more.
This result seems to be in contrast with the general assumption that these molecules should become more rigid as the functionality f increases, moving towards the hard-spheres limit, and can be qualitatively explained as follows. For low functionalities f, the intermolecular repulsion among the star polymers can be minimized by means of an interpenetration of different molecules. In this mechanism, single-molecule conformational properties as the average size $\hat{R}_{g,b}$ are weakly perturbed. On the contrary, if we increase the functionality f, molecules interpenetrations become more difficult, and the only efficient way of reducing intermolecular repulsion is that of reducing the molecule size, so that each star polymers shrinks. This discussion may lead to a different conception of star polymers as compact objects, if compared to the hard-spheres interpretation: since the interpenetration of different molecules becomes more and more difficult, star polymers become compact molecules as f increases. On the other hand, they are not hard, since their intrinsically soft nature is such that at high densities they can still reduce their size in order to minimize the intermolecular repulsion with the other molecules.
These conclusion must obviously be validated by additional analyses. First of all, we must develop multiblob models for star polymers which are able to describe molecules with higher functionalities. Indeed, $f = 12$ is not large enough to accurately test the colloidal limit $f \gg 1$. This point is actually under investigation. Moreover, one should test the density dependence of the blob radius of gyration $\hat{r}_{g,b}$. Indeed, this quantity contributes to the total radius of gyration $\hat{R}_{g,b}$, and could modify the predictions we obtained so far. This second point is more difficult to determine, as we should perform full-monomer Monte Carlo simulations of star polymers in the

semidilute regime, which is a difficult computational task, since we are interested in the scaling-limit properties of the system.

Conclusions

In this thesis, we have critically analyzed and discussed the thermodynamic behavior of solutions of linear polymer chains and star polymers, and of colloid-linear chains mixtures, in a coarse-grained (CG) approach to interactions. In CG schemes, most of the monomeric degrees of freedom are integrated out and each polymer is represented by a set of n effective interaction sites. Single-blob (SB) models are obtained for $n = 1$, thus retaining only three translational degrees of freedom for each polymer [46, 47], and interactions among polymers are parametrized in terms of intermolecular potentials. For $n > 1$, we obtain multiblob models (MB), in which each molecule is mapped onto n atoms, which interact by means of inter- and intramolecular potentials [83, 84].

After a short summary of statistical mechanics [2–4] and of the basic concepts of polymer physics [24–28], developed in Chap. 1 and 2, in Chap. 3 we reviewed the general coarse-graining theory, and applied it to the case of polymer solutions. For single-blob models, the effective potential among the coarse-grained sites has an inherently many-body nature [32], and can be reduced to a sum of pairwise central contributions either in the low polymer-concentration limit or by allowing the pair potential to depend on the thermodynamic state of the system [70–74]. The last possibility should be used with care, as standard thermodynamic relations no longer hold, and the equivalence of ensembles breaks down [51, 52]. The effects of many-body intermolecular interactions among the coarse-grained molecules cannot be neglected as soon as multiple overlaps among different molecules occur, *i.e.*, in the semidilute regime $\Phi_p \gtrsim 1$. However, we can in principle reduce multiple overlaps by reducing the average volume occupied by each molecule, thus switching to a lower level of coarse-graining and introducing multiblob models [83, 84]. In these models, it is possible to tune the number of effective sites n so that intermolecular many-body contributions to interactions are negligible and the total intermolecular potential can be expressed in terms of zero-density potentials among two polymers. Multiblob models are defined in terms of intramolecular and intermolecular potentials: their exact derivation is unfeasible in practice, due to their many-body nature, hence approximations must be introduced. Our choice for the intramolecular potential was to parametrize it in terms of scalar variables, which account for the original n-body nature of the interaction. For what concerns the two-polymer intermolecular interaction, we further simplified it considering only pairwise-additive potentials among the blobs.

In Chap. 4, we have revised coarse-grained, single-blob models for polymer solutions and colloid-polymer mixtures. This strategy has been widely used in the past [48, 53, 69–71, 75, 91, 92, 95, 103] to study polymer solutions in the homogeneous

liquid phase, and the phase diagram of mixtures of nonadsorbing colloids and chains of different architectures in a solvent. We started the discussion from homogenous polymer solutions, in Sec. 4.2.1, where we have shown the limits of validity of the single-blob model with state-independent interactions (derived at zero polymer density) in reproducing the correct thermodynamic behavior of the original system, critically discussing the problems connected with the choice of the effective interaction site. We then discussed the apparent improvement obtained by switching to density-dependent pair interactions in Sec. 4.2.2 [70–74]. The latter model is indeed tuned to represent the pair correlation function at any finite polymer concentration, but it requires the knowledge of such correlation for the underlying microscopic model, a task which needs to be accomplished by simulating the microscopic model itself. This fact points to a limited predictive character and weakens the relevance of this strategy. Moreover, different routes to physical properties, which are equivalent for state-independent potentials, provide different results when the interaction itself depends on the thermodynamic state of the system [51, 52]. We have explicitly discussed the calculation of the chain chemical potential for the homogeneous solution. A main consequence of this inconsistency is the failure of the equivalence among different statistical ensembles, even in the thermodynamic limit [52].
Then, in Sec. 4.3, we discussed the phase diagram of colloid-polymer mixtures, as predicted by coarse-grained, single-blob models, for several average polymer-to-colloid size ratios q. For $q = 1$, surprisingly, the CG model with zero-density interactions does not present the fluid-fluid transition which is expected to occur in the system, as predicted by scaling-limit extrapolation of full-monomer simulations [100] and phenomenological theories, such as the generalized free-volume theory (GFVT) [63, 89, 104]. On the contrary, the density-dependent CG model exhibits the demixing transition [93], which is found to be in qualitative agreement with GFVT results. As discussed in Sec. 4.3.1.1, we can now see that this agreement is accidental, since the phase transition in this model is driven by density fluctuations larger than in the underlying microscopic system. The coarse-grained model with zero-density interactions, which is thermodynamically consistent, is more accurate than the other model, but its accuracy is limited to a small range of polymer densities in the homogenous phase. For $q = 0.5$ and 0.8 the single-blob model with zero-density potentials exhibits the demixing transition, but overestimates significantly GFVT results, which are expected to become more and more accurate as q decreases. Therefore, an accurate single-site, coarse-grained model which is able to predict accurately the demixing transition of colloid-polymer dispersions seems to be out of reach.
In Sec. 4.3.2, we determined the phase diagram of colloid-polymer mixtures by means of integral equation methods, and the approximate closure relations presented in Chap. 1, again for $q = 0.5$, 0.8 and 1. For single-blob models, integral equation methods have been proved to be very accurate. In particular, because of the soft nature of the interactions, the hypernetted-chain and Rogers-Young closures work quite well [4, 70, 71, 137]. It is then natural to investigate whether integral equations can be successfully applied to the study of the phase diagram and thermodynamics of colloid-polymer mixtures. In the density region in which the system demixes, integral equations may not converge, or may converge to physically unacceptable solutions [117–119]. We characterized these convergence termination lines, if present,

and compared them to the Monte Carlo, single-blob binodal lines of Sec. 4.3.1, to determine whether they are related to an instability of the homogeneous phase.
For $q = 1$, no sign of termination line was found for all the approximate closures used. This is not surprising, as no sign of phase separation for the system was observed by means of Monte Carlo simulations. For $q = 0.5$ and $q = 0.8$, termination lines are present, but significantly underestimate the Monte Carlo binodals, especially in the colloid-liquid phase. In conclusion, our results show that none of the closures we considered provides accurate results for the demixing transition, although the Rogers-Young closure performs better than the hypernetted-chain one, which stops converging at very small polymer volume fraction in the colloid-liquid phase.
We then compared the integral-equation and Monte Carlo predictions for the zero-momentum structure factors and the pair correlation functions of the system, below the termination line. Again, the Rogers-Young closure is the one that fares best.
We then performed an analysis of the bridge functions at zero polymer densities, comparing the bridge functions used in the various integral-equation approximate closures with the exact estimates obtained numerically, and proposed a new approach, which uses Monte Carlo bridge functions in the integral equation methods. These results further confirmed the inability of the integral equation methods to predict the correct thermodynamic behavior of the system, especially in the colloid-liquid phase.
In Chap. 5 we discussed the thermodynamic behavior of star polymer solutions. Little is known about their thermodynamic and structural behavior, which has mostly been discussed in terms of phenomenological models [75, 129, 130, 137]. We analyzed the system by means of accurate coarse-grained, single-blob models in the center of mass and central monomer [76] representation, and presented a new multiblob model, which should be able to reproduce the thermodynamic behavior of the original system up to the semidilute regime. We parametrized and obtained the intermolecular and intramolecular interactions of the multiblob model, so that the zero-density structural and thermodynamic properties [135] of the microscopic system, obtained by means of full-monomer simulations of the lattice Domb-Joyce model, are reproduced. We compared the thermodynamics of the MB model with those of the SB models in both representations. We found that single-blob models significantly underestimate the osmotic coefficient $Z = \beta P/\rho_p$ in the semidilute regime. Moreover, the deviations do not change if the functionality of the stars increases, at least from $f = 6$ to $f = 12$, a results which may question the general assumption that single-blob models become more and more accurate as f increases. We further confirmed the problems connected to the choice of the effective interaction site of single-blob models. Indeed, the zero-density SB model in the central monomer representation was found to be a worse approximation if compared to the center of mass representation. To confirm these results, we are currently developing multiblob models with increasing functionalities, up to $f = 40$.
The residual flexibility of the multiblob model allowed us to determine the effect of density on single-molecule structural properties, in order to investigate the polymer-to-colloid crossover which is expected to hold in the system as the functionality f increases. By computing the density dependence of the MB model radius of gyration (which must not be confused with the radius of gyration of the microscopic model), we saw that each star polymers shrinks as the density increases, as a

consequence of the intermolecular repulsion with the other molecules in the system. More surprisingly, the compression of the polymers with $f = 12$ arms is larger than that of the polymers with $f = 6$ arms. This result is in apparent contradiction with the general assumption that star polymer should become more stiff and compact objects as f increases, behaving as hard spheres for $f \to \infty$ [75]. Again, this result must be confirmed by multiblob models with a higher number of arms, which are actually in preparation.

In conclusion, we can summarize the main results of this thesis with this take-home message: coarse-graining methods are a very powerful (and sometimes necessary) tool in the analysis of the universal, large-scale and thermodynamic properties of polymer solutions and colloid-polymer mixtures. In the development of *accurate* coarse-grained models for polymers, however, one should pay attention to two main criticalities, as we pointed out along the discussion.

The first one is not a consequence of the coarse-graining procedure, but is related to the general theory of polymers. Indeed, the universal properties of polymer solutions are obtained only in the large degree of polymerization limit $L \to \infty$. In computer simulations of polymers, with L large but finite, corrections to scaling must be taken into account, otherwise quantitative deviations from the universal, scaling-limit results may appear.

The second one is instead related to the coarse-graining procedure in itself.

Since an *exact* CG mapping is unfeasible in practice, approximations are needed, which always generates a lack of consistency between the CG and the original model. The consequences of introducing these approximations must always be considered, and the predictions of approximate CG models critically analyzed. As we have shown, zero-density, single-blob models with pairwise-additive interactions should be applied only in the description of the dilute regime of polymer solutions (at least for the polymer architectures we considered), keeping in mind that their predictions for the thermodynamic behavior of the system may depend on the effective interaction site chosen. In addiction, they poorly reproduce the phase diagram of colloid-linear chain mixtures. The improvement obtained by switching to pair interactions which explicitly depend on the thermodynamic state of the system is only apparent, as these may further worsen the analysis by introducing thermodynamic inconsistencies. In this framework, multiblob models represent the most natural choice for increasing the density range in which CG models based on zero-density potentials can be used. Indeed, their residual flexibility with respect to the single-blob case is a fundamental feature for the investigation of the semidilute regime of polymer solutions, where different polymer coils strongly overlap. Moreover, MB models allow us to investigate properties which are absent by definition in zero-density SB models, such as the effects of density on the molecular conformations. This was shown to be very interesting, for example, in the case of star polymer solutions.

Multiblob models, on the other hand, have the disadvantage of introducing complex intramolecular and intermolecular interactions among the effective sites, which necessitate further approximations. These approximations must be *a posteriori* verified by means of a direct comparison with full-monomer results. Indeed, it is important to stress that the primary requirement in the development of a coarse-grained model, in general, must always be the consistency with the mesoscopic behavior of the original, microscopic model.

Acronyms

AOV Asakura-Oosawa-Vrij.

CG Coarse-grained.

CM Center of mass.

DJ Domb-Joyce.

FM Full-monomer.

GFVT Generalized free-volume theory.

HNC Hypernetted-chain.

MB Multiblob.

MP Mid-point/central monomer.

OZ Ornstein-Zernike.

PY Percus-Yevick.

RHNC Reference hypernetted-chain.

RPA Random-phase approximation.

RY Rogers-Young.

SAW Self-avoiding walk.

SB Single-blob.

Bibliography

[1] K. Huang, *Statistical mechanics*, 2nd ed. (Wiley, New York, 1987).

[2] M. Tuckerman, *Statistical Mechanics: Theory and Molecular Simulation* (Oxford University Press, Oxford, 2010).

[3] P. Attard, *Thermodynamics and Statistical Mechanics: Equilibrium by Entropy Maximization* (Academic Press, London, 2002).

[4] J. P. Hansen and I. McDonald, *Theory of Simple Liquids*, 3rd ed. (Academic Press, Amsterdam, 2006).

[5] A. Ben-Naim, *Molecular theory of solutions* (Oxford University Press, Oxford, 2006).

[6] J. G. Kirkwood and F. P. Buff, J. Chem. Phys. **19**, 774 (1951).

[7] T. Morita, Prog. Theor. Phys. **23**, 829 (1960).

[8] P. Attard, J. Chem. Phys. **94**, 2370 (1991).

[9] J. P. Hansen, G. M. Torrie, and P. Vieillefosse, Phys. Rev. A **16**, 2153 (1977).

[10] M. S. Wertheim, Phys. Rev. Lett. **10**, 321 (1963).

[11] J. L. Lebowitz, Phys. Rev. A **133**, 895 (1964).

[12] F. J. Rogers and D. A. Young, Phys. Rev. A **30**, 999 (1984).

[13] T. Biben and J. P. Hansen, J. Phys.: Condens. Matter **3**, F65 (1991).

[14] Y. Rosenfeld and N. W. Ashcroft, Phys. Rev. A **20**, 1208 (1979).

[15] E. Enciso, F. Lado, M. Lombardero, J. L. F. Abascal, and S. Lago, J. Chem. Phys. **87**, 2249 (1984).

[16] F. Lado, Phys. Lett. A **89**, 196 (1982).

[17] L. Verlet and J.J. Weis, Phys. Rev. A **5**, 939 (1972).

[18] D. Henderson and E. W. Grundke, J. Chem. Phys. **63**, 601 (1975).

[19] J. L. Lebowitz, G. Helfand, and E. Praestgaard, J. Chem. Phys. **43**, 774 (1965).

[20] G. A. Mansoori, N. F. Carnahan, K. E. Starling, and T. W. Leland, Jr., J. Chem. Phys. **54**, 1523 (1971).

[21] E. W. Grundke and D. Henderson, Mol. Phys. **24**, 269 (1972).

[22] L. L. Lee and D. Levesque, Mol. Phys. **26**, 1351 (1973).

[23] P. Flory, *Principles of Polymer Chemistry* (Cornell University Press, New York, 1953).

[24] P. G. de Gennes, *Scaling Concepts in Polymer Physics* (Cornell University Press, London, 1979).

[25] M. Doi and S. F. Edwards, *The Theory of Polymer Dynamics* (Clarendon Press, Oxford, 1988).

[26] A. Y. Grosberg and A. R. Khokhlov, *Statistical Physics of Macromolecules* (American Institute of Physics, New York, 1994).

[27] H. Fujita, *Polymer Solutions* (Elsevier, Amsterdam, 1990).

[28] M. Rubinstein and R. H. Colby, *Polymer Physics* (Oxford University Press, 2003).

[29] K. F. Freed, *Renormalization Group Theory of Macromolecules* (Wiley-Interscience, New York, 1987).

[30] J. des Cloizeaux and G. Jannink, *Polymers in Solution: Their Modelling and Structure* (Clarendon, Oxford, 1990).

[31] L. Schäfer, *Excluded Volume Effects in Polymer Solutions* (Elsevier, Amsterdam, 1990). (Springer Verlag, Berlin, 1999).

[32] M. Dijkstra, R. van Roij, and R. Evans, Phys. Rev. E **59**, 5744 (1999).

[33] C. I. Addison, A. A. Louis, and J. P. Hansen, J. Chem. Phys **121**, 612 (2004).

[34] A. D. Sokal, *Monte Carlo Methods for the Self-Avoiding Walk*, arXiv:hep-lat/9405016 (1994).

[35] C. Domb and G. S. Joyce, J. Phys. C **5**, 956 (1972).

[36] S. Caracciolo, B. M. Mognetti, and A. Pelissetto, *Macromol. Theory Simul.* **17**, 67 (2008).

[37] ,D.J. Ashton and N.B. Wilding, J. Chem. Phys **140**, 244118 (2014).

[38] L.P. Kadanoff, Physics **2**, 263 (1966).

[39] K. Wilson, Rev. Mod. Phys. **47**, 773 (1975).

[40] S. K. Ma, *Modern theory of critical phenomena* (Westview Press, New York, 1976).

[41] J. Zinn-Justin, *Phase transition and the renormalization group* (Oxvord University Press, Oxford, 2007).

[42] G.A. Voth, ed., *Coarse-Graining of Condensed Phases and Biomolecular Systems* (CRC Press, Boca Raton, 2009).

[43] R. Feller, Guest Editor, Phys. Chem. Chem. Phys. **11**, 1853 (2009).

[44] M. Wilson, Guest Editor, Soft Matter **5**, 4341 (2009).

[45] Multiscale Modelling of Soft Matter, Faraday Discussions 144, 1 (2010).

[46] C.N. Likos, Phys. Rep. **348**, 267 (2001).

[47] C.N. Likos, Soft Matter **2**, 478 (2006).

[48] G. D'Adamo, A. Pelissetto, and C. Pierleoni, J. Chem. Phys. **136**, 224905 (2012).

[49] F. Müller-Plathe, Chem. Phys. Chem. **3**, 754 (2002).

[50] R.L. Henderson, Phys. Lett. A. **49**, 197 (1974).

[51] A. A. Louis, J. Phys.: Condens. Matter **14**, 9187 (2002).

[52] G. D'Adamo, A. Pelissetto, and C. Pierleoni, J. Chem. Phys. **138**, 234107 (2013).

[53] A. Fortini, P.G. Bolhuis, and M. Dijkstra, J. Chem. Phys. **128**, 024904 (2008).

[54] S. Asakura and F. Oosawa, J. Chem. Phys. **22**, 1255 (1954).

[55] A. Vrij, Pure Appl. Chem. **48**, 471 (1976).

[56] H.N.W. Lekkerkerker, W.C.K. Poon, P.N.Pusey, A. Stroobants, and P. Warren, Europhys. Lett. **20**, 559 (1992).

[57] M. Dijkstra, J.M. Brader, and R. Evans, J. Phys.: Condens. Matter **11**, 10079 (1999).

[58] M. Schmidt, A. R. Denton, and J. M. Brader, J. Chem. Phys. **118**, 1541 (2003).

[59] R. L. C. Vink and M. Schmidt, Phys. Rev. E **71**, 051406 (2005).

[60] J. Zausch, P. Virnau, K. Binder, J. Horbach, and R. L. C. Vink, J. Chem. Phys. **130**, 064906 (2009).

[61] J. Zausch, J. Horbach, P. Virnau, and K. Binder, J. Phys.: Condens. Matter **22**, 104120 (2010).

[62] M. A. Annunziata and A. Pelissetto, Phys. Rev. E **86**, 041804 (2012).

[63] H. N. W. Lekkerkerker and R. Tuinier, *Colloids and the Depletion Interaction, Lectures Notes in Physics Vol. 833* (Springer, Berlin, 2011).

[64] A. A. Louis, P. G. Bolhuis, E. J. Meijer, and J. P. Hansen, J. Chem. Phys. **117**, 1893 (2002).

[65] P.J. Flory and W.R. Krigbaum, J. Chem. Phys. **18**, 1086 (1950).

[66] A. Grosberg, P. Khalatur, and A. Khokhlov, Makromol. Chem. Rapid Commun. **3**, 709 (1982).

[67] A.B. Krüger and L. Schäfer, J. Physique **50**, 3191 (1989).

[68] J. Dautenhahn and C. Hall, Macromolecules **27**, 5399 (1994).

[69] A. Pelissetto and J.-P. Hansen, J. Chem. Phys. **122**, 134904 (2005).

[70] A.A. Louis, P.G. Bolhuis, J.P. Hansen, and E.J. Meijer, Phys. Rev. Lett. **85**, 2522 (2000).

[71] P.G. Bolhuis, A.A. Louis, J.P. Hansen, and E.J. Meijer, J. Chem. Phys. 114, 4296 (2001).

[72] P.G. Bolhuis and A.A. Louis, Macromolecules **35**, 1860 (2002).

[73] P.G. Bolhuis, A.A. Louis, and J.P. Hansen, Phys. Rev. E **64**, 021801 (2001).

[74] A. A. Louis, P. G. Bolhuis, E. J. Meijer, and J. P. Hansen, J. Chem. Phys. **116**, 10547 (2002).

[75] C. N. Likos, H. Löwen, M. Watzlawek, B. Abbas, O. Jucknischke, J. Allgaier, and D. Richter, Phys. Rev. Lett. **80**, 4450 (1998).

[76] H.-P. Hsu and P. Grassberger, Europhys. Lett. **66**, 874 (2004).

[77] R. Menichetti and A. Pelissetto, J. Chem. Phys. **138**, 124902 (2013).

[78] S. Caracciolo, B.M. Mognetti, and A. Pelissetto, J. Chem. Phys. **125**, 094903 (2006).

[79] T.A. Witten and P.A. Pincus, Macromolecules **19**, 2509 (1986).

[80] C. von Ferber, A. Jusufi, M. Watzlawek, and C.N. Likos, H. Löwen, Phys. Rev. E **62**, 6949 (2000).

[81] A. Pelissetto, Phys. Rev. E **85**, 021803 (2012).

[82] B. Widom, J. Chem. Phys. **39**, 2802 (1963).

[83] C. Pierleoni, B. Capone, and J. P. Hansen, J. Chem. Phys. **127**, 171102 (2007).

[84] G. D' Adamo, A. Pelissetto, and C. Pierleoni, Soft Matter **8**, 5151 (2012).

[85] W.C.K. Poon, J. Phys.: Condens. Matter **14**, R859 (2002).

[86] M. Fuchs and K.S. Schweizer, J. Phys.: Condens. Matter **14**, R239 (2002).

[87] R. Tuinier, J. Rieger, and C.G. de Kruif, Adv. Colloid Interface Sci. **103**, 1 (2003).

[88] K.J. Mutch, J.S. van Duijneveldt, and J. Eastoe, Soft Matter **3**, 155 (2007).

[89] G.J. Fleer and R. Tuinier, Adv. Coll. Interface Sci. **143**, 1 (2008).

[90] O. Myakonkaya and J. Eastoe, Adv. Coll. Interface Sci. **149**, 39 (2009).

[91] A. Jusufi, J. Dzubiella, C.N. Likos, C. von Ferber, and H. Löwen, J. Phys.: Condens. Matter **13**, 6177 (2001).

[92] A. Pelissetto and J.P. Hansen, Macromolecules **39**, 9571 (2006).

[93] P.G. Bolhuis, A.A. Louis, and J. P. Hansen, Phys. Rev. Lett. **89**, 128302 (2002).

[94] R.L.C. Vink, A. Jusufi, J. Dzubiella, and C.N. Likos, Phys.Rev. E **72**, 30401 (2005).

[95] J. Dzubiella, A. Jusufi, C.N. Likos, C. von Ferber, H.Löwen, J. Stellbrink, J. Allgaier, D. Richter, A.B. Schofield, P.A. Smith, W.C.K. Poon, and P.N. Pusey, Phys. Rev. E **64**, 010401(R) (2001).

[96] G. D'Adamo, R. Menichetti, A. Pelissetto, and C. Pierleoni, Eur. Phys. J. Special Topics **224**, 2239 (2015).

[97] R. Menichetti, G. D'Adamo, A. Pelissetto, and C. Pierleoni, Mol. Phys. **113**, 2629 (2015).

[98] P.G. Bolhuis, E.J. Meijer, and A.A. Louis, Phys. Rev. Lett. **90**, 068304 (2003).

[99] C.-Y. Chou, T.T.M. Vo, A.Z. Panagiotopoulos, and M. Robert, Physica A **369**, 275 (2006).

[100] N.A. Mahynski, T. Lafitte, and A.Z. Panagiotopoulos, Phys. Rev. E **85**, 051402 (2012).

[101] N.A. Mahynski, B. Irick, and A.Z. Panagiotopoulos, Phys. Rev. E **87**, 022309 (2013).

[102] A. Pelissetto, J. Chem. Phys. **129**, 044901 (2008).

[103] G. D' Adamo, A. Pelissetto, and C. Pierleoni, Mol. Phys. **111**, 3372 (2013).

[104] G. D'Adamo, A. Pelissetto, and C. Pierleoni, J. Chem. Phys. **141**, 024902 (2014).

[105] G. D'Adamo, A. Pelissetto, and C. Pierleoni, J. Chem. Phys. **141**, 244905 (2014).

[106] G.M. Torrie and J.P. Valleau, J. Comp. Phys. **23**, 197 (1977).

[107] A. Pelissetto and F. Ricci-Tersenghi, *Large Deviations in Physics: The Legacy of the Law of Large Numbers*, edited by A. Vulpiani, F. Cecconi, M. Cencini, A. Puglisi, and D. Vergni, Lecture Notes Phys. **885**, 161 (2014).

[108] R.L.C. Vink and J. Horbach, J. Chem. Phys. 121, 3253 (2004).

[109] R.L.C. Vink, *Computer Simulation Studies in Condensed Matter Physics XVIII*, edited by D.P. Landau, S.P. Lewis, H.B. Schuettler (Springer, Berlin, 2004).

[110] A.M. Ferrenberg and R.H. Swendsen, Phys. Rev. Lett. **63**, 1195 (1989).

[111] N.B. Wilding, J. Phys.: Condens. Matter **9**, 585 (1997).

[112] M.M. Tsypin and H.W.J. Blöte, Phys. Rev. E **62**, 73 (2000).

[113] M. Mézard and G. Parisi, J. Phys. A **29**, 6515 (1996).

[114] M. Mézard and G. Parisi, J. Chem. Phys. **111**, 1076 (1999).

[115] G. Parisi and F. Zamponi, Rev. Mod. Phys. **82**, 789 (2010).

[116] J.-M. Bomont, J.-P. Hansen, and G. Pastore, J. Chem. Phys. **141**, 174505 (2014).

[117] P. T. Cummings and G. Stell, J. Chem. Phys. **78**, 1917 (1983).

[118] L. Belloni, J. Chem. Phys. **98**, 8080 (1993).

[119] R. F. Rull, C. Vega, and S. Lago, Mol. Phys. **87**, 1235 (1996).

[120] G. Sarkisov and E. Lomba, J. Chem. Phys. **122**, 214504 (2005).

[121] J. Dzubiella, C. N. Likos, and H. Löwen, J. Chem. Phys. **116**, 9518 (2002).

[122] G. Pellicane and O. G. Pandaram, J. Chem. Phys. **141**, 044508 (2014).

[123] G. A. Vliegenthart and H. N. W. Lekkerkerker, J. Chem. Phys. **112**, 5364 (2000).

[124] M. G. Noro and D. Frenkel, J. Chem. Phys. **113**, 2941 (2000).

[125] K. Ohno and K. Binder., J. Phys. France **49**, 1329 (1988).

[126] L. Schäfer, C. von Ferber, and U. Lehr, Nucl. Phys. B **374**, 473 (1992).

[127] J. F. Douglas, J. Roovers, and K. F. Freed, Macromolecules **23**, 4168 (1990).

[128] G. Merkle, W. Burchard, P. Lutz, K. F. Freed, and J. Gao, Macromolecules **26**, 2736 (1993).

[129] M. Daoud and J. P. Cotton, J. Phys. France **43**, 531 (1982).

[130] T. M. Birshtein and E. B. Zhulina, Polymer **25**, 1453 (1984).

[131] G. S. Grest, Macromolecules **27**, 3493 (1994).

[132] H.-P. Hsu, W. Nadler, and P. Grassberger, Macromolecules **37**, 4658 (2004).

[133] C. Mayer and C. N. Likos, Macromolecules **40**, 1196 (2007).

[134] S. Huissmann, R. Blaak, and C. N. Likos, Macromolecules **42**, 2806 (2009).

[135] F. Randisi and A. Pelissetto, J. Chem. Phys **139**, 154902 (2013).

[136] C. von Ferber, A. Jusufi, C. N. Likos, H. Löwen, and M. Watzlawek, Eur. Phys. J. E **2**, 311 (2000).

[137] M Watzlawek, H Löwen, and C N Likos, J. Phys.: Condens. Matter **10**, 8189 (1998).

[138] M. Camargo and C. N. Likos, J. Chem. Phys. **130**, 204904 (2009).

[139] Nathan A. Mahynski and Athanassios Z. Panagiotopoulos, J. Chem. Phys. **139**, 024907 (2013).

[140] G. Ciccotti and J. P. Ryckaert, Comp. Phys. Rep. **4**, 345 (1986).

[141] R. L. C. Akkermans and G. Ciccotti, J. Phys. Chem. B **108**, 6866 (2004).